

# Functional and structural diversity of external tufted and deep short-axon cells in the main olfactory bulb

Doctoral Dissertation

**Miklós Antal M.D.**

Semmelweis University  
John Szentágothai Neuroscience School of Ph.D. Studies



Supervisor: Zoltán Nusser D.Phil., D.Sc.

Scientific Referees of the Ph.D. Dissertation: Zoltán Benyó M.D., Ph.D., D.Sc.  
Katalin Halasy Ph.D., D.Sc.

Chair of the Comprehensive Exam: András Csillag M.D., Ph.D., D.Sc

Committee Members of the Comprehensive Exam:

Gábor Tamás Ph.D., D.Sc.

Tibor Zelles Ph.D.

Budapest  
2008

## I. TABLE OF CONTENTS

<b>I. TABLE OF CONTENTS</b> .....	2
<b>II. LIST OF ABBREVIATIONS</b> .....	5
<b>III. INTRODUCTION</b> .....	9
III.1. Neuronal components of the main olfactory bulb.....	9
III.1.1. Afferents.....	10
III.1.1.1. Sensory afferents and the olfactory glomerulus.....	10
III.1.1.2. Centrifugal inputs, neuromodulators.....	12
III.1.2. Principal neurons.....	13
III.1.3. Local interneurons.....	14
III.2. Synaptic connectivity in the main olfactory bulb.....	16
III.2.1. Synapses in the glomerular layer.....	16
III.2.2. Synapses in the external plexiform layer.....	18
III.2.3. Synapses in the granule cell layer.....	18
III.3. Functional and structural diversity of interneurons.....	19
<b>IV. AIMS</b> .....	21
<b>V. METHODS</b> .....	22
V.1. Acute slice preparation and electrophysiological recordings.....	22
V.2. Visualization of the recorded cells.....	25
V.3. <i>In vivo</i> injection of fluorescent microspheres.....	26
V.4. Immunofluorescent microscopy.....	26
V.5. Three-dimensional reconstructions of deep short axon cells.....	27
V.6. Electron microscopy and postembedding immunolabeling.....	28
V.7. Statistical procedures.....	28
<b>VI. RESULTS AND CONCLUSIONS</b> .....	31
<b>VI.1. Correlation of functional and structural characteristics predicts two         subpopulations of external tufted cells</b> .....	31
VI.1.1. Active and passive electrical properties of external tufted cells.....	31
VI.1.2. The presence of two subpopulations of external tufted cells based on their physiological properties.....	34

VI.1.3. Quantitative characterization of external tufted cells based on their dendritic arborizations.....	38
VI.1.4. Comparing physiologically and morphologically determined external tufted cell subpopulations.....	43
VI.1.5. Summary of the results and conclusions.....	45
<b>VI.2. Novel intra- and extrabulbar GABAergic connections in the main olfactory bulb are provided by distinct subtypes of deep short-axon cells.....</b>	<b>46</b>
VI.2.1. The morphological diversity of deep short-axon cells.....	46
VI.2.2. Granule cell layer-dSACs project to higher olfactory areas.....	49
VI.2.3. Molecular differences between deep short-axon cells.....	51
VI.2.4. Deep short-axon cells show distinct intrinsic electrical properties.....	53
VI.2.5. Excitatory and inhibitory inputs onto deep short-axon cells.....	54
VI.2.6. The postsynaptic targets of GABAergic deep short-axon cells are other GABAergic interneurons.....	57
VI.2.7. Functional characterization of the synaptic outputs of deep short-axon cells.....	61
VI.2.8. Summary of the results and conclusions.....	66
<b>VII. DISCUSSION.....</b>	<b>67</b>
VII.1. Correlation of functional and structural characteristics predicts two subpopulations of external tufted cells.....	67
VII.1.1. Our results are in agreement with classical morphological studies.....	67
VII.1.2. The molecular heterogeneity of external tufted cells.....	68
VII.1.3. Basal dendrites – morphological predictors of bursting behavior in external tufted cells?.....	69
VII.1.4. What could be the major functional differences between the two types of external tufted cells?.....	70
VII.1.5. Subthreshold resonance properties show correlation with structural attributes.....	71
VII.2. Novel intra- and extrabulbar GABAergic connections in the main olfactory bulb are provided by distinct subtypes of deep short-axon cells.....	71
VII.2.1. Heterogeneity and classification of dSACs.....	72

VII.2.2. Granule cell layer-dSACs mediate a novel extrabulbar GABAergic projection.....	73
VII.2.3. Deep short-axon cells are interneuron-selective interneurons.....	74
VII.2.4. Novel intrabulbar connections between deep and superficial layers of the main olfactory bulb.....	75
VII.2.5. Properties of granule cell inhibition by deep short-axon cells.....	75
VII.2.6. Significance of deep short-axon cells in olfactory information processing.....	76
<b>VIII. SUMMARY – ÖSSZEFOGLALÁS.....</b>	<b>77</b>
<b>IX. BIBLIOGRAPHY.....</b>	<b>81</b>
IX.1. General bibliography.....	81
IX.2. Publications.....	90
<b>X. ACKNOWLEDGEMENTS.....</b>	<b>91</b>

## II. LIST OF ABBREVIATIONS

ABC	avidin–biotin–horseradish peroxidase complex
ACh	acetylcholine
ACSF	artificial cerebro-spinal fluid
AHP	after-hyperpolarization
AMPA	$\gamma$ -amino-3-hydroxy-5-methylisoxazole-4-propionic acid
AON	anterior olfactory nucleus
AP	action potential
BSA	bovine serum albumin
$[Ca^{2+}]_e$	extracellular concentration of $Ca^{2+}$
$[Cl^-]$	concentration of $Cl^-$
CB	calbindin
CNQX	6-cyano-7-nitroquinoxaline-2,3-dione disodium
CV	coefficient of variation
CWFSG	cold water fish skin gelatin
DAB	3'3-diaminobenzidine
D-AP5	D-(-)-2-amino-5-phosphonopentanoic acid
Dlink	linkage distance
Dmax	maximum linkage distance
dSAC	deep short-axon cell
$E_{Cl}$	equilibrium (reversal) potential for $Cl^-$
eIPSC	evoked IPSC
EM	electron microscope/microscopic
EPL	external plexiform layer
EPSC	excitatory postsynaptic current
ETC	external tufted cell
FFT	fast Fourier transformation
FWHM	full width at half maximum
GABA	$\gamma$ -amino-butiric acid
GABA <sub>A</sub> R	GABA <sub>A</sub> receptor
GL	glomerular layer

GC	granule cell
GCd	granule cell dendrite
GCg	granule cell gemmule
GCs	granule cell spine
GCL	granule cell layer
GI	intermediate granule cell
GII, G <sub>D</sub>	deep granule cell
GIII, G <sub>S</sub>	superficial granule cell
HCN 1	hyperpolarization activated and cyclic nucleotide-gated mixed cation channel 1
IN	interneuron
IPL	internal plexiform layer
IPSC	inhibitory postsynaptic current
ISI	inter-spike interval
ITC	internal tufted cell
JGC	juxtglomerular cell
LOT	lateral olfactory tract
[Mg <sup>2+</sup> ] <sub>e</sub>	extracellular concentration of magnesium
MC	mitral cell
MCd	mitral cell dendrite
MCL	mitral cell layer
mEPSC	miniature EPSC
mIPSC	miniature IPSC
MOB	main olfactory bulb
mRAS	mély rövid-axonú sejt
MTC	middle tufted cell
M/Td	mitral/tufted cell dendrite
NADPH	nicotinamide adenine dinucleotide phosphate
NBQX	2,3-dioxo-6-nitro-1,2,3,4-tetrahydrobenzo[f]quinoxaline-7-sulfonamide
NGS	normal goat serum
NMDA	N-methyl-D-aspartic acid

NOS	nitric oxide synthase
NPY	neuropeptide Y
ON	olfactory nerve
ONL	olfactory nerve layer
ORN	olfactory receptor neuron
P	postnatal day
PB	phosphate buffer
PCA	principal component analysis
PGC	periglomerular cell
PGCd	periglomerular cell dendrite
PGd	periglomerular cell dendrite
$P_r$	probability of neurotransmitter release
$R_a$	access resistance
$R_{in}$	input resistance
R-CPP	3-((R)-2-carboxypiperazin-4-yl)-propyl-1-phosphonic acid
RT	rise time
Rec	recording electrode
SAC	short-axon cell
SE-LM kit	silver enhancement light microscopy kit
sEPSC	spontaneous EPSC
sIPSC	spontaneous IPSC
SR95531	6-imino-3-(4-methoxyphenyl)-1(6 <i>H</i> )-pyridazinebutanoic acid
Stim	stimulating electrode
$\tau$	tau, membrane time constant
$\tau_w$	weighted decay time constant
$\sigma^2$	variance
TB	tris-buffer
TBLS	0.081% NaCl tris-buffer
TBS	tris-buffered saline
TBST	tris-buffered saline with Triton X-100
TC	tufted cell
TH	tyrosine hydroxylase

TSA	tyramide signal amplification
TTX	tetradotoxin
uIPSC	unitary IPSC (evoked by one presynaptic cell)
VIP	vasoactive intestinal polypeptide

### III. INTRODUCTION

The olfactory bulb is a bilateral structure of the vertebrate forebrain involved in olfaction, the perception of odors. It processes and transmits smell information from the nose to the brain and is divided into two distinct structures, the main olfactory bulb (MOB), and the accessory olfactory bulb. The latter forms an independent parallel pathway from the MOB, believed to play an important role in detection of pheromones, which are essential for mate selection, reproductive behavior and hormonally regulated odor-stimulated behaviors in many mammals (e.g. aggression) (Keverne, 1995).

#### III.1. Neuronal components of the main olfactory bulb

The main olfactory bulb, in most vertebrates, is the most rostral part of the brain. Similar to other sensory systems in the brain, the neuronal building blocks of the MOB can be categorized into three groups: input, output and intrinsic elements.

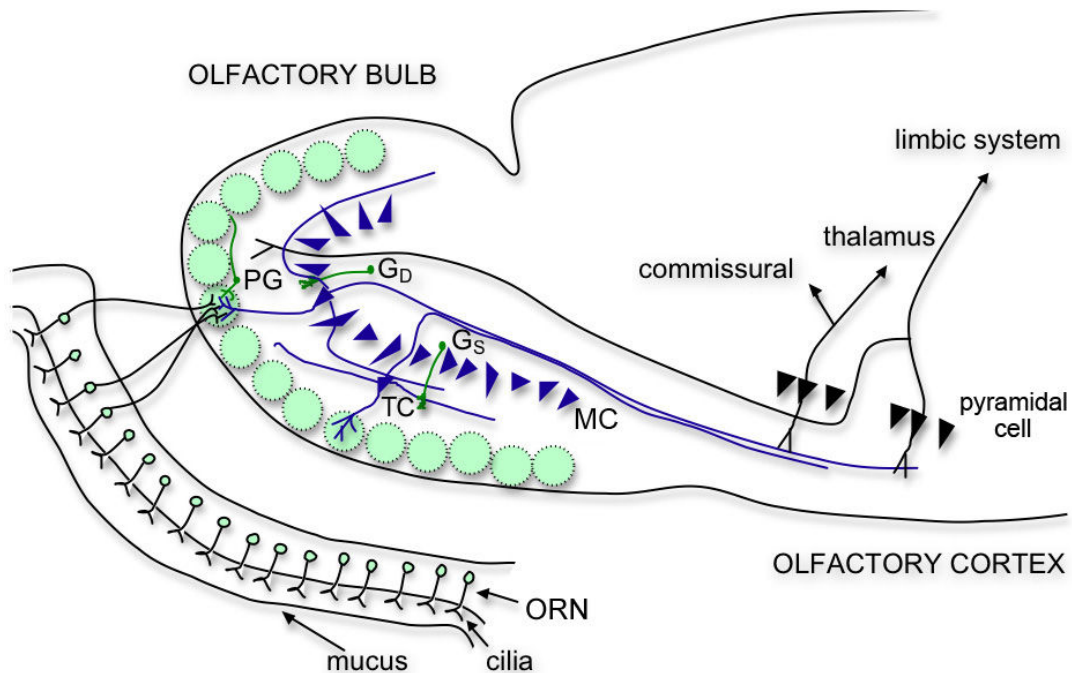


**Figure 1. A summary of the olfactory pathway.** The olfactory bulb receives direct sensory input from olfactory receptor neurons (ORNs) of the nasal epithelium and sends its output directly to the olfactory cortex. Some general aspects of projections patterns and connections with central brain regions are indicated. Abbreviations: PG: periglomerular cell, MC: mitral cell, TC: tufted cell, G<sub>S</sub>: superficial granule cell, G<sub>D</sub>: deep granule cell.

It receives a single source of direct sensory input, axons from olfactory receptor neurons (ORN) of the olfactory epithelium and sends its output directly to the olfactory cortices (Figure 1). However, it also receives "top-down" information from higher brain areas. The main olfactory bulb presents a multi-layered cellular architecture. In order from the surface towards the center of the bulb the layers are (Figure 2):

1. Olfactory nerve layer
2. Glomerular layer
3. External plexiform layer
4. Mitral cell layer
5. Internal plexiform layer
6. Granule cell layer
7. Lateral olfactory tract

### **III.1.1. Afferents**

#### **III.1.1.1. Sensory afferents and the olfactory glomerulus**

The sensory input is made up of a sophisticated arrangement of axons originating from the ORNs in the nasal olfactory epithelium. Despite the fact that within the epithelium ORNs possess a homogeneous appearance, they are highly diverse regarding their molecular characteristics. In rodents, a large multigene family encodes more than 1000 different olfactory receptors (Buck and Axel, 1991). Subpopulations of ORNs expressing the same odorant receptor are located in one of several regions across the epithelium, although the precise nature of their distribution is still under investigation.

These tightly packed bundles of ORN axons form the most superficial layer of the MOB, the olfactory nerve layer. As they target regions of the MOB, they defasciculate and reorganize. Axons that originate from ORNs expressing the same olfactory receptor gene usually terminate in two synaptic complexes, also known as, glomeruli within the glomerular layer, one being on the medial and one on the lateral side of each MOB (Ressler et al., 1994; Vassar et al., 1994).

The olfactory glomeruli are spherical regions of neuropil that form the first processing station of the olfactory pathway, where sensory axons form synapses on the apical dendrites of the principal cells (mitral and tufted cells) and on some intrinsic neurons (Figure 2A) (Pinching and Powell, 1971b; Kosaka et al., 1998; Shepherd et al., 2004).

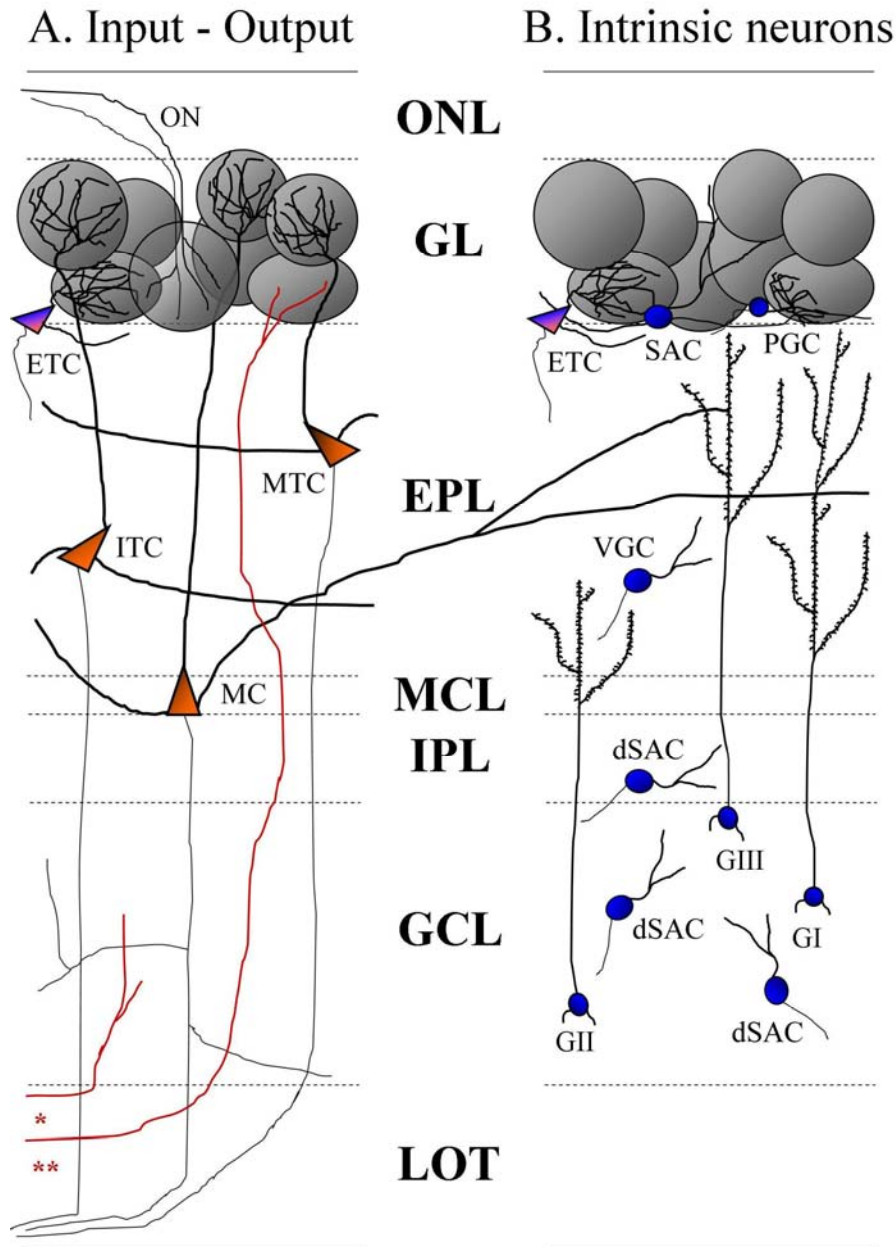


**Figure 2. Layout of neuronal components in the main olfactory bulb.** A. Input – Output and B. Intrinsic neurons. Abbreviations of layers: ONL: olfactory nerve layer, GL: glomerular layer, EPL: external plexiform layer, MCL: mitral cell layer, IPL: internal plexiform layer, GCL: granule cell layer, LOT: lateral olfactory tract. A. ON: olfactory nerve, Centrifugal afferents are from (indicated in red) \*: ipsi-, contralateral anterior olfactory nucleus; tenia tecta; primary olfactory cortex; horizontal limb of the diagonal band; locus coeruleus; raphe nuclei and \*\*: horizontal limb of the diagonal band; locus coeruleus; raphe nuclei. The output from the main olfactory bulb is carried by the axons of the principal cells, mitral (MC) and different types of tufted cells, external (ETC), middle (MTC), internal (ITC). B. Intrinsic neurons are organized into specific layers. PGC: periglomerular cell; SAC: short axon cell; VGC: Van Gehuchten cell; GI, GII, GIII: three types of granule cells; dSAC: deep short-axon cell.

They are clear examples of the principle of grouping neural elements and synapses into well defined modules. Their size ranges from 30-50  $\mu\text{m}$  in diameter in small mammals to 100-200  $\mu\text{m}$  in rabbits and cats (Allison, 1953).

### **III.1.1.2. Centrifugal inputs, neuromodulators**

The main olfactory bulb is under extensive and well defined control by different areas of the brain. The substantial number of inputs shows a particular laminar organization. Most centrifugal fibers arise from the following areas of the brain (Figure 2A):

- a. Olfactory cortex. One type of input is comprised of axon collaterals from pyramidal cells located in the primary olfactory cortex, also called the piriform cortex. These fibers terminate in the granule cell layer (GCL).
- b. Anterior olfactory nucleus. The terminals of axons that arise from different parts of both ipsi- and contralateral anterior olfactory nucleus in extensive numbers are also confined to the GCL.
- c. Brainstem. The brainstem sends noradrenalinergic fibers from the locus coeruleus that distribute evenly through the glomerular, internal plexiform and granule cell layers (Shepherd et al., 2004). Moreover, axonal fibers containing other neuromodulators, such as serotonin arrive from the dorsal and median raphe nuclei and, in different species, preferentially terminate in different layers of the MOB (Takeuchi et al., 1982; McLean and Shipley, 1987).
- d. Basal forebrain. One basal forebrain cholinergic center, the horizontal diagonal band also sends axons to granule cells, as well as to the periglomerular region (Hoffer et al., 1971).

As mentioned above it is notable that the olfactory bulb is enormously rich in a variety of neurotransmitters and -modulators. This is likely related to the fact that it mediates information that contributes to the generation of behaviors such as feeding, social organization and reproduction, which are controlled through these multiple types of neuroactive substances.

### III.1.2. Principal neurons

Several studies have provided a substantial body of evidence suggesting that the output of the MOB flows through axonal projections of two types of principal cells, the mitral (MC) and tufted cells (TC) (Figure 2A).

1. Mitral cells. The somata of most MCs are confined to the mitral cell layer in vertebrates, which is a thin and distinct layer 200-400  $\mu\text{m}$  deep to the glomerular layer. Having a diameter of 15-20  $\mu\text{m}$ , the cell bodies of MCs give rise to a single primary, apical dendrite which passes through the external plexiform layer (EPL) and branches into a tuft within a single glomerulus. Characteristic of MCs are the laterally directed secondary dendrites which do not branch extensively and terminate in the EPL. Unique is their length of at least 500  $\mu\text{m}$ , up to over one mm, in cases reaching up to halfway around the circumference of the bulb. MC axons give rise to recurrent collaterals, and after traversing through the internal plexiform layer (IPL) form the lateral olfactory tract (LOT). The major targets of the LOT are, primarily, layer Ia of the piriform cortex, as well as anterior olfactory nuclei, the olfactory tubercle, the entorhinal cortex, and portions of the amygdala. Pyramidal cell axons in the piriform cortex in turn project to several thalamic and hypothalamic nuclei and to the hippocampus and amygdala. Studies suggest that axonal targeting within the cortex is influenced by the molecular identity of the glomerulus serving as the source of sensory input for the given MC (Zou et al., 2001).

2. Tufted cells. Another major source of output is the more superficially located TCs. Three main groups can be identified according to their laminar location, they are termed: external (ETC), middle (MTC) and internal (ITC) tufted cells.

- a. External tufted cells. ETCs are a diverse population of neurons possessing a variety of dendritic branching and axonal projection patterns. Their axonal collaterals in the internal plexiform and granule cell layers contribute to an intrabulbar associational system, establishing connections between glomeruli of the medial and lateral sides of the MOB that receive input from ORNs expressing the same odorant receptor (Belluscio et al., 2002). Based on whether an ETC projects out of the MOB through the LOT or not, one can identify them as principal or intrinsic neurons, respectively.

- b. Middle tufted cells. The largest population, the MTCs, lie in the outer half (Bartolomei and Greer, 1998) of the external plexiform layer, they have a primary dendrite branching within a glomerulus and several thin secondary dendrites. Their axons, similar to mitral cells, after giving off collaterals join the LOT.
- c. Internal tufted cells. The third group is the ITCs, which exhibit similar properties to other TCs and due to their location overlap with superficially displaced mitral cells.

Despite the fact that tufted cells show many similarities to mitral cells, differences on the basis of molecular phenotype, somatic location, dendritic morphology, axonal connections, targets of extrabulbar projections, neurotransmitters and neuromodulators can be clearly established (Greer and Shepherd, 1982; Orona et al., 1984; Macrides et al., 1985; Mori, 1987; Bartolomei and Greer, 1998).

### **III.1.3. Local interneurons**

Several intrinsic cell types are distributed throughout the MOB (Figure 2B).

1. Juxtglomerular cells. Neurons with cell bodies in the glomerular layer also termed juxtglomerular cells (JGC) are located around the glomeruli, creating a cell-rich neuropil. It has long been recognized that JGCs are morphologically diverse and comprise periglomerular (PGC), short-axon cells (SAC), and ETCs (Cajal, 1911; Pinching and Powell, 1971a; Shepherd et al., 2004).
  - a. Periglomerular cells. The smallest of interneurons are the PGCs with a somatic diameter of 6-8  $\mu\text{m}$ . Their single, short and bushy dendrite arborizes into a small, spine-bearing dendritic tuft, occupying 15-20% of a glomerulus. In some instances bitufted PGCs can also be observed. With the exception of some that lack axons, they innervate extraglomerular regions laterally up to a few glomeruli away (Pinching and Powell, 1971a, c; Shepherd et al., 2004).
  - b. External tufted cells. Among the JGCs, ETCs have the largest somata (10–15  $\mu\text{m}$ ) and have a single, relatively sparse, fan-shaped apical dendritic tuft that most often arborizes in a single glomerulus. Most ETCs are thought to lack secondary dendrites. However, ETCs with

basal dendrites have also been described, as have ETCs with apical tufts ramifying in two glomeruli (Pinching and Powell, 1971a; Macrides and Schneider, 1982; Hayar et al., 2004a; Shepherd et al., 2004) indicating the morphological heterogeneity of these cells.

- c. Short-axon cells. These interneurons of the glomerular layer have an intermediate soma size and are distinguished by dendrites that arborize around the glomeruli in the periglomerular region without forming an apical tuft (Pinching and Powell, 1971a; Aungst et al., 2003; Shepherd et al., 2004).

Juxtglomerular cells are diverse, based on their active and passive electrical properties and their synaptic connectivity (Puopolo and Belluzzi, 1998a; McQuiston and Katz, 2001; Hayar et al., 2004a; b). Recently, Hayar *et al.* (2004b) have functionally characterized several JGCs and found robust differences between PGCs, ETCs and SACs, but most physiological properties of the ETCs were found to be rather uniform.

2. Van Gehuchten cells. Although, the external plexiform layer is mainly occupied by primary and secondary dendrites of M/TCs and somata of TCs and displaced MCs, interneurons first identified by Van Gehuchten can also be observed in this layer.
3. Granule cells. Deep to the mitral cell and internal plexiform layers lies the granule cell layer, a 300-400  $\mu\text{m}$  thick band of neuropil containing the cell bodies of granule cells (GC), which reside preferentially in clusters. They possess one radial dendrite extending up to different depths of the external plexiform layer, and a few deep processes that branch sparingly. Their dendrites bear numerous spines, also termed gemmules, that are larger but less in number than e.g. pyramidal cell dendritic spines in the cerebral cortex. Another unique feature of GCs is that they lack axons. This has been repeatedly confirmed using the Golgi impregnation method and electron microscopy. It has been suggested earlier that GCs at different depths could serve different functional roles in olfactory circuitry (Shepherd, 1972). There are 3 major types of granule cells, superficial (Figure 2B, GIII), deep (GII) and intermediate (GI) GCs, with

dendritic ramifications mainly in superficial, deep parts or throughout the entire area of the external plexiform layer, respectively.

4. Deep short-axon cells. Similar to the glomerular layer, only in higher number, a third type of interneurons resides in granule cell layer, the inframitral deep short-axon cells (dSAC). They exhibit a variety of dendritic trees and axonal arbors within the external plexiform and granule cell layers based on which they have been subdivided into four groups (Cajal, 1911; Pinching and Powell, 1971a; Schneider and Macrides, 1978). So far, little is known about their functional and structural properties, or their place in the circuitry of the olfactory bulb.

In the olfactory bulb convergence is one the main principles of organizing of cellular components. In rodents, an estimate of the number of olfactory receptor neurons is approximately  $20 \times 10^6$ , giving rise to as many axons targeting each olfactory bulb. Within one MOB they converge onto 1800-2000 glomeruli to which an estimated 50000 MCs and 100000 TCs are connected (Allison, 1953). This yields convergence ratios of 10000:1 onto glomeruli, 400:1 onto MCs and 200:1 onto TCs. Ratios of intrinsic neurons onto principal cells are also high, an estimated 20:1 PG to MC, 50-100:1 GC to MC and 1:1 SAC to MC (Shepherd, 1972). These rough estimates indicate an extensive intrinsic circuitry for olfactory information processing.

### **III.2. Synaptic connectivity in the main olfactory bulb**

The main olfactory bulb was one of the first brain regions where identification of synaptic communication was made. The variety of principal and intrinsic neurons gives rise to a wide array of intrinsic circuits for sensory information processing in the bulb.

#### **III.2.1. Synapses in the glomerular layer**

The identity of a single glomerulus can be defined based on the molecular phenotype of the olfactory receptor neuron populations targeting it. It is the first processing station of the olfactory pathway, where sensory axon terminals establish axo-dendritic contacts with dendritic tufts of both mitral/tufted cells and subpopulations of juxtglomerular cells (periglomerular and external tufted cells) (Pinching and Powell, 1971a, c; Kasowski et al., 1999) (Figure 3A).

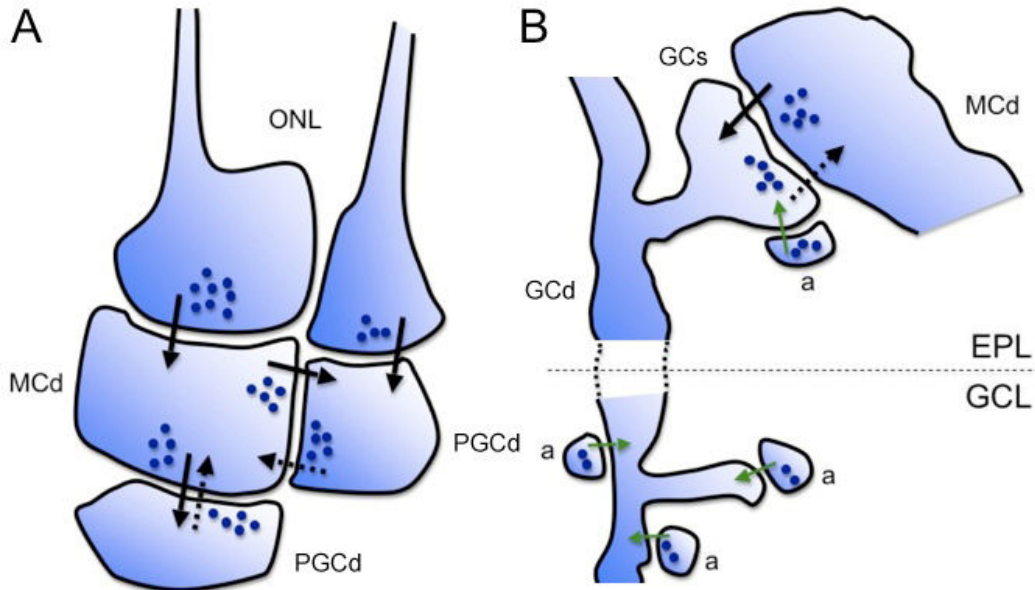


**Figure 3. Synaptic connections within the glomerular and external plexiform layers in the main olfactory bulb.** A. The typical synaptic arrangement within the glomerulus is shown, which includes axo-dendritic and dendro-dendritic connections. B. Granule cell spines (GCs) establish reciprocal dendro-dendritic synapses with mitral cell secondary dendrites (MCd) in the EPL (solid and dashed black arrows: excitatory and inhibitory connections, respectively). Furthermore, axon terminals of centrifugal afferents, recurrent collaterals and deep short-axon cells impinge onto GC dendrites in the GCL (green arrows). Abbreviations: ONL, EPL, GCL: olfactory nerve, external plexiform, granule cell layers, respectively; PGCd: periglomerular cell dendrite; GCd: GC dendrite; a: axons.

These synaptic contacts are type I (Gray, 1959), excitatory synapses. A special feature of dendrites within a glomerulus is that they not only receive sensory input, but are themselves presynaptic to JGCs. Complex dendro-dendritic interactions occur within the glomeruli between principal cells and JGCs (Kosaka et al., 1998; Kosaka et al., 2001; Hayar et al., 2004b; Shepherd et al., 2004; Hayar et al., 2005; Kosaka and Kosaka, 2005) (Figure 3A).

The most common of connections is excitatory from M/TC to PGC. Synaptic communication in the opposite direction, from PGC to M/TC, is another frequently observed pattern which comprise type 2 (Gray, 1959) inhibitory synapses. These two types of synapses are arranged mainly in reciprocal, side-by-side pairs. Periglomerular cells may also receive inhibition from other PGC dendrites or short-axon cell axons (White, 1972). This complex synaptic arrangement is well organized; the axo-dendritic

and dendro-dendritic synapses are isolated by astroglial processes, although the individual synapses are not wrapped around with this glial sheath. This unique organization may facilitate the synchronization of postsynaptic activity by allowing the diffusion of neurotransmitter (Carlson et al., 2000; Schoppa and Westbrook, 2001). Contributing to this extensive synaptic mosaic are axon terminals of centrifugal fibers from various brain regions and short-axon cells which serve to mediate flow of sensory information between glomeruli. Several channels of synaptic communication serve to connect individual glomeruli. On one hand, PGC axons terminate in inhibitory synapses onto somata and dendrites of PGCs, ETCs and M/TCs. Tufted cell somata and stem dendrites very rarely receive any synapses other than those from the axon terminals of PGCs and from gemmules of GCs (see later). Occasionally, however, asymmetrical, type 1 synapses are present on the cell somata or stem dendrites from axon terminals containing spherical vesicles (Pinching and Powell, 1971a, c).

### **III.2.2. Synapses in the external plexiform layer**

In the external plexiform layer (EPL) the dominant type of synaptic connection is a widely spaced sequence of pairs of reciprocal synapses between secondary dendrites of mitral/tufted cells and the gemmules of granule cells (Hirata, 1964; Rall et al., 1966; Jahr and Nicoll, 1980; Chen et al., 2000; Shepherd et al., 2004) (Figure 3B). These were the first dendro-dendritic synapses identified in the nervous system. In the reciprocal pair, similar to the ones in the glomerulus, MC-to-GC is excitatory, whereas GC-to-MC is inhibitory. This type of connection comprises more than 80% of all synapses in the EPL. Given the fact that the secondary dendrites of M/TCs occupy separate fields in the EPL, it is possible that the microcircuits they contribute to are separated as well. It is important to note that there aren't any synapses on primary dendrites of M/TCs. In addition, in the EPL axon terminals of short-axon cells and centrifugal fibers can be observed which, without exception, impinge onto GC spines through presumably excitatory synapses (Price and Powell, 1970c).

### **III.2.3. Synapses in the granule cell layer**

Axon terminals contacting dendritic spines of GCs in the granule cell layer originate from both intrinsic and centrifugal sources (Figure 3B). Intrinsic input include

excitatory M/TCS and, presumably, inhibitory deep short-axon cells. Centrifugal excitatory terminals can be found at different depths within the granule cell layer. For example, fibers arising from the contralateral anterior olfactory nucleus (AON) run through the anterior commissure to target mainly deep processes. The axons from the ipsilateral AON, however, distribute over the middle regions of dendritic area and the horizontal diagonal band projects primarily to spines in the external plexiform layer. The key site for gating and modulating processing of olfactory information, it seems, is the dendritic spine of GCs, the reciprocal MC-GC-MC connection, making it a multifunctional synapse.

### **III.3. Functional and structural diversity of interneurons**

Information processing in a neuronal network does not only depend on the structural building blocks of synaptic circuitry but also on the electrophysiological properties of neuronal elements and how these are influenced by neurochemical substances. Two neurons possessing similar morphological features may respond to the same input in a very different manner due to their diverse intrinsic electrical properties.

Synaptic integration within a glomerulus involves a multineuronal circuitry. Within a glomerulus the sensory axons of olfactory receptor neurons synapse onto an extensive neuron population of juxtglomerular cells (JGC) that comprise periglomerular, short-axon cells, and ETCs. Despite their large number and strategic location, little is known about the electrophysiological characteristics or the morphological heterogeneity of these cells. Although a few studies have functionally characterized several JGCs and robust differences were found between ETCs, their functional roles in olfactory information processing remain poorly understood.

The extraordinary diversity of nerve cells was already recognized over a century ago (Cajal, 1911). It is now widely accepted that within most brain regions, the glutamatergic principal cells are rather homogeneous, whereas the GABAergic non-principal cells, or interneurons (IN), form a much more diverse population (Freund and Buzsaki, 1996; Kosaka et al., 1998; Somogyi et al., 1998; McBain and Fisahn, 2001; Markram et al., 2004). Traditionally, the classification of IN types has relied primarily

on their axonal and dendritic morphologies. However, recently their intrinsic electrical properties, gene expression profiles and firing behavior in relation to ongoing network activity have all been taken into account. Such combined molecular, morphological and physiological approaches have provided compelling evidence for the astonishing diversity of INs and for the variety of roles they play in neuronal networks. The classical view regarding the connectivity of INs has been that they primarily innervate the principal cells, and to a smaller extent each other. However, additional populations of hippocampal and neocortical INs have been revealed (Acsady et al., 1996; Gulyas et al., 1996; Meskenaite, 1997; Gulyas et al., 2003) that are specialized to selectively control the activity of other GABAergic INs, and the presence of such cells has also been suggested to occur in the main olfactory bulb (Mugnaini et al., 1984; Gracia-Llanes et al., 2003).

As in many other brain regions, the GABAergic periglomerular and granule cells also receive GABAergic inputs (Price and Powell, 1970b; Pinching and Powell, 1971b; Puopolo and Belluzzi, 1998b; Nusser et al., 1999; Smith and Jahr, 2002; Murphy et al., 2005; Pressler and Strowbridge, 2006), but their source is largely unknown. A recent report (Pressler and Strowbridge, 2006) has demonstrated that GCs receive GABA<sub>A</sub> receptor-mediated inhibition from a subpopulation of infra-mitral deep short-axon cells called Blanes cells, but it remains to be seen whether other cell types also contribute to the GABAergic control of GCs. Short-axon cells form another, rather diverse GABAergic IN population distinct from the numerically dominant GCs and PGCs (Cajal, 1911; Price and Powell, 1970a; Schneider and Macrides, 1978; Mugnaini et al., 1984). However, very little is known about their axonal arborizations, their intrinsic electrical properties, their synaptic inputs and their postsynaptic targets.

To understand the cellular and synaptic mechanisms of olfactory information processing, the intrinsic properties and synaptic connectivity of these different types of nerve cells need to be deciphered. This requires the identification of whether structural and functional heterogeneity correlates with each other, resulting in well defined subpopulations of cells; or whether these measured features of the cells vary independently, resulting in a single but highly diverse population.

#### IV. AIMS

First, I aimed to characterize the intrinsic electrical and morphological properties of external tufted cells (ETCs) in the rat main olfactory bulb. Based on a large number of measured physiological and morphological parameters, I asked whether:

1. External tufted cells comprise a *single* population or *multiple subpopulations* exist, and whether
2. The pattern of *dendritic arborization* of ETCs could be *predicted* from their active and passive *electrical properties* and vice versa.

Second, I aimed to provide a combined characterization of deep short-axon cells, by carrying out a detailed analysis of their

1. intrinsic *electrophysiological properties* and *synaptic inputs*,
2. *molecular content* and
3. *axo-somato-dendritic morphologies*

in order to reveal their place in the olfactory bulb network.

## V. METHODS

### V.1. Acute slice preparation and electrophysiological recordings

For my experiments I used male Wistar rats (20–78 days old), which were anesthetized with ketamine (50 mg per animal) in accordance with the ethical guidelines of the Institute of Experimental Medicine, Hungarian Academy of Sciences (license number: 2288/003/Főv/2006). After decapitation, the brain was removed and placed into ice-cold artificial cerebro-spinal fluid (ACSF) containing (in mM): 230 sucrose, 2.5 KCl, 25 glucose, 1.25 NaH<sub>2</sub>PO<sub>4</sub>, 24 NaHCO<sub>3</sub>, 4 MgCl<sub>2</sub>, and 0.5 CaCl<sub>2</sub>. Horizontal or sagittal slices from the olfactory bulb were cut at 300 µm thickness with a Vibratome (Leica VT1000S; Leica Microsystems, Vienna, Austria) and were stored in ACSF containing (in mM): 85 NaCl, 75 sucrose, 2.5 KCl, 25 glucose, 1.25 NaH<sub>2</sub>PO<sub>4</sub>, 24 NaHCO<sub>3</sub>, 4 MgCl<sub>2</sub>, and 0.5 CaCl<sub>2</sub>. After 30 minutes, this medium was gradually or instantly replaced with normal ACSF containing (in mM): 126 NaCl, 2.5 KCl, 25 glucose, 1.25 NaH<sub>2</sub>PO<sub>4</sub>, 24 NaHCO<sub>3</sub>, 2 MgCl<sub>2</sub>, and 2 CaCl<sub>2</sub>. All extracellular solutions were bubbled continuously with 95% O<sub>2</sub> and 5% CO<sub>2</sub>, resulting in a pH of 7.4. After an additional 30-60 minute period of recovery at 33°C, slices were incubated at room temperature until they were transferred to the recording chamber.

I performed cell-attached and somatic whole-cell current and voltage recordings at 31-36°C. Cells were identified with an infrared differential interference contrast or an oblique illumination technique using an Olympus BX50WI microscope and a 40x water immersion objective. External tufted cell (ETC) recordings were carried out from somata with a diameter of >10 µm and with a juxtglomerular location (within the glomerular layer or at the border of the external plexiform layer and glomerular layer, but not within the external plexiform layer.) Deep short-axon cell (dSAC) recordings were carried out from visually identified cells with a somatic diameter of >10 µm located in the inframitral layers. For current-clamp experiments, I used a potassium gluconate-based intracellular solution containing (in mM): 120 K-gluconate, 5 KCl, 2 MgCl<sub>2</sub>, 0.05 EGTA, 10 HEPES, 2 Mg-ATP, 0.4 Mg-GTP, 10 creatinine phosphate, and 5.3-8 biocytin (pH=7.25; osmolarity: 270–290 mOsm). Using intracellular solutions containing 5.3-8 mM biocytin allowed us visualization and *post hoc* anatomical analysis

of recorded cells following electrophysiological recordings. After establishing the whole-cell configuration, if needed, hyper- or depolarizing DC current injections were applied to maintain cells at membrane potentials just below firing threshold. In ETCs, trains of action potentials were evoked by injecting one-second long depolarizing current pulses of different amplitudes (20-200 pA); in dSACs, by injecting one-second long depolarizing current pulses of 100 pA in amplitude. The passive properties were derived from single exponentials fitted to average traces of membrane voltage responses to small (1-20 pA, 400 ms) hyper- and depolarizing current injections. For testing the subthreshold resonance properties of ETCs, two-second long sinusoidal (0.5-60 Hz) currents (amplitudes from 5 to 40 pA) were injected into the cells.

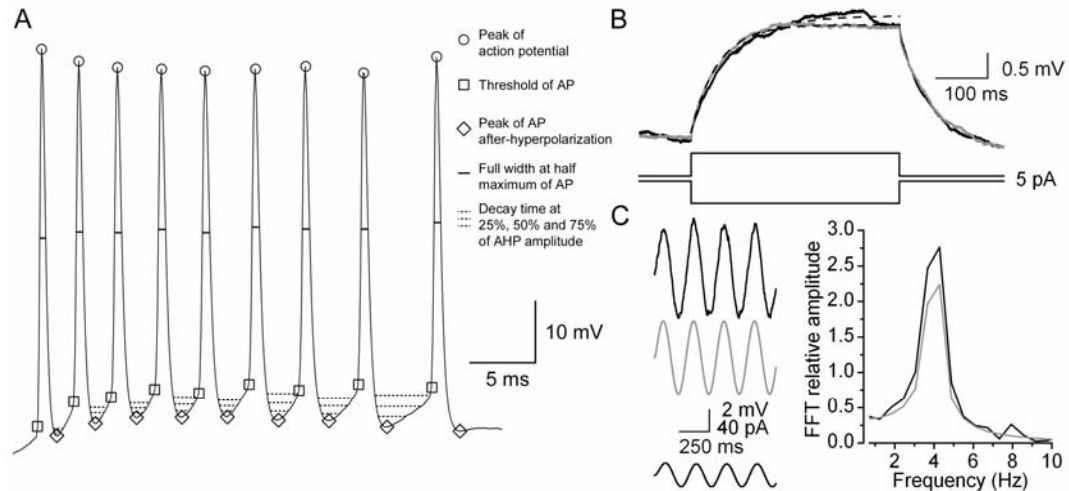


**Figure 4. Measurements of physiological properties of external tufted cells.** A. somatic DC current injection-evoked spike train is shown. Parameters such as the action potential (AP) threshold, peak amplitude, full width at half maximum, AP after-hyperpolarization (AHP) amplitude and width at 25%, 50%, 75% decay were automatically measured with a custom-made software. B. Passive membrane properties (input resistance and membrane time constant,  $R_{in}$  and  $\tau$ , respectively) of ETCs were derived from single exponential fits (dashed lines) to averaged (of 50-100 traces) voltage responses to small (1-20 pA, 400 ms) hyper- (gray trace, inverted) and depolarizing (black trace) current injections. C. For testing subthreshold resonance properties, two-second long sinusoidal currents (0.5-60 Hz, 5-40 pA, 2 s) were injected into the cells (bottom black trace). The voltage responses of the cells (black trace) were then compared to responses of a single compartment model cell with passive membrane properties (gray trace) following fast Fourier transformation. (ETC response: black; passive model: gray).

The peak amplitude of the fast Fourier transform of the voltage responses were then compared to that of a single compartment passive resistance-capacitance model cell, which was generated in Berkeley Madonna 8.0.1 (written by R.I. Macey and G.F. Oster at UC Berkeley, CA, USA).

During paired recordings of dSACs and granule cells the same intracellular solution described above was used for recording from the presynaptic dSACs. Three to five ms 2.5-4.0 nA currents were injected to evoke a single spike, which was repeated at either 25 or 50 Hz to evoke pairs of action potentials. To isolate AMPA receptor-mediated excitatory postsynaptic currents (EPSCs), cells were voltage-clamped at -70 mV in the presence of 20  $\mu$ M SR95531 and 50  $\mu$ M D-AP5 in the bath solution. To examine spontaneous and action potential-evoked inhibitory postsynaptic currents (IPSCs), I used a mixed potassium gluconate and potassium chloride internal solution containing (in mM): 90 K-gluconate, 40 KCl, 2 MgCl<sub>2</sub>, 0.05 EGTA, 10 HEPES, 2 Mg-ATP, 0.4 Mg-GTP, 10 creatinine phosphate, and 8 biocytin (pH=7.33; osmolarity: 270–290 mOsm). For recording spontaneous IPSCs, cells were voltage-clamped at -80 mV and recordings were carried out in the continuous presence of 20  $\mu$ M CNQX (Tocris Cookson, Bristol, UK) and 50  $\mu$ M D-AP5 in the bath solution. Miniature synaptic events were recorded in the presence of 1  $\mu$ M tetrodotoxin (Alomone Labs, Jerusalem, Israel) to block voltage-gated sodium channels. During paired recordings, postsynaptic granule cells were recorded with this same mixed potassium gluconate and potassium chloride intracellular solution, they were voltage-clamped at -80 mV, but CNQX and D-AP5 were not included in the extracellular solution.

To investigate whether deep to superficial GABAergic connections exist in the main olfactory bulb, electrical stimulation of the internal plexiform layer (IPL) was carried out. A bipolar tungsten stimulating electrode (World Precision Instruments, Inc., Sarasota, FL, USA) was placed into the IPL and brief (350  $\mu$ s, 0-100  $\mu$ A) electrical pulses were delivered through an A395 Linear Stimulus Isolator (World Precision Instruments, Inc., Sarasota, FL, USA). Evoked IPSCs were recorded from periglomerular cells using the above described mixed potassium gluconate and potassium chloride intracellular solution in the presence of 5  $\mu$ M NBQX (Tocris Cookson, Bristol, UK) and 5  $\mu$ M R-CPP in the bath solution; the cells were clamped at -80 mV. The GABA<sub>A</sub> receptor blocker, 20  $\mu$ M picrotoxin was then washed in.

To ensure the time independence of my data during the recordings I applied the following criteria. The access resistance ( $R_a$ ) was subject to 75% compensation, and was continuously monitored. If  $R_a$  changed >15% during the recording, the cell was discarded from the analysis. All recordings were rejected if the  $R_a$  became >15M $\Omega$ . Recordings were performed with a dual-channel MultiClamp 700A amplifier (Axon Instruments, Foster City, CA, USA). Patch pipettes (3–8 M $\Omega$ ) were pulled (Zeitz Universal Puller; Zeitz-Instrumente Vertriebs, Munich, Germany) from thick-walled borosilicate glass capillaries with an inner filament (1.5 mm outer diameter, 0.86 mm inner diameter; Sutter Instruments, Novato, CA, USA). Data were digitized on-line at 10 or 20 kHz, and analyzed with EVAN 1.3 (Nusser et al., 2001a) and with an in-house analysis software (SPIN 1.0.1.) written in Matlab (Matlab 7.0, The MathWorks Inc., Natick, MA, USA).

## **V.2. Visualization of the recorded cells**

All of the anatomical work, including processing of slices, light and subsequent electron microscopy, *post hoc* reconstruction and anatomical analysis of recorded cells were performed by my colleague, Dr. Mark D. Eyre Ph.D. (Laboratory of Cellular Neurophysiology, Institute of Experimental Medicine).

After recordings, slices were placed in a fixative containing 4% paraformaldehyde, 1.25% glutaraldehyde and 15% v/v picric acid in 0.1 M phosphate buffer (PB; pH=7.4) at 4°C for at least 24 hours. Before processing, the fixative was thoroughly washed out with 0.1 M PB. Slices were then cryoprotected 10 and 20% sucrose solutions (in 0.1 M PB) for 45 minutes followed by freezing in liquid N<sub>2</sub> and thawing in PB. After several washes in PB, slices were embedded in gelatin and re-sectioned at 60  $\mu$ m in thickness. Biocytin was visualized using avidin–biotin–horseradish peroxidase complex overnight (ABC; Vector Laboratories, Burlingame, CA, USA) followed by a reaction with 3'3'-diaminobenzidine tetrahydrochloride (DAB, 0.05% solution in Tris buffer, pH=7.4) as chromogen and 0.01% H<sub>2</sub>O<sub>2</sub> as oxidant for 12 minutes. Sections were then postfixated in 1% OsO<sub>4</sub> for 20 minutes, stained in 1% uranyl acetate for 25 minutes, dehydrated in a graded series of ethanol, and embedded in epoxy resin (Durcupan).

This protocol extensively labeled the biocytin-filled cell processes and masked epitopes for post-embedding immunolabelling (see below), so in a number of slices an

alternative method was used to visualize the biocytin. After freezing and re-sectioning, slices were incubated with ABC overnight, followed by tyramide for 10 minutes (1:50 in solvent supplied; biotinylated TSA kit; Perkin-Elmer, Waltham, MA, USA). Slices were then blocked in tris-buffered saline (TBS) with 3% bovine serum albumin (BSA), 0.1% cold water fish skin gelatin (CWFSG; Aurion, Wageningen, The Netherlands) and 0.05% sodium azide for 60 minutes and then incubated with streptavidin-conjugated 1 nm gold particles (1:50, Aurion) in TBS with 0.8% BSA, 0.1% CWFSG and 0.05% sodium azide overnight. Sections were then treated with 2% glutaraldehyde in TBS for 10 minutes, followed by silver enhancement (Aurion SE-LM kit) for 30 minutes at 25°C. Slices were then postfixed in 0.5% OsO<sub>4</sub> at 4°C for 15 minutes, stained in 1% uranyl acetate for 25 minutes, and dehydrated and embedded in Durcupan as above. For the retrogradely labeled cells (see below), prior to the ABC-DAB reaction the biocytin was visualized with Alexa488 or Cy5 conjugated to streptavidin and the colocalization of biocytin and the fluorescent microspheres was confirmed using confocal laser scanning microscopy.

### **V.3. *In vivo* injection of fluorescent microspheres**

*In vivo* injections were also performed by Dr. Mark D. Eyre Ph.D. Male Wistar rats (n=11 rats; 28-42 days old) were anaesthetized with 2 ml/kg of a 1:1 mixture of Ketamine and Xylazine and were mounted in a stereotaxic apparatus. Solutions of 40 nm diameter fluorescent latex microspheres (as supplied by Molecular Probes) were pressure injected (100-300 nl) into the anterior olfactory nucleus, the olfactory tubercle, the piriform cortex and the deep endopiriform nucleus. Three to 14 days after the surgery, acute horizontal slices from the main olfactory bulb were prepared as described above and with the aid of an appropriate fluorescence filter, fluorescently labeled cells with inframitral somatic locations were subject of whole-cell recordings.

### **V.4. Immunofluorescent microscopy**

In some cases, slices with recorded and biocytin-filled cells were fixed after recordings as above except the glutaraldehyde concentration in the fixative was only 0.05% and the fixative was thoroughly washed out after 3 hours. Slices were then cryoprotected, freeze-thawed and re-sectioned as above. Slices were blocked in TBS with 10% normal

goat serum (NGS; Vector Laboratories) for one hour, and then incubated overnight with anti-GABA<sub>A</sub> receptor  $\alpha$ 1 subunit primary antibodies (diluted 1:500; gifts of Prof. J-M. Fritschy and Prof. W. Sieghart) in TBST containing 2% NGS (TBS with 2% NGS and 0.05% Triton X-100). Sections were then washed and incubated in a mixture of either streptavidin conjugated to Alexa488 and goat-anti-rabbit IgG conjugated to Cy3 or streptavidin conjugated to Cy5 and goat-anti-rabbit IgG conjugated to Alexa-488 (all diluted in 2% NGS TBST; Alexa dyes from Invitrogen, Eugene, OR, USA; Cy dyes from Jackson ImmunoResearch, West Grove, PA, USA) for two hours. Slices were then washed in TBS and mounted. When fluorescent immunolabeling of periglomerular cells for tyrosine hydroxylase and calbindin was carried out, slices were similarly cryoprotected, freeze-thawed, re-sectioned and blocked with TBS in 10% NGS as described above. Slices were then incubated overnight with mouse anti-tyrosine hydroxylase (diluted 1:1000, DiaSorin, Saluggia, Italy) and rabbit anti-calbindin primary antibodies (diluted 1:1000, Oncogene Research Products, San Diego, CA, USA) in TBST containing 2% NGS (TBS with 2% NGS and 0.05% Triton X-100). The sections were then washed and incubated in a mixture of streptavidin conjugated to Alexa488, goat-anti-rabbit IgG conjugated to Cy3 and goat-anti-mouse IgG conjugated to Cy5 (all diluted 1:500 in TBS with 2% NGS and 0.05% Triton X-100). The colocalization of biocytin and the GABA<sub>A</sub> receptor  $\alpha$ 1 subunit or the presence of tyrosine hydroxylase and calbindin was then confirmed by using an Olympus BX62 microscope equipped with appropriate fluorescence filters and a DP30BW CCD camera or an Olympus FV1000 confocal microscope. Biocytin was subsequently visualized with the ABC-DAB method and the slices were similarly dehydrated and embedded in Durcupan as above.

#### **V.5. Three-dimensional reconstructions of deep short axon cells**

Labeled cells were identified as ETCs or dSACs from their size, the location of their somata and their dendritic morphology. Neurons with no obvious truncations in their dendrites or no obvious truncations in their dendrites and axons, in the case of ETCs or dSACs, respectively, were fully reconstructed with the NeuroLucida system (MicroBrightField Europe, Magdeburg, Germany) attached to a Zeiss Axioscope 2 microscope using a 100x oil-immersion objective, and were subjected to morphometric

measurements.

### **V.6. Electron microscopy and postembedding immunolabeling**

Portions of cells were re-embedded and serial sections were cut at 60 nm thickness using an ultramicrotome (Ultracut; Leica Microsystem, Vienna, Austria). Sections were collected alternately onto copper and nickel phloform-coated slot grids. Sections on nickel slot grids were subjected to postembedding immunoreactions for GABA, modified from Somogyi & Hodgson (1985). Briefly, slot-grids were treated with 1% periodic acid for 8 minutes, followed by blocking with 50 mM glycine in 0.081% NaCl TB (TBS) and 1.5% BSA in TBS for 90 minutes. This was followed by incubation in primary rabbit-anti-GABA antibodies (GABA9; diluted 1:500; gift of Prof. P. Somogyi) in TBS containing 1.5% BSA for 90 minutes. The reaction was visualized with 10 nm gold-conjugated goat-anti-rabbit secondary antibodies (British Biocell International, Cardiff, UK; diluted 1:50 in TB with 1% BSA and 0.5% Tween-20). Sections were contrasted with uranyl acetate and lead citrate and viewed using a JEOL1011 electron microscope. Digital images were captured with a cooled CCD camera (Cantega; Soft Imaging System, Munster, Germany). Ultrastructurally identified mitral/tufted cell apical and lateral dendrites were consistently immunonegative, verifying the specificity of our anti-GABA immunoreactions.

### **V.7. Statistical procedures**

Throughout my dissertation, all data are expressed as mean  $\pm$  standard deviation. In ETCs recordings, to ensure that variability in the physiological parameters was not the consequence of different time elapsed from the establishment of the whole-cell configuration, I measured all active and passive electrical properties at the beginning and at the end of the whole-cell recording period. Following Shapiro-Wilk normality test, either paired t-test or sign-test was used to compare data measured at the beginning and at the end of the recording. Parameters that significantly ( $p < 0.01$ ) changed during the whole-cell recordings were discarded from my analysis. I utilized Pearson's regression analysis to determine whether the measured physiological parameters depended on the amplitudes of the injected current (20, 40 and 70 pA). Parameters where a significant correlation ( $p < 0.01$ ) was found were also discarded from my

analysis. Principal component analysis (PCA; (Jolliffe and Morgan, 1992) and agglomerative clustering methods were carried out with the Statistica 6.0 software (StatSoft, Inc., Tulsa, OK, USA). Briefly, the aim of PCA is to reduce the number of parameters describing a population to a smaller number of ‘factors’, which account for a large fraction of the total variance in the population. Only factors with large Eigenvalue (usually >1) are selected to represent the population. PCA also transforms the data to standard scores, removing any potential bias due to the fact that parameters are in different units. Agglomerative or joining clustering was employed to group data (PCA factors) without any *a priori* assumption concerning the number of clusters. Dissimilarities between cells were measured as Euclidean distances and Ward’s amalgamation rule was used to determine cluster linkage. The joining tree indicated clusters of differing sizes depending on the degree of dissimilarity. For analysis of ETCs the number of clusters that were statistically different from one another was determined by calculating the squared Euclidean distance of each cell from the center of each cluster. The coordinates of each cluster centre in a multidimensional space along each axis (i.e. for each factor used in the clustering) were calculated as the average of each factor score for cells assigned to that cluster by the joining tree. Distances of cells in each cluster from each center were then compared. Specifically, we first tested the validity of two clusters by calculating the centers of cluster 1 and 2, and then the distances of each member from each center. By using Mann-Whitney-U test, we statistically compared the mean distance of the members of cluster 1 and 2 from the center of cluster 1. Then the reverse comparison was carried out (members of cluster 1 and 2 from the center of cluster 2). If both of these tests were statistically significant ( $p < 0.001$ ), then we concluded that ETCs form two subpopulations. Subsequently, a similar statistical comparison was carried out with 3 clusters, 4 clusters etc. using a Kruskal-Wallis non-parametric test, and if significant, a *post hoc* test (multiple comparisons of mean ranks for all groups) was used to decide whether the groups were different or not. None of our analyses revealed 3 or more subpopulations with significant difference between all subgroups.

Following dSAC recordings, the data were subject to the Shapiro-Wilk normality test, and the Levene and Brown-Forsythe or Hartley F-max tests for homogeneity of variances. To compare averaged spontaneous and miniature synaptic events within

subtypes I employed the t-test for dependent samples or the Wilcoxon matched pairs test. At the individual cell level, I carried out comparisons using a non-parametric Kolmogorov-Smirnov test. Either parametric ANOVA or non-parametric Kruskal-Wallis ANOVA was used to compare data between dSAC subtypes, depending on whether the distribution was normal or not. Where appropriate, data were further assessed by conducting a *post hoc* test (Tukey's Unequal n HSD test or multiple comparisons of mean ranks, respectively). All differences were considered significant if  $p < 0.05$ . Morphological data was subjected to PCA. The first 4 factors had Eigenvalues greater than 1 and were then used for agglomerative clustering of Euclidean distances using Ward's method. The gap statistic method (Tibshirani et al., 2001) was used to determine the number of clusters. All analyses (including analysis of parameter correlations, PCA and unsupervised clustering) were performed using the Statistica 6.0 software (StatSoft, Inc., Tulsa, OK, USA; [www.statsoft.com](http://www.statsoft.com)). The gap statistic calculation was implemented as a macro within the Statistica software.

## VI. RESULTS AND CONCLUSIONS

### VI.1. Correlation of functional and structural characteristics predicts two subpopulations of external tufted cells.

#### VI.1.1. Active and passive electrical properties of external tufted cells

To ensure an unbiased, representative sampling of the external tufted cell (ETC) population, I randomly selected juxtglomerular cells with a somatic diameter of  $>10\mu\text{m}$  without any additional selection criterion (e.g. soma shape, number of emerging dendrites etc). I paid particular attention to ensure that only cells with somata located in the glomerular layer (GL) and not within the external plexiform layer (EPL) were selected. All cells were filled with biocytin and were subject to *post hoc* morphological identification. Several cells with somatic diameter of  $>10\ \mu\text{m}$  were subsequently identified as short-axon cells, which were discarded (i.e. only anatomically identified ETCs were included in my work). First, I assessed the spontaneous spiking activity of the ETCs in cell-attached recording configuration. The recorded cells displayed large heterogeneity based on their spontaneous firing behavior. A large proportion (57%) fired bursts of action potentials (APs; from 0.03 to 8 Hz), some (25%) fired individual APs at frequencies ranging from 0.1 to 38 Hz, and the remaining 18% of the cells were completely silent. This spontaneous activity was also observed during the first minute of whole-cell recordings, similar to that found by Hayar et al. (2004a). When a cell showed spontaneous suprathreshold activity, small hyperpolarizing DC current was injected to keep the membrane potential just below firing threshold. Under such conditions, trains of action potentials were evoked by injecting one-second long depolarizing currents of different amplitudes into the cells (Figure 4, see Methods and materials).

The firing patterns of ETCs were extremely diverse (Figure 5); qualitative descriptions commonly used to characterize such patterns are regular spiking, irregular spiking with accommodation and burst firing. Eighty eight percent of the cells that showed spontaneous bursting in the cell attached configuration also displayed bursts of APs upon DC current injections. In 82% of the cells that did not fire bursts spontaneously, somatic current injections evoked regular and irregular firing patterns.

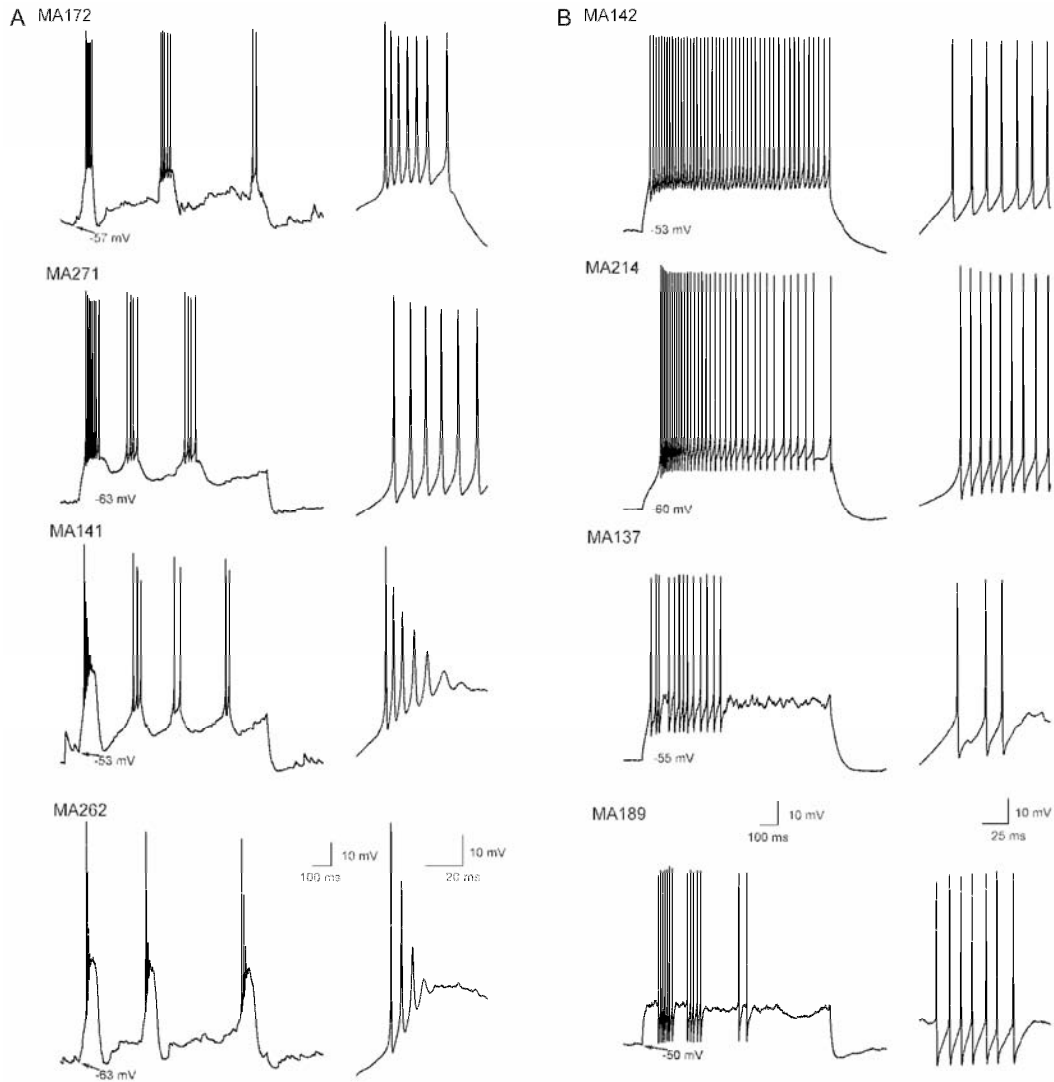


**Figure 5. Diverse action potential firing patterns of individual external tufted cells.** Whole-cell voltage recordings of suprathreshold responses to depolarizing current injections from ETCs. Although, the firing patterns of the members of cluster 1 (A) are clearly different from those in cluster 2 (B), large within-group variability is also apparent. In all panels, the first part of the trace is shown on an expanded timescale on the right.

Of the silent cells 37.5% fired bursts of APs and the remaining 62.5% were non-bursting following somatic current injections. To quantitatively characterize the spikes of ETCs, I measured (Figure 4A) the threshold, peak amplitude, full width at half maximum of the first and last APs of the train, the amplitude of spike after-hyperpolarization (AHP) and decay times at 25, 50 and 75% of AHP amplitude after the first and last AP. The ratios of these values were also calculated (parameter X of last

spike divided by that of the 1<sup>st</sup> spike). In addition, the first and last inter-spike intervals (ISI) were measured and their ratio was calculated. In the case of burst firing cells the first and last ISIs of the first burst were measured, but all ISIs (intra- and inter-burst) were used to generate the ISI distribution (see below). To characterize the firing patterns of ETCs, I calculated the mean, maximum, minimum and coefficient of variation (CV) of the ISI distributions. These parameters allow distinctions to be made among qualitatively different firing patterns. For example, a bursting pattern would result in very different minimum and maximum ISI values, and as a consequence a large CV of the ISI distribution. In contrast, a regular firing pattern would be characterized by similar maximum and minimum ISI values, resulting in a small CV of the ISI distribution. Dissimilarities in individual spike shape, spike frequency adaptation and AP amplitude accommodation are also reflected by our measurements. The membrane time constant ( $\tau$ ) and the input resistance ( $R_{in}$ ) of the cells were also measured (Figure 4B) and revealed tremendous heterogeneities:  $\tau$  ranging from 5.7 to 63.7 ms with a CV of 0.71 and  $R_{in}$  spanning from 43 to 990 M $\Omega$  with a CV of 0.6. I also characterized the cells with respect to their intrinsic, subthreshold resonant properties (Figure 4 and Materials and Methods). In one-fourth of the cells, no active resonance was found at the frequencies tested, whereas in the rest of the cells, the peak resonant frequency varied from 1 to 10 Hz (Figure 8).

Next, I selected those measured and calculated parameters that did not show any dependence on two important experimental variables, and therefore reliably characterized the cells. In order to ensure that the elapsed time from the establishment of the whole-cell configuration did not affect my parameters, I re-measured them at the end of the whole-cell recording period. All parameters were statistically compared between the beginning (first  $3.5 \pm 1.2$  minutes) and at the end ( $10 \pm 3$  minutes later) of the recording periods, and parameters showing significant difference were discarded from my analysis (Table 1). I also tested whether the measured and calculated parameters depended on the amount of injected current to evoke the spike trains. If regression analysis yielded a significant correlation between a parameter and the amount of current injected, the parameter was also discarded. Following these selection criteria, twelve physiological parameters remained and were used for quantitative characterization of ETCs (Table 1).

**Table 1. Selection of functional parameters.** Pearson’s regression analysis was used to ensure that the parameters used to characterize the cells do not depend on the amplitude of the injected current. To ensure that the parameters are not influenced by the elapsed time during the whole-cell recordings, they were compared at the beginning and at the end of the recording period with either parametric (paired t-test, indicated by italics) or nonparametric (Sign-test) tests as appropriate (following Shapiro-Wilk’s normality test, at  $p < 0.01$ ). Parameters independent of both the amplitude of injected current and the elapsed time are highlighted in bold.

<b>Functional parameters</b>	<b>Regression analysis of injected current independence</b>	<b>Paired comparison between beginning and end of recording</b>	
	<b>Pearson's R Correlation</b> <b>p=</b>	<b>Sign test</b>	<b>Paired t-test</b> <b>p=</b>
<b>Input resistance</b>			<b>0.405</b>
<b>Membrane time constant</b>			<b>0.868</b>
<b>Threshold of 1st AP</b>	<b>0.584</b>		<b>0.220</b>
Peak amplitude of 1st AP	<b>0.579</b>		<i>0.000</i>
Full width at half maximum of 1st AP	<b>0.259</b>		0.006
<b>Amplitude of AHP of 1st AP</b>	<b>0.136</b>		<b>0.560</b>
Decay time at 25 % of AHP amplitude	0.007		<b>0.360</b>
Decay time at 50 % of AHP amplitude	0.005		<b>0.542</b>
Decay time at 75 % of AHP amplitude	0.007		<b>0.877</b>
1st ISI	0.004		<b>0.291</b>
<b>Threshold of last AP</b>	<b>0.020</b>		<b>0.880</b>
Peak amplitude of last AP	<b>0.305</b>		<i>0.000</i>
Full width at half maximum of last AP	<b>0.410</b>		<b>0.095</b>
<b>Amplitude of AHP of last AP</b>	<b>0.739</b>		<b>0.263</b>
Decay time at 25 % of AHP amplitude	<b>0.737</b>		<b>0.440</b>
Decay time at 50 % of AHP amplitude	<b>0.475</b>		<b>0.542</b>
Decay time at 75 % of AHP amplitude	<b>0.265</b>		<b>0.222</b>
Last ISI	<b>0.169</b>		<b>0.175</b>
<b>Ratio of last and 1st ISI</b>	<b>0.061</b>		<b>0.651</b>
Ratio of thresholds of last and 1st AP	0.000		<b>0.877</b>
Ratio of peak amplitude of last and 1st AP	0.007		0.000
<b>Ratio of FWHMs of last and 1st AP</b>	<b>0.011</b>		<b>0.519</b>
<b>Ratio of AHP Amplitude of last and 1st AP</b>	<b>0.093</b>		<b>0.014</b>
<b>Mean of ISI distribution</b>	<b>0.082</b>		<b>0.880</b>
<b>Maximum of ISI distribution</b>	<b>0.203</b>		<b>0.880</b>
Minimum of ISI distribution	0.009		<b>0.291</b>
<b>Coefficient of variance of ISI distribution</b>	<b>0.524</b>		<b>0.880</b>

### VI.1.2. The presence of two subpopulations of external tufted cells based on their physiological properties

To determine whether ETCs form multiple subpopulations based on their active and passive electrical properties or whether a single heterogeneous population exists, I performed principal component and cluster analysis (Figure 6). Because the number of available cells (62 cells in total) is likely to be insufficient for clustering in a 12-dimensional space, principal component analysis (PCA) of the parameters was first carried out. As shown in the scree plot in figure 6A, the first 4 factors had Eigenvalues of  $>1$  and accounted for  $>75\%$  of the total variance; therefore they were selected for subsequent cluster analysis. Agglomerative clustering revealed a joining tree with two dominant and several additional sub-branches (Figure 6C).

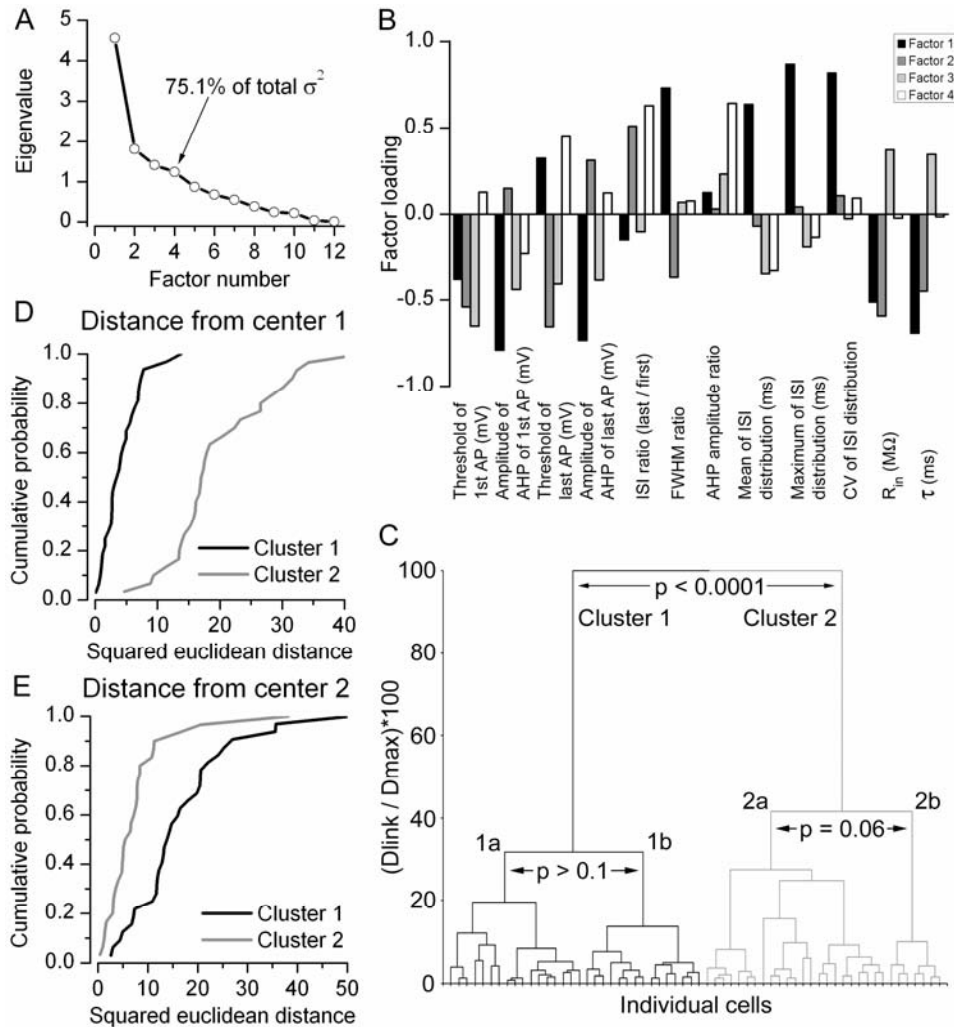


**Figure 6. Principal component and cluster analysis of the recorded cells based on their electrophysiological parameters.** A. Scree plot of the Eigenvalues derived from principal component analysis of 12 physiological parameters. The first 4 factors had Eigenvalues of  $>1$  and together accounted for 75.1% of the total variance. B. Factor loading plot showing the contribution of the 12 physiological parameters to each of the first 4 factors. C. Joining tree of agglomerative clustering using the first 4 principal component factor scores for each cell. Individual cells are illustrated in the X axis and the Y axis shows the percentage of the maximum Euclidean distance between any two cells. Cluster 1 and 2 significantly differ from each other. D. Cumulative probability plots of squared Euclidean distances of each cell in cluster 1 (black) and 2 (gray) from the center of cluster 1. The distributions are statistically different ( $p < 0.001$ , Mann-Whitney test). E. Similar plot as in panel D, but distances of cells in clusters 1 and 2 are shown from the center of cluster 2. The distributions are statistically significant ( $p < 0.001$ , Mann-Whitney test).  $\sigma^2$ : variance, AP: action potential, AHP: spike after-hyperpolarization, ISI: inter-spike interval, FWHM: full width at half maximum amplitude of AP, CV: coefficient of variation,  $R_{in}$ : input resistance,  $\tau$ : membrane time constant. Dlink: linkage distance, Dmax: maximum linkage distance.

Next, I developed a method of objective determination of the number of distinct subpopulations following such clustering (see Materials and Methods). I considered two clusters significantly different in an n-dimensional space if the distance of the members of cluster 1 from the center of cluster 1 was significantly smaller than the distance of the members of cluster 2 from the center of cluster 1, and vice versa. By performing this analysis on ETCs based on the first 4 factors obtained with PCA, I found that two clusters differed significantly (Figure 6D and E), but additional subdivisions (into 3, 4 ... clusters) were not supported statistically.

So far, these results demonstrate the presence of two subpopulations of ETCs based on PCA factors calculated from parameters describing the intrinsic electrical properties of the cells. Next, I asked how different the individual active and passive electrical properties between the two subpopulations were. Statistical comparisons revealed that *i*: the threshold of the first AP (cluster 1:  $-36.1 \pm 3.7$  mV vs. cluster 2:  $-33.3 \pm 4.9$  mV; Figure 7B); *ii-iii*: the amplitude of the AHP after the first ( $4.5 \pm 4.0$  mV vs.  $13.3 \pm 4.6$  mV; Figure 7A) and last ( $7.2 \pm 3.8$  mV vs.  $14.3 \pm 3.7$  mV) APs; *iv*: the ratio of the last and first spike width ( $1.5 \pm 0.4$  vs.  $1.1 \pm 0.1$ ); *v-vii*: the mean ( $77.6 \pm 35.2$  ms vs.  $39.8 \pm 18.7$  ms), maximum ( $319.6 \pm 140.3$  ms vs.  $104.1 \pm 71.4$  ms) and CV ( $1.6 \pm 0.5$  vs.  $0.6 \pm 0.5$ ; Figure 7D) of the ISI distributions; and *viii*: the membrane time constants ( $13.6 \pm 6.5$  ms vs.  $27.8 \pm 17.2$  ms; Figure 7C) are significantly different between the two subpopulations. Qualitatively, the most prominent difference between the two subpopulations was that all members of cluster 1 fired bursts of APs, whereas those of cluster 2 had regular or irregular firing patterns (Figure 5) and did not change to burst firing when hyperpolarized to -60 mV or more negative membrane potentials. However, it is important to note that members of each subpopulation displayed large variability based on several parameters. For example, cells in cluster 1 showed large variability in the degree of the spike amplitude accommodation (Figure 5A) or the amplitude of the AHP (Figure 5A and 7A). Cells belonging to cluster 2 displayed very different spike frequency adaptations (Figure 5B, 7D), amplitude and time course of AHP (Figure 5B, 7A) or  $\tau$  (Figure 7C).

The peak resonance of the cells was also significantly different; cells in cluster 1 displayed a higher peak resonant frequency (Figure 8;  $2.5 \pm 2.2$  Hz vs.  $0.9 \pm 0.8$  Hz).

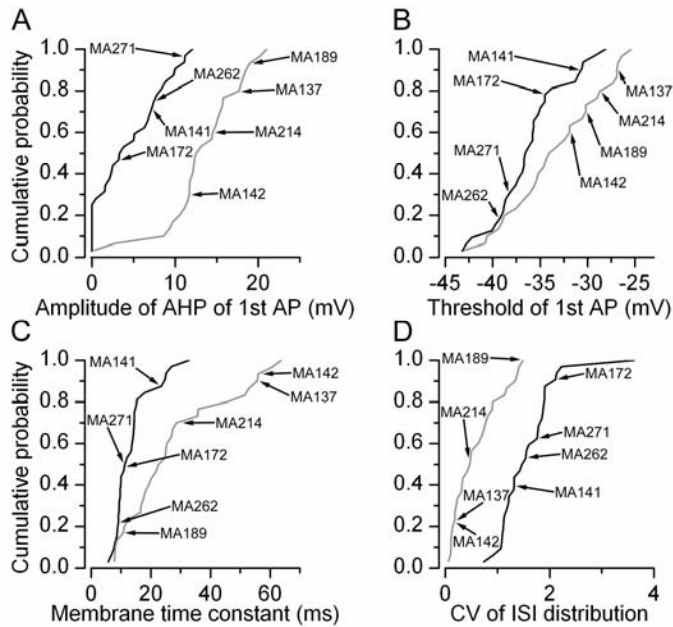


**Figure 7. Between- and within-cluster variability of physiological parameters.**

A-D. Cumulative probability plots of 4 parameters (cluster 1: black; cluster 2: gray), showing significant difference between the two external tufted cell subpopulations. Each parameter varied considerably within each cluster (CVs ranging from 0.34 to 0.88), resulting in some overlap between the subpopulations. The positions of the cells illustrated in figure 5 are marked in each panel.

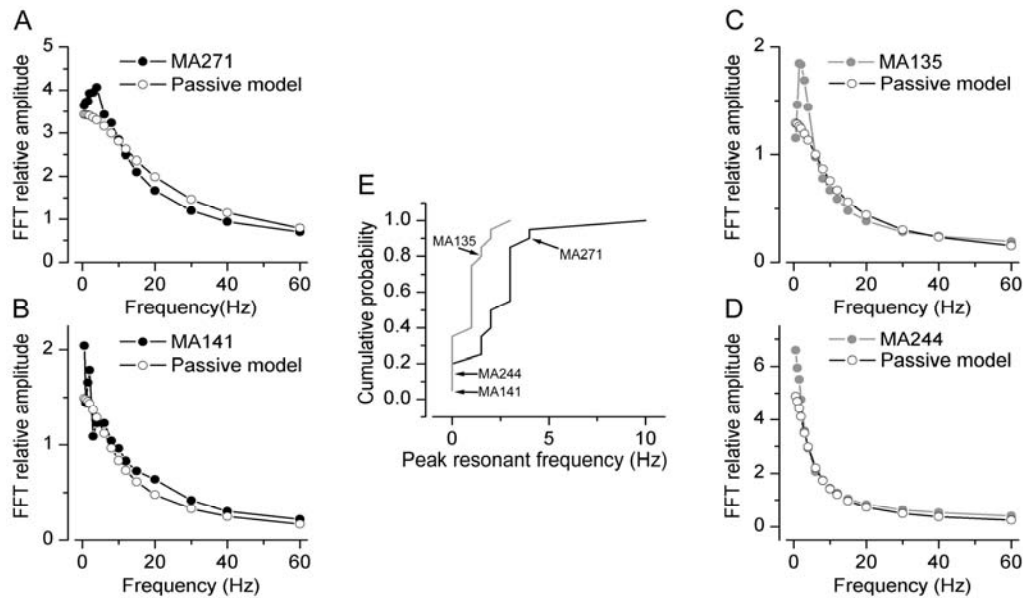


**Figure 8. External tufted cells significantly differ with regard to their subthreshold resonant behavior.**

A-D. Plots of frequency against FFT relative amplitude for four individual cells (black and gray symbols). For comparison, the behavior of passive model cells are shown (open symbols). The peak resonant frequency was determined from these plots. Cells in panel A and B belong to cluster 1 and those in C and D to cluster 2. E. Cumulative probability plot of peak resonant frequencies for cells in cluster 1 (black) and cluster 2 (gray). The two subpopulations are significantly different ( $p < 0.002$ , Mann-Whitney U-test). FFT: fast Fourier transformation.

However, as shown in the cumulative probability plot in figure 8E, both subpopulations had cells without detectable subthreshold resonance, but cells that showed active subthreshold resonance had a higher peak frequency in cluster 1.

### **VI.1.3. Quantitative characterization of external tufted cells based on their dendritic arborizations**

Following the recordings, biocytin was visualized and the cells were analyzed at the light microscopic level and were judged for completeness. All morphological analysis was performed by Dr. Mark D Eyre Ph.D. Cells with incomplete filling or with truncations in their dendritic tree were discarded from our quantitative morphological analysis. However, if a cell showed signs of obvious truncation (e.g. secondary dendrites), but could be still positively identified as an ETC (e.g. from the soma and apical tuft), it remained in our study for physiological analysis only. The most noticeable difference between ETCs was the presence of secondary, basal dendrites in approximately one third of the cells (14/41 cells, Figure 9).

The branching patterns of the basal dendrites were dissimilar; some cells had a non-extensively branching large diameter basal dendrite, spanning a large distance only in one direction from the soma (Figure 9B bottom panel), whereas in some other cells the basal dendrites extensively branched and symmetrically occupied the external plexiform layer (EPL) below the cell (Figure 9B top and middle panel). Several additional morphological differences were also observed, including the presence of apical dendrites ramifying in two glomeruli, large differences in the extent of arborization of the apical dendritic tufts and in the branching patterns (e.g. funnel shaped with relatively few branches vs. globular shaped with extensive branching). Cells also had very different axonal arborizations; some emitted a large number of collaterals in the glomerular layer and EPL before entering the internal plexiform and granule cell layers, whereas some others crossed through the EPL with little branching. Because we hardly ever found cells without truncation in their axonal arbors, the quantitative characterization of the ETCs was based exclusively on their dendritic morphologies. Forty-one cells with complete filling and no obvious dendritic truncations were reconstructed using the NeuroLucida system.

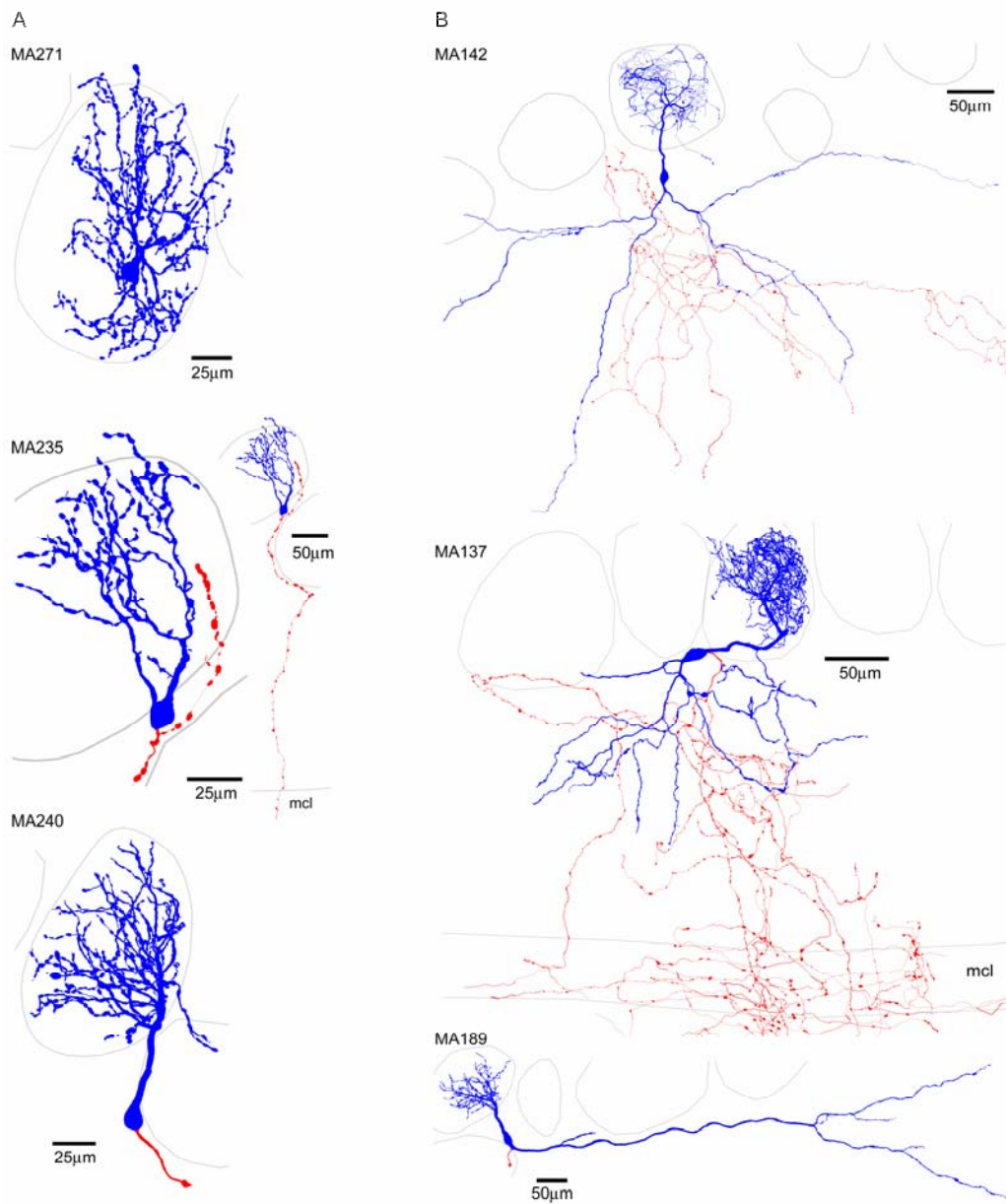


**Figure 9. External tufted cells possess distinct dendritic arborization patterns.** Two-dimensional projections of 3-D reconstructed ETCs with somata and dendrites indicated by blue and the axon is by red. The most pronounced difference between the cells in cluster 1 (A) and 2 (B) is the absence of basal dendrites in the EPL of the cells in cluster 1. Cells within each subpopulation show large diversity based on the total length, number of segments and arborization pattern of their apical tufts. The basal dendrites of ETCs in cluster 2 can also be remarkably different. MA137 and MA142 possessed extensive axonal arbors of in the EPL, MCL, IPL and GCL. MA235 also projects out through the EPL and MCL. The physiological properties of some of these cells are illustrated in Figures 5-8. mcl: mitral cell layer

To quantitatively describe differences in the dendritic arborizations among ETCs, we measured and calculated 9 parameters for the apical as well as the basal dendrites (Figure 10B). For example, dendritic tufts with extensive branching could be easily discriminated from fan-shaped tufts by calculating the number of segments and the total dendritic length. Cells with similar total dendritic length, but very different density of branches can be distinguished by the furthest sholl intercept and from the mean segment tortuosity. I am confident that these measured parameters are sufficient to discriminate between qualitatively dissimilar dendritic patterns and provide comparable values for visually similar dendritic arbors. To reduce the number of dimensions within which clustering was carried out, we performed PCA of the 18 anatomical parameters. The scree plot in figure 10A indicates that 4 factors had Eigenvalues of  $>1$ , accounting for  $>73\%$  of the total variance. Agglomerative clustering using the first 4 PCA factor scores for each cell revealed two main branches on the joining tree with several additional sub-branches (Figure 10C). Similar statistical analysis to that performed above indicated the presence of two subpopulations of ETCs based on their dendritic arborization patterns (Figure 10C-E). To determine the morphological parameters that are significantly different between the two ETC subpopulations, we performed a between-groups statistical comparison for each variable. Fifteen out of the 18 variables differed significantly ( $p < 0.05$ ) between the groups (Table 2).

These results demonstrate that most of the measured morphological parameters are significantly different between the two ETC subpopulations. However, similarly to the physiological parameters, large within-group variability was observed for most measurements (Figure 11), indicating that ETCs within each subpopulation are highly heterogeneous.

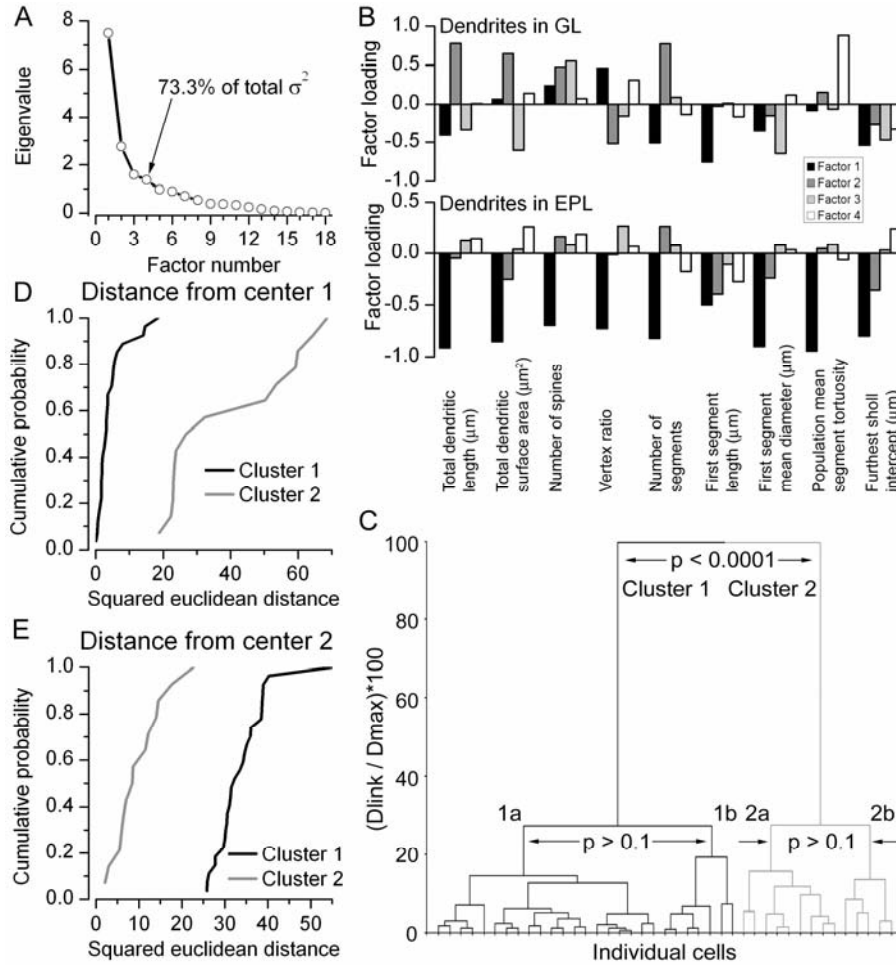


**Figure 10. Principal component and cluster analysis of the recorded cells based on their morphological properties.** A. Scree plot of the Eigenvalues derived from principal component analysis of the 18 morphological parameters. The first 4 factors had Eigenvalues  $>1$ , and together account for 73.3% of the total variance. B. Factor loading plots demonstrate the contribution of the 18 variables, 9 for dendrites in the GL and 9 for dendrites in the EPL, to each of the 4 factors. C. Joining tree of agglomerative clustering using the first 4 principal component factor scores for each cell. Individual cells are shown in the X axis. Cluster 1 and 2 are significantly different from each other. However, further subdivision of the clusters is not justified (neither clusters 1a and 1b nor cluster 2a and 2b are significantly different). D. Cumulative probability plot of squared Euclidean distances of cells in cluster 1 (black) and 2 (gray) from the center of cluster 1. E. Cumulative probability plot of squared Euclidean distances of cells in cluster 1 (black) and 2 (gray) from the center of cluster 2.  $\sigma^2$ : variance; GL: glomerular layer; EPL: external plexiform layer; vertex ratio: a measure of the branching pattern of the dendrites; tortuosity: ratio of the length along a dendritic segment and the shortest distance in 3D between the two ends of the segment; furthest sholl intercept: radius of the largest virtual sphere centered on the soma that is still intercepted by the dendrite. Dlink: linkage distance, Dmax: maximum linkage distance.

**Table 2. Parameters describing the dendritic arborization pattern of external tufted cells.** Significant differences (Mann-Whitney or t-test at  $p < 0.05$ ) are indicated in bold. Cluster 1 contains 27 and cluster 2 14 ETCs. Vertex ratio: a measure of the branching pattern of the dendrites; tortuosity: ratio of the length along a dendritic segment and the shortest distance in 3D between the two ends of the segment; furthest sholl intercept: radius of the largest virtual sphere centered on the soma that is still intercepted by the dendrite.

Morphological parameters	Cluster 1				Cluster 2			
	Mean	SD	Max	Min	Mean	SD	Max	Min
<b>Dendrites in the GL</b>								
Total length ( $\mu\text{m}$ )	<b>2719</b>	876	4613	1337	<b>3512</b>	1180	5834	2029
Total surface area ( $\mu\text{m}^2$ )	10385	4085	21973	5201	9054	2571	16052	5087
Number of spines	<b>55</b>	60	242	4	<b>26</b>	24	76	2
Vertex ratio	<b>0.922</b>	0.236	1.425	0.377	<b>0.718</b>	0.143	0.938	0.513
Number of segments	<b>206</b>	98	535	74	<b>353</b>	197	684	160
First segment length ( $\mu\text{m}$ )	<b>25</b>	20	75	2	<b>79</b>	48	160	11
First segment mean diameter ( $\mu\text{m}$ )	3.09	1.00	6.50	1.30	3.68	1.03	5.40	2.25
Population mean segment tortuosity	1.57	0.32	2.45	1.27	1.58	0.39	2.70	1.31
Furthest Sholl intercept ( $\mu\text{m}$ )	<b>139</b>	29	210	90	<b>172</b>	33	240	130
<b>Dendrites in the EPL</b>								
Total length ( $\mu\text{m}$ )	<b>0</b>	0	0	0	<b>1211</b>	736	2335	242
Total surface area ( $\mu\text{m}^2$ )	<b>0</b>	0	0	0	<b>4727</b>	3562	12341	726
Number of spines	<b>0</b>	0	0	0	<b>8</b>	9	35	0
Vertex ratio	<b>0</b>	0	0	0	<b>0.92</b>	0.73	2.00	0.00
Number of segments	<b>0</b>	0	0	0	<b>23</b>	15	46	4
First segment length ( $\mu\text{m}$ )	<b>0</b>	0	0	0	<b>89</b>	102	292	1
First segment mean diameter ( $\mu\text{m}$ )	<b>0</b>	0	0	0	<b>2.50</b>	1.02	4.00	1.00
Population mean segment tortuosity	<b>0</b>	0	0	0	<b>1.41</b>	0.33	2.02	1.09
Furthest Sholl intercept ( $\mu\text{m}$ )	<b>0</b>	0	0	0	<b>362</b>	226	860	130

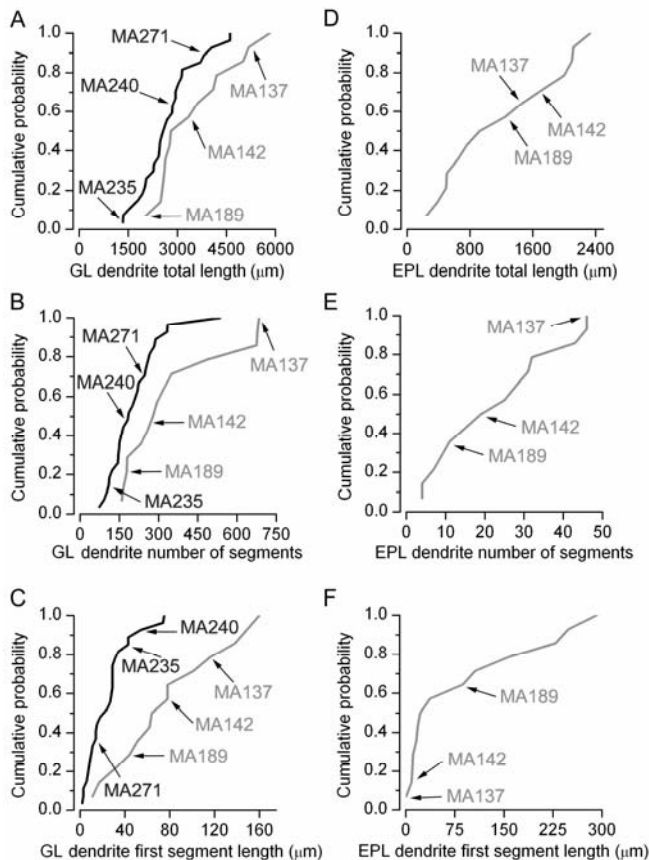


**Figure 11. Quantitative comparisons of the morphological parameters between and within external tufted cell subpopulations.** Fifteen out of 18 parameters significantly differed between cluster 1 (black) and 2 (gray). Some of these parameters include the total dendritic length in GL (A) and EPL (D), the number of dendritic segments in GL (B) and EPL (E) and the first segment length in GL (C) and EPL (F). Each parameter varied considerably within each subpopulation (CVs ranging from 0.32 to 1.15). Cumulative probability distributions of EPL dendrites of cells in cluster 1 are not shown (D-F) because they lacked such dendrites. GL and EPL: glomerular and external plexiform layer, respectively; CV: coefficient of variation.

#### **VI.1.4. Comparing physiologically and morphologically determined external tufted cell subpopulations**

Finally, I asked how the two morphologically determined ETC subpopulations correspond to those derived from the physiological properties. To address this question, I restricted my analysis to a total of 37 ETCs in which all 30 (12 physiological and 18 morphological) parameters were determined (Figure 12).

Principal component analysis indicated 7 factors with Eigenvalues of  $>1$  (Figure 12A), accounting for 78.5% of the total variance. Agglomerative clustering showed a joining tree with two major branches. The presence of two subpopulations was statistically confirmed (Figure 12C and D). When the position of each individual cell was compared, a perfect match was found between the anatomically determined groups and the groups based on all parameters (Figure 12B). This could be the consequence of a large dominance of the anatomical parameters in the first 7 factors derived from PCA. However, a very close agreement between the results of clustering based on all parameters and only the physiological parameters was also observed. Only one cell (MA136) was clustered into the first group based on its physiological properties, which was clustered to the second group when all parameters were taken into account. The rest of the cells ( $n=20$  cells) in the first cluster based on the electrophysiological properties alone were also in the first cluster based on all parameters.

Our results demonstrate that a number of electrophysiological (e.g. burst firing) and morphological (e.g. lack of basal dendrites) parameters of ETCs are highly predictive of one another.

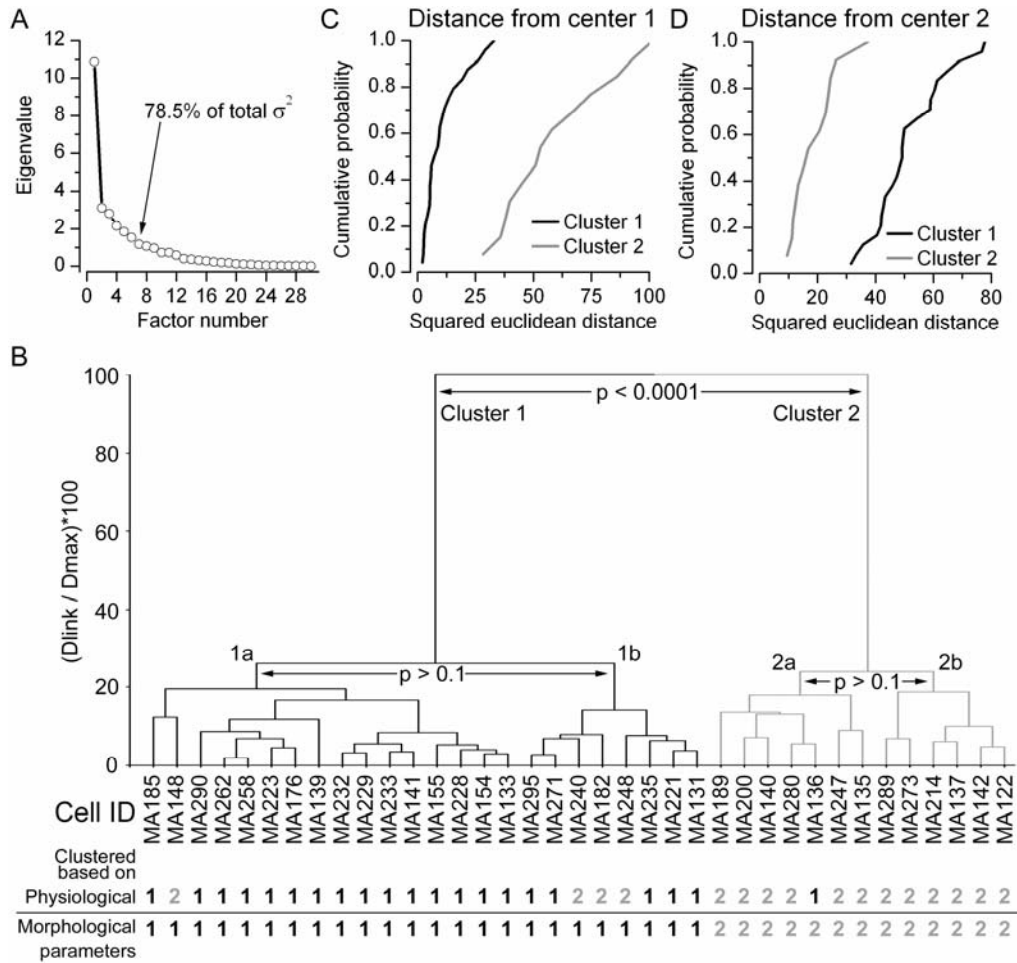


**Figure 12. Principal component and cluster analysis of the recorded cells based on both electrophysiological and morphological properties.** A. Scree plot of the Eigenvalues derived from principal component analysis of the 30 variables (12 functional and 18 structural). The first 7 factors together accounted for 78.5% of the total variance. B. Joining tree of agglomerative clustering using the first 7 principal component factor scores for each cell (37 cells in total for which all 30 parameters were determined). The ID of individual cells is shown on the X axis, whereas the normalized maximum Euclidean distances between any two cells are shown on the Y axis. At the bottom, the group membership of each cell is shown based on clustering of either only the electrophysiological or only the morphological parameters. Note the almost perfect matching between the three ways of clustering. C. Cumulative probability plot of squared Euclidean distances of cells in cluster 1 (black) and 2 (gray) from the center of cluster 1. D. Cumulative probability plot of squared Euclidean distances of cells in cluster 1 (black) and 2 (gray) from the center of cluster 2. The distributions on both panel C and D are significantly different from each other (Mann-Whitney,  $p < 0.001$ ).  $\sigma^2$ : variance, Dlink: linkage distance, Dmax: maximum linkage distance.

#### **VI.1.5. Summary of the results and conclusions**

My results demonstrate the presence of two subpopulations of ETCs of the rat main olfactory bulb based on their active and passive intrinsic electrical properties and their dendritic morphologies. Although 24 out of the 30 measured parameters significantly differed between the two ETC subpopulations, qualitatively the most prominent differences between them were the:

1. presence and absence of basal dendrites and the
2. lack and presence of action potential bursting, respectively.

Although our quantitative analysis indicated the existence of only two ETC subpopulations, a large heterogeneity in both physiological and morphological properties within each subpopulation was apparent.

## **VI.2. Novel intra- and extrabulbar GABAergic connections in the main olfactory bulb are provided by distinct subtypes of deep short-axon cells.**

### **VI.2.1. The morphological diversity of deep short-axon cells**

I carried out patch pipette recordings from the somata of 158 neurons located below the mitral cell layer (MCL) in acute main olfactory bulb slices obtained from P20-P41 rats. Cells with a somatic diameter of  $>10\ \mu\text{m}$  were randomly selected in the internal plexiform (IPL) and granule cell (GCL) layers and were recorded first in cell-attached, and then in whole-cell configurations. Following electrophysiological recordings, the slices were fixed and the biocytin-filled cells were subjected to neurochemical and morphological characterizations.

All of the recorded cells exhibited dendritic and axonal morphologies distinct from both mitral/tufted and granule cells. The location and shape of the somata and the dendritic arbors of these cells were heterogeneous, and examples of all categories of deep short-axon cells (dSACs) described previously were observed (Blanes, 1898; Cajal, 1911; Price and Powell, 1970a; Schneider and Macrides, 1978). Large spiny Blanes cells (73/158 cells) were the most frequent cell morphology encountered, whereas sparsely spiny large Golgi cells (28/158 cells), medium-sized horizontal cells (42/158 cells) and smaller Cajal cells (15/158 cells) were less common. Due to the advantages offered by intracellular labeling techniques compared to Golgi impregnations, we were able to recover extensive axonal trees of the recorded cells. Many dSACs had a very extensive axonal arbor, ramifying in distinct layers of the main olfactory bulb (Figure 13).

A substantial number of cells projected their axons across the external plexiform layer (EPL) and ramified broadly in the glomerular layer (GL). The majority of these branches encircled many glomeruli, and only a few collaterals were found in the EPL and the granule cell layer (GCL) (Figure 13A, B). Their somata were elongated parallel to the MCL, and were often located in the internal plexiform layer (IPL) (32/51 cells). Their dendrites were either sparsely (30/51 cells) or densely (8/51 cells) spiny and predominantly confined to the IPL, corresponding to horizontal cells. The remaining cells (13/51 cells) had an overall appearance of Golgi cells. In contrast, many other dSACs had axonal ramifications predominantly within the EPL, with some collaterals in the IPL and superficial GCL (Figure 13E, F).

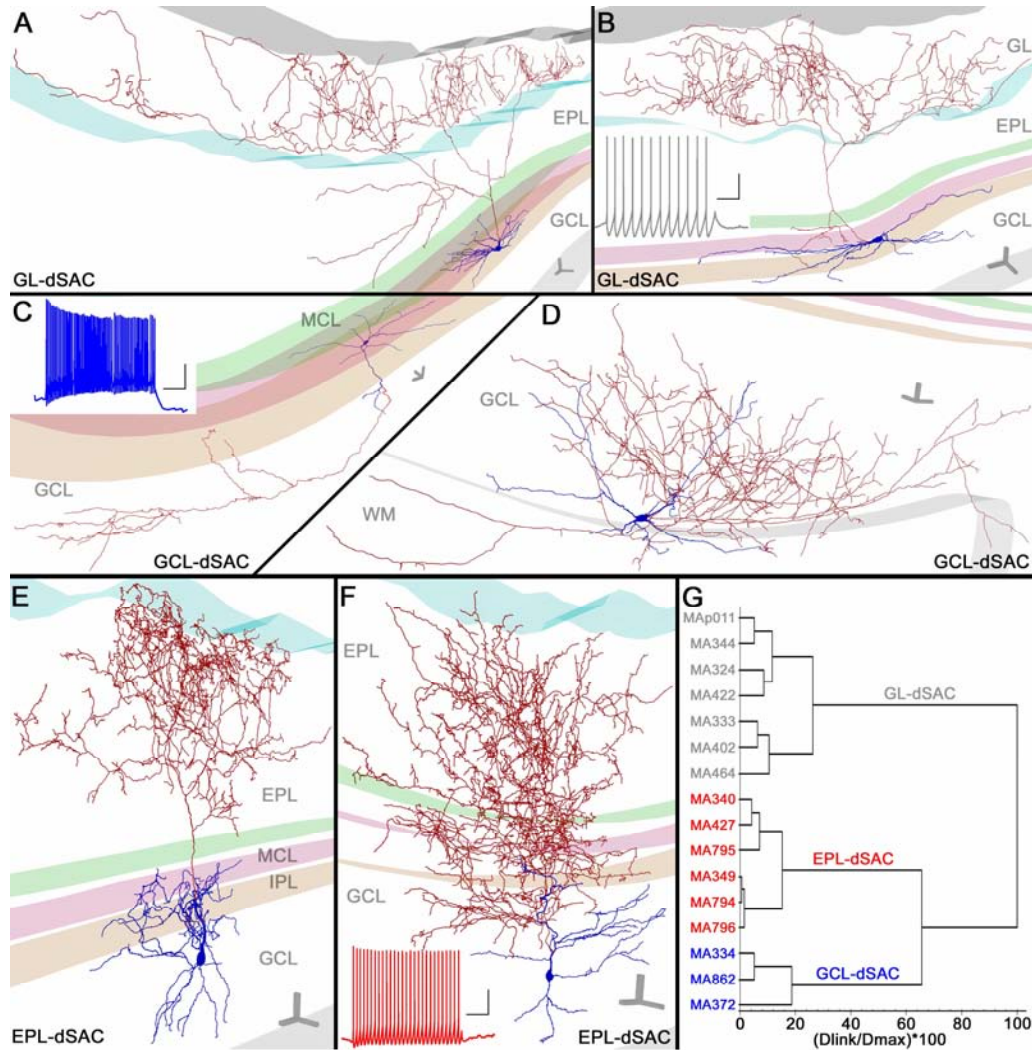


**Figure 13. Three subpopulations of deep short-axon cells based on their axonal and dendritic arborizations.** Three-dimensional Neurolucida reconstructions of individual deep short-axon cells (dSACs). A, B. Some dSACs (A: MA324; B: MA344) have axonal ramifications predominantly in the glomerular layer (GL-dSACs). The cells possess a variable extent of lateral axonal ramification. The dendrites of these cells are mainly confined to the internal plexiform layer (IPL). Inset in B shows voltage responses to one-second long 100 pA depolarizing somatic current injections. C, D. The axonal arbor of some dSACs is confined to the granule cell layer (GCL-dSAC; C: MA334; D: MA862). The somatic location of GCL-dSACs varies throughout the IPL and granule cell layer (GCL) down to the GCL-white matter border. Inset in C demonstrates the firing properties of the reconstructed cell. E, F. The largest proportion of dSACs have an axonal arbor predominantly located in the external plexiform layer (EPL-dSAC; E: MA340; F: MA349) with some local collaterals in the IPL and GCL. These cells mainly possess vertically oriented dendritic trees. Inset in F shows the voltage response of the EPL-dSAC to 1 s long depolarizing (100 pA) current injection. All panels: axons, red; dendrites, blue. Color-coded contours represent boundaries between layers: ONL-GL: dark gray; GL-EPL: blue; EPL-MCL: green; MCL-IPL: red;

IPL-GCL: orange; GCL-WM: light gray. Scale bars: 50  $\mu\text{m}$  along each axis. Scale bars for spike trains: 10 mV/200 ms. G. Joining tree of agglomerative clustering using the first 4 principal component factor scores for each cell. Individual cells are illustrated on the y-axis (ID labels are color-coded by identified subtype) and the x-axis shows the percentage of the maximum Euclidean distance between any two cells. The gap statistic method suggested that the smallest number of clusters was 3.

The axonal arbor was dense, column-like and had a characteristic sharp border between the EPL and GL; axons never entered the GL. The majority (72/79 cells) displayed vertically-polarized somata in the GCL and their stellate or vertically oriented dendrites were usually covered with spines (62/79 cells), giving them the appearance of Blanes cells (Figure 13F). However, some cells with similar axonal morphologies possessed smooth dendrites almost devoid of spines, typical of vertical Cajal cells (Figure 13E; 14/79 cells). Finally, the smallest subset of dSACs had axonal arbors restricted to the GCL (Figure 13C, D). In order to exclude the possibility that the lack of axons in the superficial layers was the consequence of truncation during slice preparation, we discarded all such cells from our analysis. The somata of these cells were often located in the GCL (13/28 cells) and their dendrites were usually sparsely spiny (25/28 cells), having an overall appearance of horizontal or Golgi cells.

Thus, our analysis of the somato-dendritic morphologies was in agreement with the classical Golgi studies, but when the axonal arborizations were also considered, a more complex picture emerged. In order to assess whether dSACs can be objectively divided into well-defined subpopulations based on both their axonal and dendritic morphologies, we reconstructed a subpopulation of these cells in 3D and subjected them to morphometric measurements. Following principal component analysis, agglomerative clustering (see Materials and Methods) suggested 3 main subpopulations (Figure 13G), which was confirmed using the gap statistic method (Tibshirani et al., 2001). Based on the predominant axonal arborizations of the subpopulations in different layers, they were termed as GL-, EPL- and GCL-dSACs (Figure 13). Our results also demonstrate that many morphological parameters (e.g. dendritic fractal index, axonal segment length, furthest axonal Sholl intercept, Table 3) significantly differed among the subtypes.

**Table 3. Many morphological parameters significantly differ between subtypes of deep short axon cells.** Significant differences are indicated by \* and \*\* for parametric ANOVA or by # and \$ for Kruskal-Wallis nonparametric ANOVA tests at  $p < 0.05$  and  $p < 0.01$  levels, respectively. # and \$ depict significant ( $p < 0.05$ ) differences between the indicated pairs following *post hoc* tests. Vertex ratio: a measure of the branching pattern of the dendrites; furthest Sholl intercept: radius of the largest virtual sphere centered on the soma that is still intercepted by the dendrite or the axon; fractal index: a measure of the space-filling nature of the object.

Morphological parameters	GL-dSAC Mean $\pm$ SD	EPL-dSAC Mean $\pm$ SD	GCL-dSAC Mean $\pm$ SD	ANOVA
Soma minor diameter ( $\mu\text{m}$ )	14.0 $\pm$ 2.5 # \$	11.4 $\pm$ 2.3 #	10.2 $\pm$ 2.4 \$	**
Dendrite fractal index	1.09 $\pm$ 0.05 #	1.09 $\pm$ 0.04	1.05 $\pm$ 0.03 #	*
Axon mean segment length ( $\mu\text{m}$ )	39.0 $\pm$ 8.8 #	13.6 $\pm$ 4.6 # \$	34.8 $\pm$ 14.5 \$	**
Furthest axon Sholl intercept ( $\mu\text{m}$ )	976 $\pm$ 486 #	458 $\pm$ 73 # \$	995 $\pm$ 325 \$	**
Axon fractal index	1.21 $\pm$ 0.10	1.32 $\pm$ 0.10	1.16 $\pm$ 0.16	*
Mean % of dendrite in IPL	68.9 $\pm$ 15.0 # \$	20.2 $\pm$ 11.2 #	19.6 $\pm$ 23.9 \$	**
Mean % of dendrite in GCL	26.4 $\pm$ 16.4 #	76.6 $\pm$ 13.1 #	57.4 $\pm$ 38.2	**
Mean % of axon in GL	52.9 $\pm$ 29.9 # \$	0 #	0 \$	**
Mean % of axon in EPL	13.2 $\pm$ 8.8	57.0 $\pm$ 22.7 #	0 #	**
Mean % of axon in MCL	7.3 $\pm$ 6.2	18.2 $\pm$ 9.5 #	1.3 $\pm$ 2.6 #	*
Mean % of axon in GCL	14.5 $\pm$ 12.1	7.8 $\pm$ 5.8 #	92.7 $\pm$ 5.6 #	*

### VI.2.2. Granule cell layer-dSACs project to higher olfactory areas

When the local axon collaterals of distinct dSAC subtypes were analyzed, we noticed that a branch of the main axon of GCL-dSACs often entered the white matter and projected caudally in the lateral olfactory tract, suggesting that GCL-dSACs might form an extrabulbar projection (Kosaka and Kosaka, 2007). In order to address this issue directly, my colleague, Mark D. Eyre Ph.D. injected fluorescent microspheres into many higher order olfactory areas, including the anterior olfactory nucleus, the olfactory tubercle, the piriform cortex and the deep endopiriform nucleus (Figure 14).

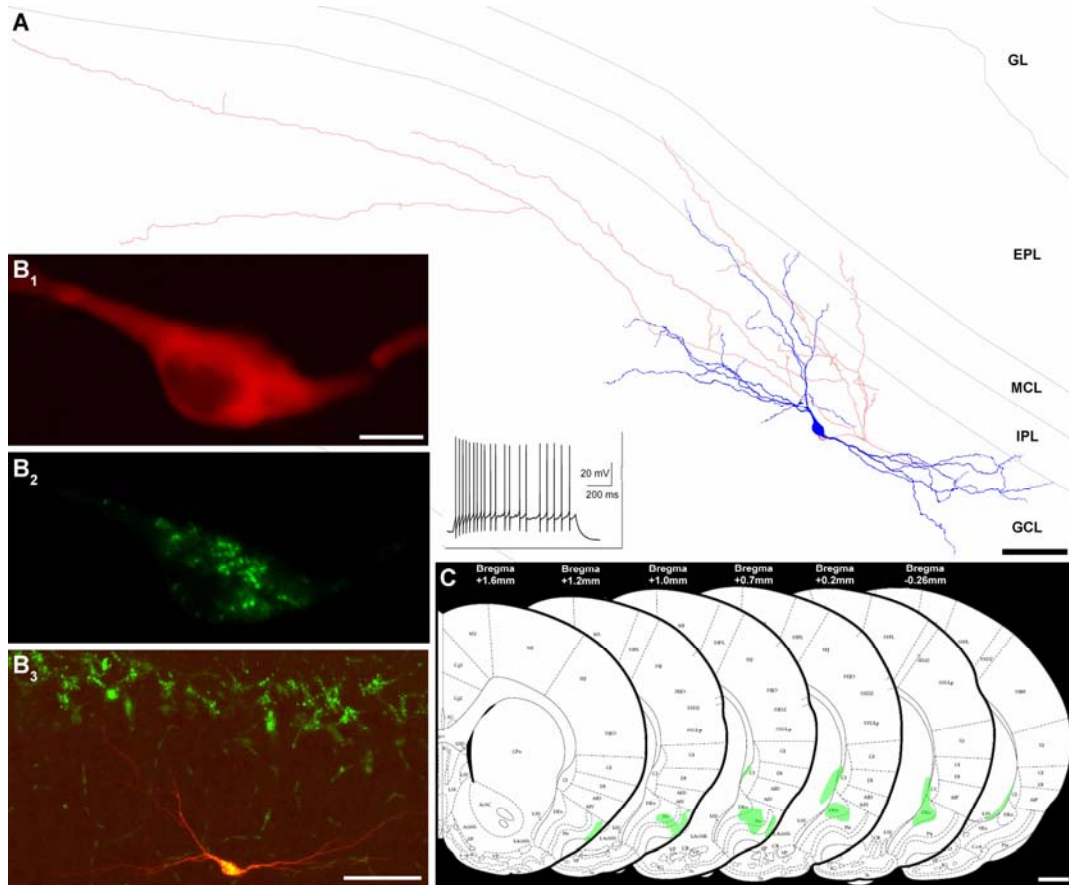


**Figure 14. A granule cell layer-dSAC projecting to the piriform cortex.** A. NeuroLucida reconstruction of a retrogradely labeled GCL-dSAC (MA1034) showing dendrites (blue) and axons (red) confined to the inframitral layers extending considerably in the rostro-caudal axis of the GCL. Scale bar: 200  $\mu$ m. Inset illustrates the voltage response of the cell to a one-second long 100 pA depolarizing current injection. B. *Post hoc* visualization of the intracellularly applied biocytin (red) confirmed that the recorded cell contained fluorescent microspheres (green). Note that many mitral cells also contained fluorescent microspheres (green cells in B<sub>3</sub>). Scale bars: B<sub>1</sub> and B<sub>2</sub>: 10  $\mu$ m, B<sub>3</sub>: 50  $\mu$ m. C. The site of the injection of fluorescent microspheres (green overlay) is shown superimposed on coronal maps (from Paxinos and Watson, 1998) at six rostro-caudal levels relative to Bregma. The injection is mainly confined to the piriform cortex and the deep endopiriform nucleus. Scale bar: 1 mm. GL, EPL, MCL, IPL, GCL: glomerular, external plexiform, mitral cell, internal plexiform, granule cell layer, respectively

Three to 14 days after surgery, I prepared acute *in vitro* slices from the main olfactory bulb and fluorescently labeled cells with inframitral somatic locations were subject of whole cell recordings. Following the characterization of their active and passive electrical properties and their synaptic inputs (see below), the presence of microspheres in the biocytin-filled cells was verified (Figure 14B) followed by full morphological

reconstructions. Figure 14A shows the reconstruction of a dSAC with projection to the piriform cortex and the deep endopiriform nucleus. The soma was located in the GCL, had horizontally oriented dendrites, and the local axon collaterals were also restricted to the inframitral layers. Qualitatively very similar axonal and dendritic arborizations were found in all 17 cells in which sufficient axons and dendrites were recovered following *in vitro* electrophysiological characterization (n=42 cells). The axo-dendritic morphologies of these retrogradely labeled cells were indistinguishable from the randomly recorded and filled GCL-dSACs, but it remains to be seen whether all GCL-dSACs project outside the main olfactory bulb.

### **VI.2.3. Molecular differences between deep short-axon cells**

We then addressed whether molecular differences also exist among dSAC subtypes. Previous immunolabeling studies have indicated that neuropeptide Y (NPY), vasoactive intestinal polypeptide (VIP), calbindin (CB) and nitric oxide synthase (NOS) are neurochemical markers for dSACs in the inframitral layers. However, because these markers labeled very few cells (e.g. VIP and CB <4% of all dSACs), we found none of them to be a good candidate as a selective marker of a particular dSAC subtype. In contrast, the GABA<sub>A</sub> receptor (GABA<sub>A</sub>R)  $\alpha$ 1 subunit selectively labels the somato-dendritic domain of a large population of non-granule cells in the inframitral layers of the main olfactory bulb (Figure 15A), making it a potential subtype-selective marker.

As illustrated in figure 15A, only dSACs are immunopositive for this subunit in the GCL; the strong labeling of the EPL originates from mitral/tufted cells. A subset of the *in vitro* recorded cells (n=50 cells) was processed for immunolabeling for the GABA<sub>A</sub>R  $\alpha$ 1 subunit in conjunction with fluorescent visualization of the biocytin. All EPL-dSACs (n=30 cells) were intensely labeled for the  $\alpha$ 1 subunit (Figure 15C). Eleven out of 15 GL-dSACs were found to be moderately labeled (Figure 15B), whereas two were strongly labeled and two appeared to be immunonegative. Finally, the majority (4/5 cells) of GCL-dSACs were apparently immunonegative (Figure 15D); only a single cell showed very weak immunoreactivity.

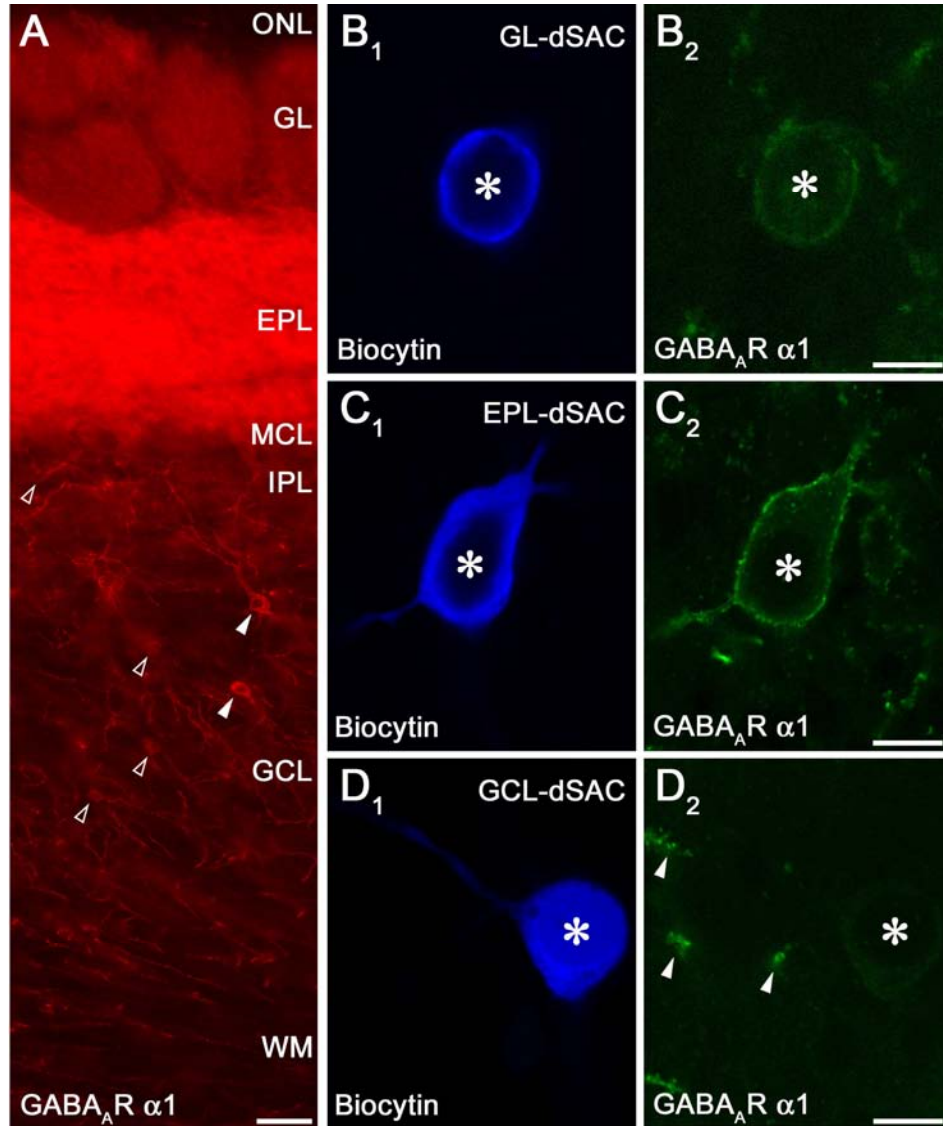


**Figure 15. Deep short-axon cell subtypes differentially express the GABA<sub>A</sub> receptor  $\alpha$ 1 subunit.** A. Immunofluorescent labeling for the GABA<sub>A</sub> receptor  $\alpha$ 1 subunit in the main olfactory bulb. In the IPL and GCL, the  $\alpha$ 1 subunit is exclusively expressed by dSACs. Strongly and weakly-labeled cells are indicated by filled and open arrowheads, respectively. The very strong labeling of the EPL originates from mitral/tufted cell somata and dendrites. Scale bar: 50  $\mu$ m. B-D. Confocal images of intracellularly filled dSACs (biocytin: blue) immunolabeled *post hoc* for the GABA<sub>A</sub> receptor  $\alpha$ 1 subunit (green). Glomerular layer-dSACs (B: MA900) are weakly immunopositive, EPL-dSACs (C: MA916) are strongly immunopositive, whereas the GCL-dSACs (D: MA920) are immunonegative for the GABA<sub>A</sub> receptor  $\alpha$ 1 subunit. Note the extensive dendritic labeling of EPL-dSACs in panel C<sub>2</sub> and the lack of labeling of GCL-dSACs despite adjacent strongly-labeled processes (arrowheads) in D<sub>2</sub>. Scale bars: B-D: 10  $\mu$ m. ONL, GL, EPL, MCL, IPL, GCL: olfactory nerve, glomerular, external plexiform, mitral cell, internal plexiform, granule cell layer, respectively; dSAC: deep short-axon cell.

These results clearly demonstrate that molecular differences exist, but future experiments will be needed to identify other dSAC subtype-selective molecular markers.

#### VI.2.4. Deep short-axon cells show distinct intrinsic electrical properties

Given the morphological and molecular heterogeneity of dSACs, I also aimed to reveal potential subtype-specific differences in the electrophysiological properties of the cells. Cell-attached recordings prior to the establishment of the whole-cell configuration demonstrated differences in the spontaneous spiking activity of dSACs in acute *in vitro* slices. Both GL- and GCL-dSACs were found to be spontaneously active, whereas 27 out of 28 EPL-dSACs were silent (Table 4).

**Table 4. Significant differences in physiological properties of deep short-axon cells.** Significant differences are indicated by \* and \*\* using Kruskal-Wallis nonparametric ANOVA test at  $p < 0.05$  and  $p < 0.01$  levels, respectively. # and \$ indicate a significant ( $p < 0.05$ ) *post hoc* test (multiple comparisons of mean ranks) between the indicated pairs. AP: action potential; AHP: after-hyperpolarization; FWHM: full width at half maximum amplitude; ISI: inter-spike interval

Physiological parameters	GL-dSAC Mean $\pm$ SD	EPL-dSAC Mean $\pm$ SD	GCL-dSAC Mean $\pm$ SD	ANOVA
Spontaneous firing activity (Hz)	7.41 $\pm$ 6.54 <sup>#</sup>	0.25 $\pm$ 1.31 <sup>#</sup>	3.26 $\pm$ 3.29 <sup>\$</sup>	**
Input resistance (M $\Omega$ )	306.2 $\pm$ 150.1 <sup>#</sup>	160.8 $\pm$ 68.6 <sup>#</sup>	406.6 $\pm$ 180.7 <sup>\$</sup>	**
Membrane time constant (ms)	25.4 $\pm$ 8.9 <sup>#</sup>	13.5 $\pm$ 5.7 <sup>#</sup>	32.8 $\pm$ 18.6 <sup>\$</sup>	**
Threshold of first AP (mV)	-38.2 $\pm$ 5.4	-39.8 $\pm$ 5.6 <sup>#</sup>	-35.1 $\pm$ 3.2 <sup>#</sup>	*
Amplitude of AHP of first AP (mV)	14.0 $\pm$ 5.1 <sup>#</sup>	11.2 $\pm$ 3.5 <sup>#</sup>	13.1 $\pm$ 2.2	*
Decay time at 75 % of AHP amplitude of first AP (ms)	21.1 $\pm$ 19.8 <sup>#</sup>	25.5 $\pm$ 6.3 <sup>#</sup>	12.4 $\pm$ 7.5 <sup>\$</sup>	**
Ratio of thresholds of last and first AP	0.86 $\pm$ 0.07 <sup>#</sup>	0.73 $\pm$ 0.47 <sup>#</sup>	0.74 $\pm$ 0.14 <sup>\$</sup>	**
Ratio of FWHMs of last and first AP	1.19 $\pm$ 0.17 <sup>#</sup>	1.26 $\pm$ 0.16 <sup>#</sup>	1.44 $\pm$ 0.72	*
Ratio of AHP Amplitude of last and first AP	1.17 $\pm$ 0.37 <sup>#</sup>	1.32 $\pm$ 0.23 <sup>#</sup>	1.08 $\pm$ 0.12 <sup>\$</sup>	**
Mean of ISI distribution (ms)	36.4 $\pm$ 19.1 <sup>#</sup>	40.1 $\pm$ 8.8 <sup>#</sup>	21.1 $\pm$ 7.8 <sup>\$</sup>	**

In whole-cell recordings, dSACs exhibited a variety of action potential firing patterns in response to one-second long 100pA depolarizing current injections (Figure 13 insets). Quantitative analysis of a large number of parameters derived from the spike trains, individual spikes and the passive electrical properties of the cells revealed significant dSAC subtype-specific differences and prominent within-subtype heterogeneity for many parameters (Table 4).

#### **VI.2.5. Excitatory and inhibitory inputs onto deep short-axon cells**

In order to gain insights into the potential role of a neuron in a network, not only the morphological, molecular and intrinsic electrical properties should be deciphered, but the synaptic connectivity must be determined as well. To investigate the synaptic inputs of dSACs, I performed *in vitro* voltage-clamp recordings of spontaneous excitatory and inhibitory postsynaptic currents before and during the application of 1  $\mu$ M tetrodotoxin (TTX). Potential sources of glutamatergic excitation are either the local mitral/tufted cells or centrifugal inputs from the anterior olfactory nucleus and piriform cortex (Shepherd et al., 2004). I argued that if TTX reduces the frequency of spontaneous excitatory postsynaptic currents (sEPSCs), then the cells providing the excitatory inputs must be present in the slice and should be spontaneously active. Figure 16A shows representative recordings of AMPA receptor-mediated sEPSCs in the presence of GABA<sub>A</sub> and NMDA receptor antagonists for each dSAC subtype.

Tetrodotoxin dramatically reduced the frequency and amplitude of sEPSCs in a GL- and an EPL-dSAC, and less dramatically in a GCL-dSAC (Figure 16A, B). When examined at the population level, a significant decrease in EPSC frequency was detected in all subtypes without any change in the kinetics of the responses (Figure 16C). The amplitude of sEPSCs was significantly reduced in GL- and EPL-, but not in GCL-dSACs. I also noted the prevalence of bursts of sEPSCs in control conditions, which disappeared following TTX application, indicating that the sources of these synaptic currents are likely to be bursting external tufted (Hayar et al., 2004a) or some mitral cells (Carlson et al., 2000). The amplitude, rise and decay kinetics showed no significant differences among the subtypes (Figure 16B, C). The extremely rapid rise of the miniature EPSCs (mEPSCs) (10-90% rise time: 230-300  $\mu$ s) suggests that neither asynchronous release nor dendritic filtering is severe in these cells.

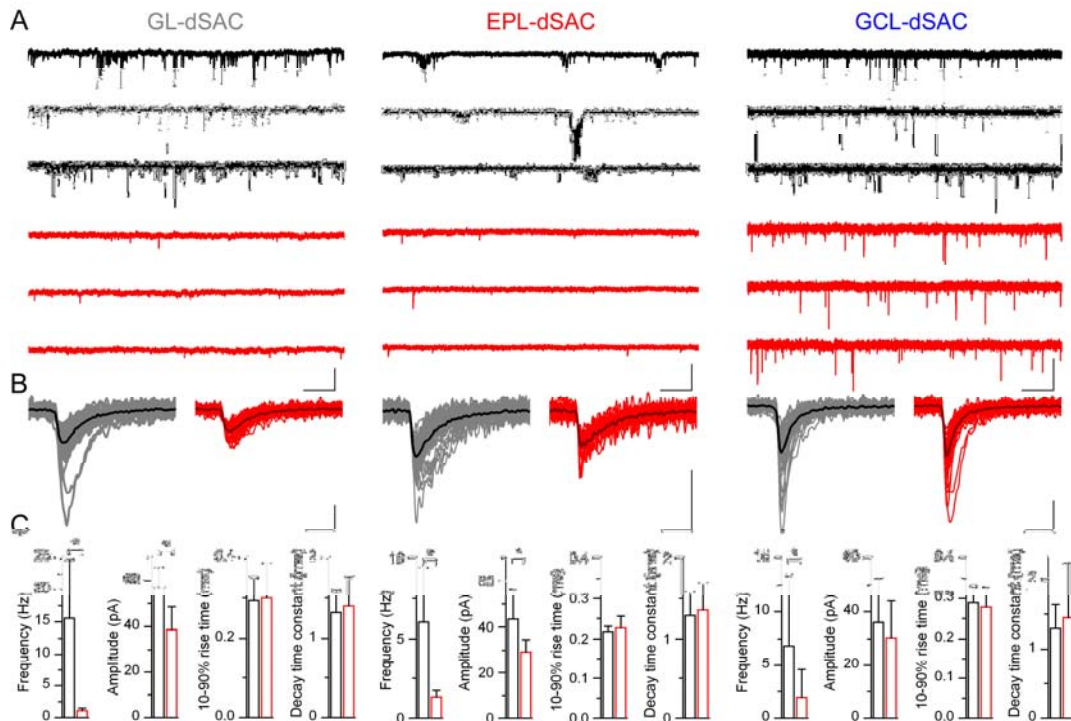


**Figure 16. Tetrodotoxin reduces the amplitude and frequency of sEPSCs in a cell type-specific manner.** A. Representative recordings of spontaneous EPSCs before (black traces) and after (red traces) bath application of 1  $\mu$ M TTX, in the presence of 20  $\mu$ M SR95531 and 50  $\mu$ M D-AP5. Note the large reduction in the frequency and amplitude of EPSCs in GL- (MA934) and EPL- (MA889), and the moderate change in GCL-dSACs (MA915). Scale bars: 100 pA/200 ms. B. Consecutive individual spontaneous (gray traces) and miniature (red traces) EPSCs are shown superimposed on an extended time scale with their corresponding averaged traces (black and dark red, respectively). Scale bars: 50 pA/2 ms. C. Summary plots of the effect of TTX on the frequency, amplitude and kinetics of EPSCs in all dSAC subtypes. For GL- (n=6 cells), EPL- (n=6 cells) and GCL-dSACs (n=12 cells) dSACs, TTX resulted in a significant (Wilcoxon matched paired test, \*:  $p < 0.05$ ) reduction in the frequency without affecting the kinetics of the responses. The amplitude of sEPSCs was significantly reduced in GL- and EPL-, but not in GCL-dSACs. sEPSC: spontaneous excitatory postsynaptic current; TTX: tetrodotoxin; GL, EPL, GCL: glomerular, external plexiform, granule cell layer, respectively; dSAC: deep short axon cell.

In addition, the identical decay time constants (weighted decay time constant ( $\tau_w$ ) = 1.4 ms for all subtypes, Figure 16C) indicate similar postsynaptic AMPA receptors and synaptic glutamate concentration waveforms. In summary, dSACs receive some of their AMPA receptor-mediated excitatory input from spontaneously active mitral/tufted cells. In agreement with this, electron microscopy (EM) analysis revealed that the presynaptic elements establishing asymmetrical synapses on dSACs were axon terminals (data not shown).

Next, I examined the inhibitory inputs of dSAC subtypes by recording spontaneous inhibitory postsynaptic currents (sIPSCs) using high chloride containing intracellular solutions in the presence of the glutamate receptor antagonists, CNQX and D-AP5. The average frequency of sIPSCs ranged from 3.4 to 7.1 Hz under control conditions, which was significantly reduced following the application of TTX in all dSAC subtypes (Figure 17).

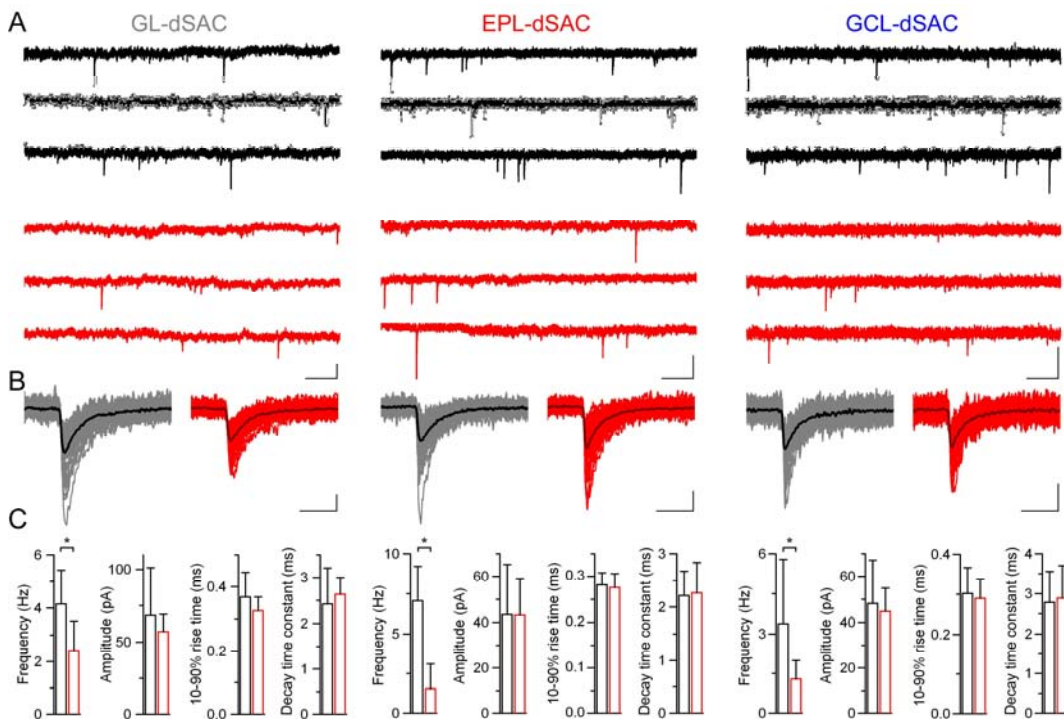


**Figure 17. The effect of blocking the network activity with tetrodotoxin on spontaneous IPSCs.** A. Continuous current recordings before (black traces) and after (red traces) bath application of 1  $\mu$ M TTX, in the presence of 20  $\mu$ M CNQX and 50  $\mu$ M D-AP5, are shown from individual cells of each dSAC subtype (GL-: MA858; EPL-: MA882; GCL-: MA913). Scale bars: 40 pA/200 ms. B. Consecutive individual spontaneous (gray traces, average in black) and miniature (red traces, average in dark red) IPSCs are shown on an extended time scale. Scale bars: 20 pA/5 ms. C. Summary of the effects of 1  $\mu$ M TTX on spontaneous IPSCs in GL (n=6 cells), EPL (n=5) and GCL (n=5) dSACs. For all three subtypes, a significant (Wilcoxon matched paired test, \*: p<0.05) effect was only detected for IPSC frequency. IPSC: inhibitory postsynaptic current; TTX: tetrodotoxin; GL, EPL, GCL: glomerular, external plexiform, granule cell layer, respectively; dSAC: deep short axon cell.

Application of TTX did not change the amplitudes of sIPSCs significantly, suggesting a low quantal content (~1) in all dSACs. Comparisons between dSAC subtypes showed no statistically significant differences in mIPSC amplitudes or kinetics (Figure 17C). The fast rise times of mIPSCs (10-90% rise time: 280-330  $\mu$ s) also indicate the lack of both severe dendritic filtering and robust asynchronous release. The comparable decay time constants ( $\tau_w=2.3, 2.6$  and  $2.9$  ms for EPL-, GL- and GCL-dSAC, respectively) suggest similar postsynaptic GABA<sub>A</sub> receptor subunit compositions and synaptic GABA concentration waveforms. These data demonstrate that all dSAC subtypes receive some of their fast synaptic inhibition from spontaneously active, local GABAergic interneurons. From our current knowledge of the main olfactory bulb microcircuit, these could be either granule cells or short-axon cells. By using EM analysis, we found that the presynaptic elements of symmetrical synapses onto dSACs were exclusively GABA immunoreactive axon terminals. No evidence of dendro-dendritic synapses, either established by or formed onto dSAC subtypes was observed, suggesting that the majority of the GABAergic inputs of dSACs originate from short-axon cells (data not shown).

#### **VI.2.6. The postsynaptic targets of GABAergic deep short-axon cells are other GABAergic interneurons**

Following the identification of the synaptic inputs of dSACs, we carried out EM analysis of the postsynaptic targets of biocytin-filled dSAC axon terminals. In addition to the classification of postsynaptic profiles based on ultrastructural features, their neurotransmitter content was also revealed using postembedding immunogold labeling for GABA. Axon terminals of GL-dSACs ( $n=3$  cells) ramifying in the juxtglomerular space established symmetrical synapses onto small diameter somata (5 synapses), and large (22 synapses) and small (17 synapses) diameter dendrites, which all showed ultrastructural features of periglomerular cells (PGCs) (Figure 18A, B) and were immunopositive for GABA (Figure 18B, 20A). Because PGCs form a very diverse cell population, we asked whether GL-dSAC axons selectively innervate a single subpopulation or indiscriminately synapse on all cell types.

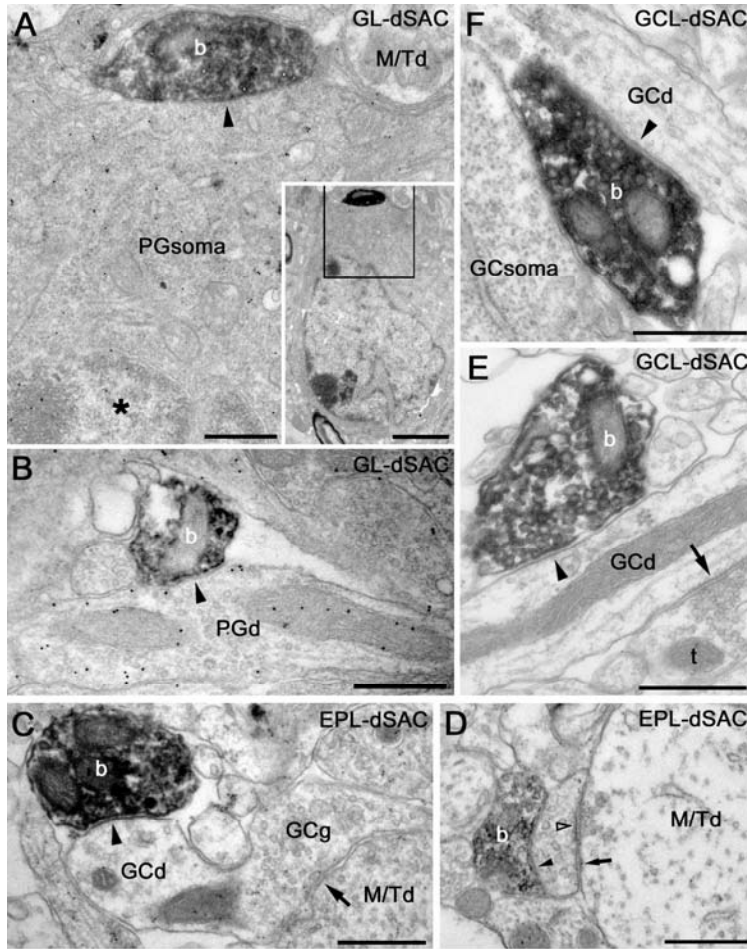


**Figure 18. Deep short-axon cell subtypes selectively innervate other GABAergic interneurons.**

A. Electron micrograph showing an axon terminal (b; black DAB precipitate) of a biocytin-filled GL-dSAC (MA324) forming a symmetrical synapse (arrowhead) onto the soma of a periglomerular neuron (PG soma). The section was immunoreacted for GABA (small gold particles) using the postembedding immunogold method. Inset shows the area at a lower magnification. Note the absence of gold particles in the adjacent principal cell process (M/Td). B. An axon terminal (b) of a GL-

dSAC (MA324) in the GL forms a symmetrical synapse (arrowhead) onto a strongly GABA immunopositive periglomerular cell dendrite (PGd). C. The postsynaptic target of an EPL-dSAC (MA340) in the EPL is a granule cell dendrite (GCd). A gemmule (GCg) emerges from this dendrite and forms a symmetrical synapse (arrow) onto a mitral/tufted dendrite (M/Td). Note the presence of immunogold particles labeling GABA in the vesicle-filled gemmule. D. A bouton (b) of an EPL-dSAC (MA349) in the EPL establishes a symmetrical synapse (arrowhead) onto the gemmule of a granule cell, which forms a reciprocal synapse with a mitral/tufted profile (M/Td; mitral-granule asymmetric synapse, open arrowhead; granule-mitral symmetrical synapse, arrow). E, F. The postsynaptic targets of GCL-dSACs (MA372) in the GCL are granule cell dendrites (GCd). Note that in panel E the granule cell dendrite also receives a symmetrical synapse (arrow) from an unidentified axon terminal (t). All scale bars: 500 nm, except inset of panel A: 2 μm

Using fluorescent immunolabeling for tyrosine hydroxylase and calbindin, and visualizing biocytin in the intracellularly filled axons, we found that at least these two neurochemically defined PGC subpopulations are among the postsynaptic targets of GL-dSACs (Figure 19).

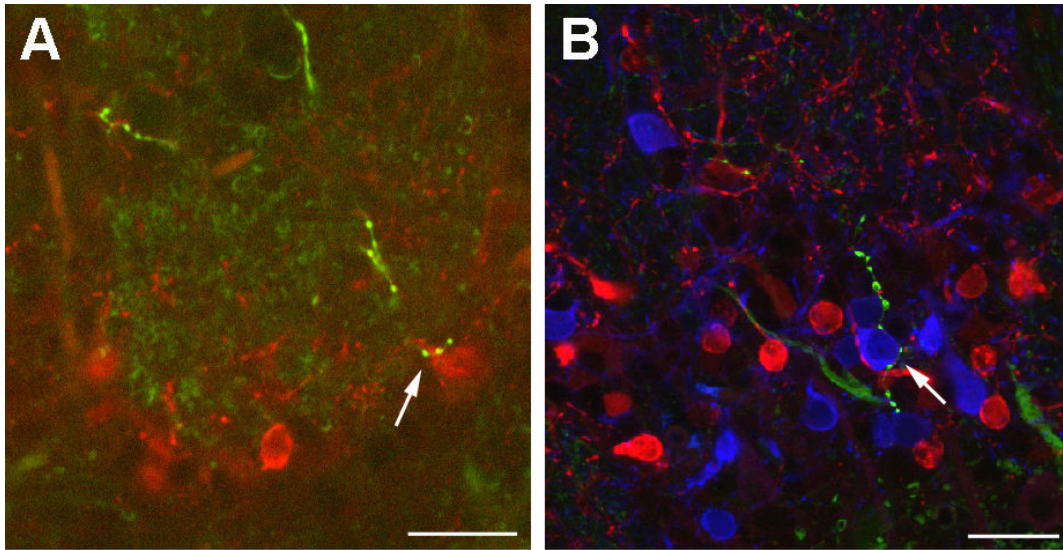


**Figure 19. Neurochemical identification of the postsynaptic targets of GL-dSACs in the glomerular layer.** A. Biocytin-labeled axons of a GL-dSAC (MA847, green) ramify in the GL and form varicosities in close apposition to a calbindin (CB) immunopositive (red) periglomerular cell (arrow). B. Biocytin-labeled axons of a GL-dSAC (MA856, green) partially encircle the soma of a tyrosine hydroxylase (TH) immunopositive (blue) periglomerular cell (arrow), forming three closely apposed varicosities. Note that the TH positive population does not overlap with the CB positive cells (red). Scale bars: 25  $\mu$ m.

In addition, axon collaterals of one GL-dSAC ramifying in the EPL (n=10 synapses) and a different one arborizing in the GCL (n=4 synapses) were found to synapse exclusively on granule cell (GC) dendrites. Next, the postsynaptic targets of EPL-dSAC (n=4 cells) axons were examined in the EPL, where 38 out of 43 synapses were formed onto GC dendritic shafts and the remaining 5 synapses established contacts onto GC gemmules (Figure 18C, D). The ultrastructural identification of these targets was assisted by the presence of reciprocal dendro-dendritic synapses with mitral/tufted cells and their GABA immunoreactivity (Figure 18C, 20B).

In the GCL, 38 axon terminals from 3 EPL-dSACs were also examined and 37 formed synapses onto GC dendrites. The only exception was a synapse onto the perisomatic region of a horizontally elongated soma in the IPL, which was strongly GABA immunopositive and was considered to be a dSAC. Finally, the axons of two GCL-dSACs were examined in the GCL. Out of the 13 synapses analyzed, 11 contacted GC proximal dendrites and 2 contacted GC somata (Figure 18E, F). No evidence of

synaptic contacts onto mitral/tufted cells was observed for any dSAC subtype in any layer.

Visualization of intracellular biocytin at the EM level with a diaminobenzidine (DAB) reaction results in an electron-dense precipitate throughout the cytoplasm (Figure 18), preventing the access of primary antibodies to the aldehyde-fixed neurotransmitter molecules. To overcome this technical drawback, we visualized the intracellular biocytin with silver-enhanced ultrasmall gold particles (Figure 20). This technique not only allowed 3D light microscopic reconstruction of the cells and unequivocal identification of the filled processes at the EM level, but the visualization of GABA in the filled profiles was also possible. For each dSAC subtype, all examined terminals were immunopositive for GABA, as were their postsynaptic target cells (Figure 20).

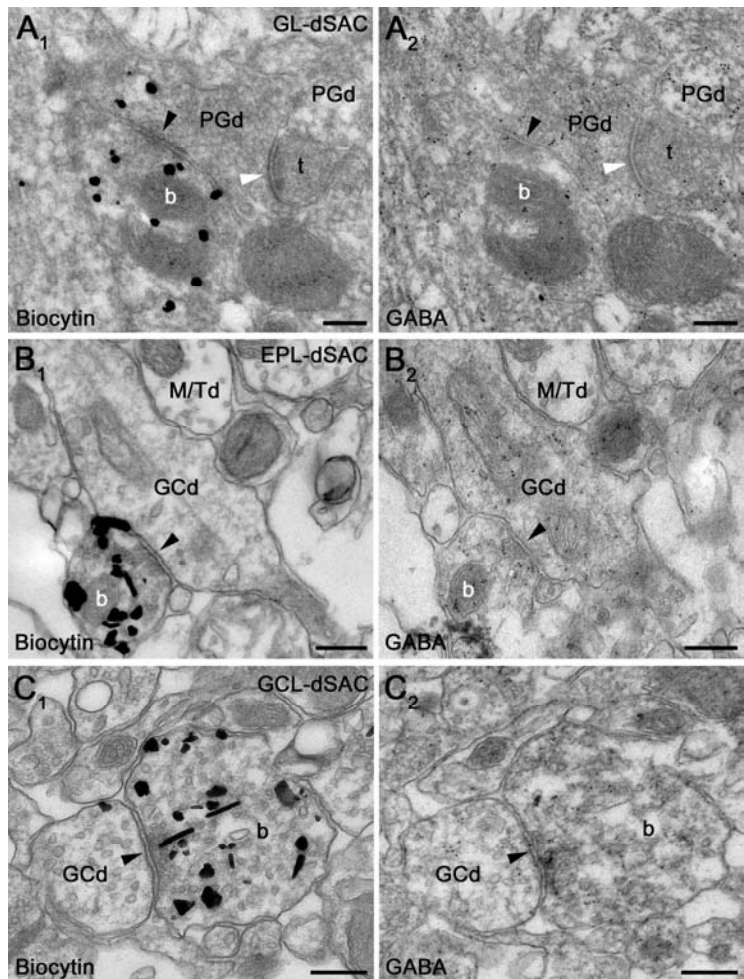


**Figure 20. Deep short-axon cells are GABAergic.** A1, A2. Serial ultrathin sections of a bouton (b) of a biocytin-filled (large silver-enhanced particles in A1) GL-dSAC (MA633) in the GL. The GABA immunopositive bouton (small gold particles in A2) forms a symmetrical synapse (black arrowhead) onto a GABA immunopositive periglomerular cell dendrite (PGd). The axon terminal (t) that establishes an asymmetric synapse (white arrowhead) on the same dendrite is GABA immunonegative. B1, B2. Serial sections of a biocytin-filled (large silver particles in B1) EPL-dSAC (MA796) bouton (b) in the EPL, which forms a symmetrical synapse (black arrowhead) onto a granule cell dendrite (GCd). Both the

presynaptic dSAC bouton and the postsynaptic dendrite contain a large number of gold particles labeling GABA. Note the lack of immunogold particles in the adjacent mitral/tufted cell dendrite (M/Td). C1, C2. Sequential ultrathin sections of a biocytin-filled (large silver particles in C1) GCL-dSAC (MA799) bouton (b) in the GCL, forming a symmetrical synapse (black arrowhead) onto a granule cell dendrite (GCd). Both the biocytin-filled terminal and the postsynaptic dendrite contain small immunogold particles labeling GABA. The large silver particles are not visible in the sections A2, B2 and C2 because they were removed during the immunogold labeling procedure. Scale bars in all panels: 250 nm. dSAC: deep short-axon cell; GL, EPL, GCL: glomerular, external plexiform, granule cell layer, respectively.

### **VI.2.7. Functional characterization of the synaptic outputs of deep short-axon cells**

Our ultrastructural data suggest that dSACs are GABAergic and that they provide synaptic inputs to local GABAergic interneurons. To functionally characterize the output of dSACs, I carried out paired whole-cell recordings from presynaptic dSACs and postsynaptic GCs. In 7 pairs, action potentials in the presynaptic dSACs induced short-latency, fast rising, exponentially decaying inward currents in the postsynaptic GCs (Figure 21).

The short latency of the responses ( $1.0 \pm 0.4$  ms, coefficient of variation (CV) of the latencies:  $0.18 \pm 0.8$ ,  $n=7$ ) indicate the monosynaptic nature of the unitary IPSCs (uIPSCs). These results offer functional evidence for our EM predictions that GABAergic interneurons are the postsynaptic targets of dSACs. The specific GABA<sub>A</sub>R antagonist SR95531 completely and reversibly blocked uIPSCs in all of the 6 pairs tested (Figure 21), functionally validating our immunohistochemical results that dSACs are GABAergic. The amplitude of the uIPSCs showed large within-cell ( $CV=1.5 \pm 0.8$ ,  $n=7$ ) and between-cell ( $CV=1.7$ ) variability. Unitary IPSCs with small amplitudes had slow rise times (RT), indicating severe dendritic filtering and distal dendritic locations of the synapses on the postsynaptic GC. When examining the kinetics of uIPSCs, I restricted my analysis to uIPSCs with a 10-90% RT of  $< 0.55$  ms. For the 4 pairs meeting this criterion, the 10-90% RT was  $0.42 \pm 0.1$  ms and the weighted decay time constant was  $6.6 \pm 1.6$  ms, which is 2.5-fold slower than that of mIPSCs recorded from dSACs ( $2.6 \pm 0.6$  ms, see Figure 17C). In two pairs, 1  $\mu$ M zolpidem, a benzodiazepine site agonist, prolonged the decay of uIPSCs.

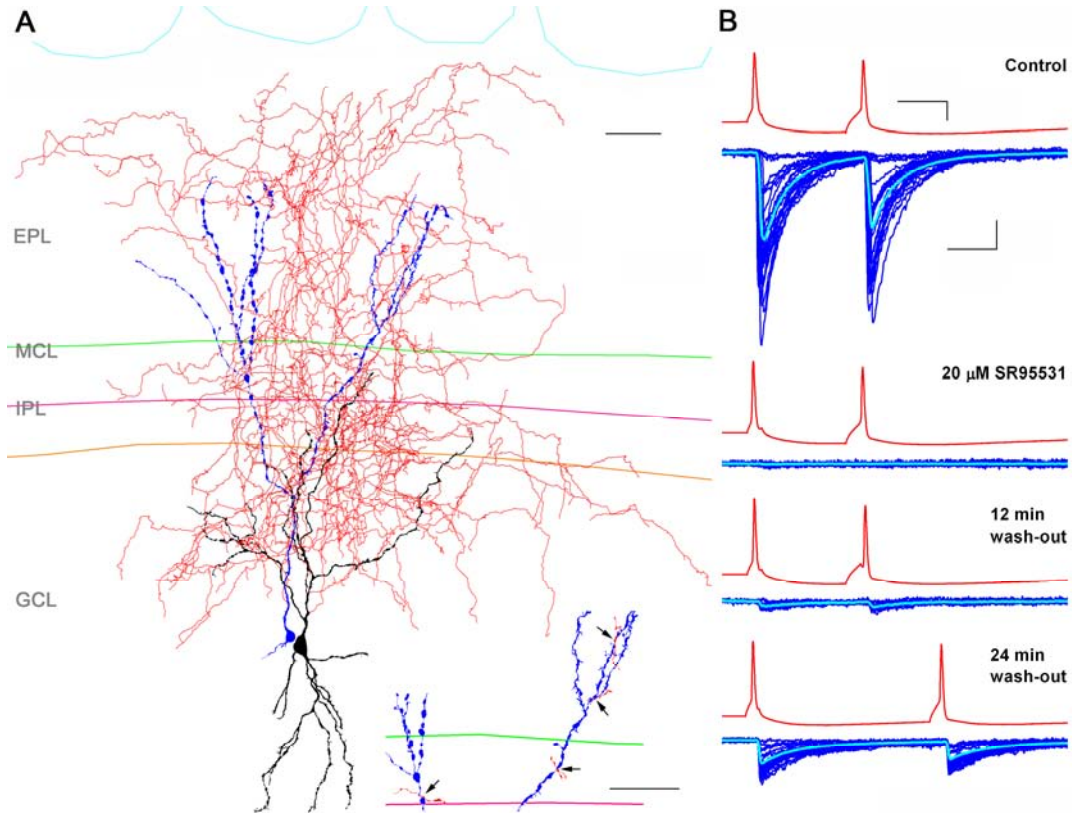


**Figure 21. Unitary postsynaptic responses between an EPL-dSAC and a granule cell are mediated by GABA<sub>A</sub> receptors.** A. NeuroLucida reconstruction of a presynaptic EPL-dSAC (soma, dendrites: black; axon: red) and its postsynaptic granule cell (blue; MA1050). Note the high axon density in the IPL and GCL. Inset demonstrates the positions of the potential contacts sites at a higher magnification. Scale bars: 50  $\mu$ m. B. Pairs of action potentials (50 Hz; 25 Hz in bottom panel) in the presynaptic dSAC (red traces) evoked fast rising (10-90% RT=0.33 ms) and exponential decaying ( $\tau_w=6.1$  ms) inward currents (individual traces: blue; averaged traces: light blue) in a granule cell (MA1050). The granule cell was held at -80 mV and was recorded with an intracellular solution containing high [Cl<sup>-</sup>], yielding an E<sub>Cl<sup>-</sup></sub>~30mV. The unitary IPSCs displayed large amplitude variability (CV=1.1). The averaged postsynaptic response showed slight paired-pulse depression. Bath application of the specific GABA<sub>A</sub> receptor antagonist SR95531 (20  $\mu$ M) abolished the inward currents. This effect could be partially recovered following the wash-out of the drug (lower panels). Scales: voltage traces: 10 ms/20 mV; current traces: 10 ms/50 pA. EPL, MCL, IPL, GCL: external plexiform, mitral cell, internal plexiform and granule cell layer, respectively; dSAC: deep short axon cell; IPSC: inhibitory postsynaptic current.

Next, I investigated the short-term plasticity of the postsynaptic responses. Two action potentials in the presynaptic dSACs were evoked at 50 or 25Hz and their effects on uIPSC amplitudes were analyzed. The short-term plasticity showed large variability;

some responses showed depression (Figure 21B), some facilitation and in one pair no plasticity was observed (Figure 22B).

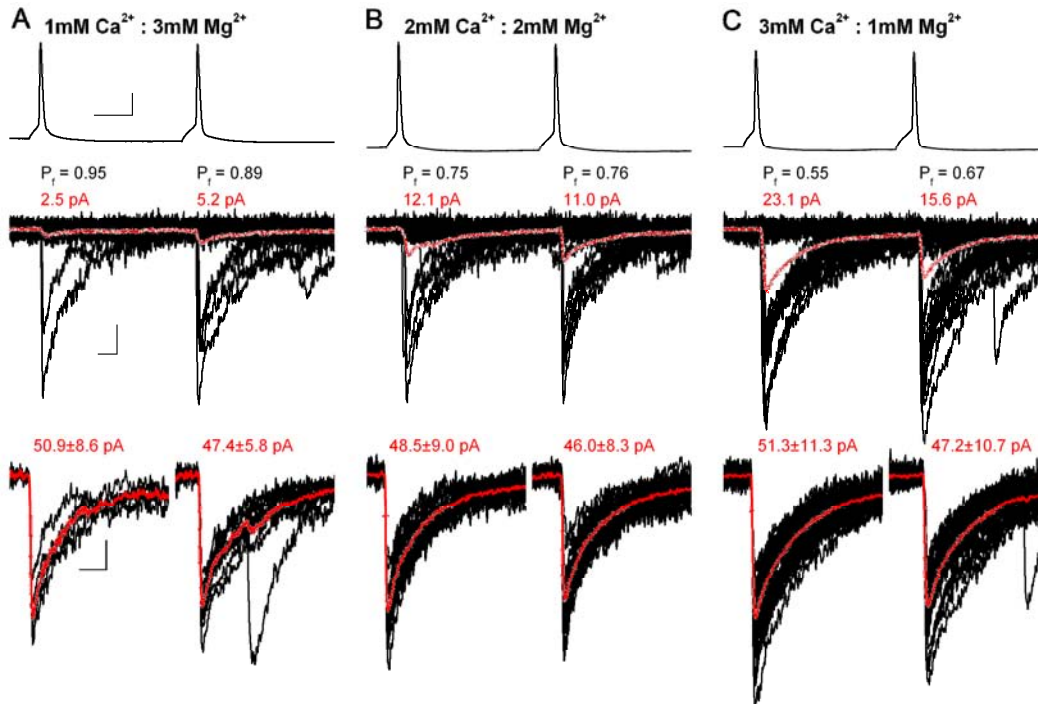


**Figure 22. Unitary IPSCs between a GCL-dSAC (MA1066) and a granule cell are mediated by a single release site.** A. Pairs (25 Hz) of presynaptic action potentials evoked postsynaptic responses with a very low probability when the  $[Ca^{2+}]_e$  was 1 mM. Under this low release probability ( $P_f$ ) condition, the averaged postsynaptic response showed paired-pulse facilitation, which was accompanied by a corresponding decrease in the failure rate. B. When the  $[Ca^{2+}]_e$  was increased to 2 mM, the failure rate decreased and the mean postsynaptic responses increased. There was no paired-pulse depression or facilitation under this  $P_f$  condition and the failure rate was similar for both action potentials. C. Elevating the  $[Ca^{2+}]_e$  to 3 mM further decreased the failure rate and increased the mean postsynaptic response to the 1<sup>st</sup> action potential. Under this  $P_f$  condition, the mean postsynaptic response showed paired-pulse depression. Despite the 9-fold increase in the success rate from  $[Ca^{2+}]_e$  of 1 mM to 3 mM, the potency (amplitude of successes without failures) did not change ( $50.9 \pm 8.6$  pA vs.  $51.3 \pm 11.3$  pA), indicating that the connection was mediated by a single functional release site. A-C. middle panels: 25 consecutive traces (black) and their superimposed averages (red); lower panels: all successful release events (black) within a 100 trial epoch and their superimposed averages (red). Scales: voltage traces: 10 ms/20 mV; current traces: 5 ms/10 pA

In this pair, however, changing the  $[Ca^{2+}]_e$  revealed short-term facilitation and depression, and demonstrated that the plasticity depends on the initial release

probability ( $P_r$ ). Changing the  $[Ca^{2+}]_e$  from 1 mM to 3 mM resulted in a 9-fold increase in the success rate (from 0.05 to 0.45), but did not affect the mean postsynaptic response amplitude excluding failures (potency at low  $P_r=50.9\pm 8.6$  pA; high  $P_r=51.3\pm 11.3$  pA; Figure 22), demonstrating the presence of a single functional release site. At this site, the  $P_r$  at 2 mM  $[Ca^{2+}]_e$  and 2 mM  $[Mg^{2+}]_e$  was 0.25 and the quantal size was 51 pA. The variance in the peak current of the successful events was remarkably small ( $CV\sim 0.2$ ), indicating high postsynaptic receptor occupancy.

For *post hoc* identification of the recorded cells, biocytin was included in the intracellular solutions of both pre- and postsynaptic cells. In 6 out of the 7 pairs, the presynaptic cell was successfully recovered, yielding 5 EPL-dSACs and one GCL-dSAC (MA1066, electrophysiology shown in figure 22). In four cases, the postsynaptic GC was also sufficiently filled for morphological identification. Unfortunately, the postsynaptic GC of the pair shown in figure 22 did not recover, precluding the anatomical determination of the number of synapses between the recorded cells. Figure 21A however, shows a NeuroLucida reconstruction of a presynaptic EPL-dSAC and its postsynaptic GC, and the positions and number of contact sites as determined at the light microscopy level. The four putative synapses are consistent with the impression that this connection is mediated by multiple functional release sites, as implicated from the mean amplitude, its variability, failure rate and the largest uIPSC recorded from this pair (Figure 21B).

Despite my repeated efforts I could not record GL-dSAC - PGC pairs, which is extremely challenging due to the enormous number of potential PGC targets within the area innervated by a single GL-dSAC. However, to provide a somewhat less direct functional evidence for the deep to superficial GABAergic connection in the main olfactory bulb, I carried out whole-cell recordings from PGCs and evoked IPSCs by extracellular stimulation in the IPL. In the presence of ionotropic glutamate receptor antagonists, extracellular stimulation in the IPL evoked short latency ( $1.9\pm 0.5$  ms) inward currents of variable amplitudes ( $49.4\pm 34.4$  pA; Figure 23).

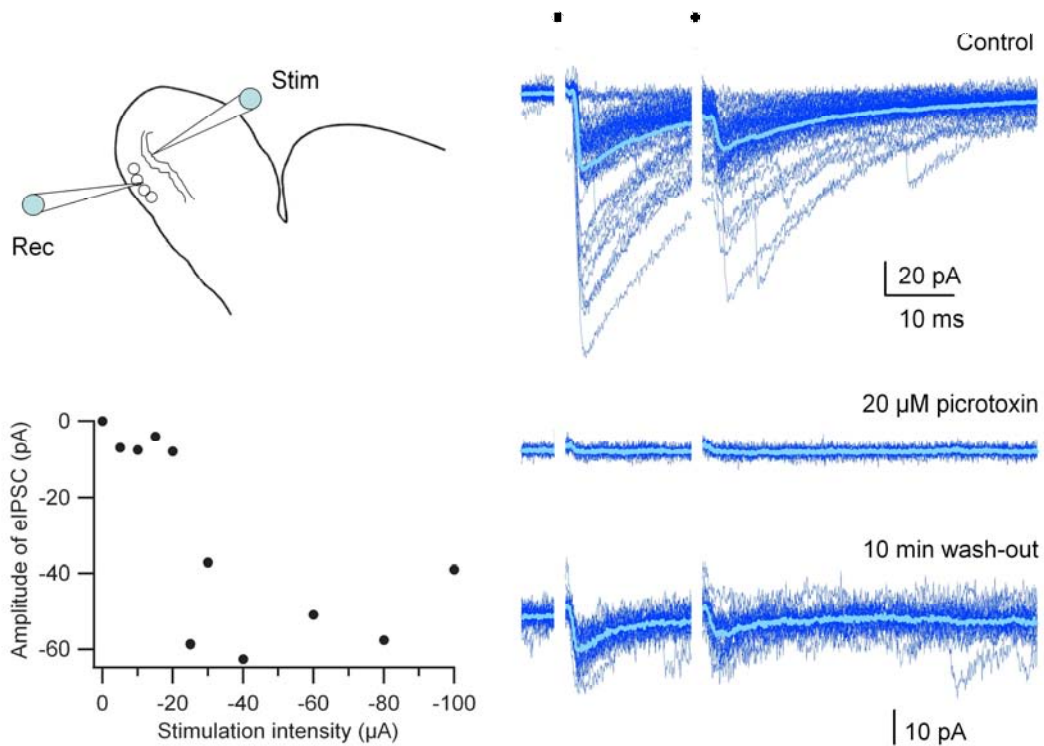


**Figure 23. Internal plexiform layer stimulation-evoked IPSCs in a periglomerular cell.** A. Schematic representation of the recording and stimulating configuration. B. The amplitude of the evoked IPSCs vs. the stimulus intensity plot shows that the responses appeared in an all-or-none manner, suggesting that the responses are mediated by a single fiber. C. Two stimuli at 50Hz evoked inward currents of variable amplitudes with short latencies. The mean postsynaptic response (light blue) showed paired-pulse depression. 20  $\mu\text{M}$  picrotoxin completely and reversibly blocked the inward currents, demonstrating that they were mediated by  $\text{GABA}_A$  receptors. Black dots above the current traces indicate the timing of the stimuli. The stimulus artifacts have been digitally removed from the traces. eIPSC: evoked inhibitory postsynaptic current. Rec, Stim: recording and stimulating electrode, respectively.

The presence of glutamate receptor antagonists in the bath, the short and uniform latencies, and the monotonous rise indicate the monosynaptic nature of these IPSCs. The  $\text{GABA}_A$  receptor blocker picrotoxin (20  $\mu\text{M}$ ) completely and reversibly eliminated the inward currents, providing a functional demonstration of a  $\text{GABA}_A$  receptor-mediated deep to superficial layer connection in the main olfactory bulb.

### VI.2.8. Summary of the results and conclusions

In the second part of my work, employing a combined *in vitro* electrophysiological and anatomical approach I made the following observations:

1. Provided evidence for the existence of 3 distinct dSAC subtypes in the main olfactory bulb, which are the GL-, EPL and GCL-dSACs.
2. Demonstrated subtype-specific differences in their
  - axo-somato-dendritic morphologies,
  - expression of the GABA<sub>A</sub>R  $\alpha$ 1 subunit content,
  - intrinsic electrical properties, and
  - their postsynaptic target cells.
3. GL-dSACs establish a novel intrabulbar GABAergic connection from deep to superficial layers, whereas
4. GCL-dSACs directly signal the activity of the main olfactory bulb to higher olfactory areas.
5. All dSAC subtypes are GABAergic, and they
6. Selectively innervate GABAergic periglomerular and granule cells.
7. EPL- and GCL-dSACs innervate granule cells through the activation of  $\alpha$ 2 and  $\gamma$ 2 subunit-containing GABA<sub>A</sub>Rs.

## VII. DISCUSSION

In the present work I utilized a toolbox of *in vitro* electrophysiological, anatomical and statistical techniques to address how the heterogeneity in structural and functional properties as well as synaptic connectivity of certain nerve cell populations in the rat main olfactory bulb correlate with each other, by describing two nerve cell populations, the external tufted and deep short-axon cells. The morphological analysis was carried out by my long-standing collaborator Dr. Mark D. Eyre Ph.D.

### VII.1. Correlation of functional and structural characteristics predicts two subpopulations of external tufted cells.

In the first part of my work I demonstrated the presence of two subpopulations of external tufted cells (ETCs) of the rat main olfactory bulb based on their active and passive intrinsic electrical properties and their dendritic morphologies. Although 24 out of the 30 measured parameters significantly differed between the two ETC subpopulations, qualitatively the most prominent differences between them were the presence and absence of basal dendrites and the lack and presence of action potential bursting, respectively. Although our quantitative analysis indicated the existence of only two ETC subpopulations, a large heterogeneity in both physiological and morphological properties within each subpopulation was apparent. I propose that the two ETC populations serve very different roles in the main olfactory bulb circuit, and the within-group heterogeneity is the reflection of further specialization evolved to fulfill less prominent functional requirements.

#### VII.1.1. Our results are in agreement with classical morphological studies.

The morphological heterogeneity of ETCs has long been described and the existence of 3 subtypes has been proposed. The first detailed investigation of the dendritic arborizations of ETCs was carried out by Macrides and Schneider (1982) using the Golgi impregnation technique. They concluded that ETCs are comprised of 3 subpopulations; the first group of ETCs lack secondary dendrites; ETCs in the second group have extensively branched, spatially restricted secondary dendrites, and the third group have sparsely branched secondary dendrites, which extend tangentially in one

direction from the soma. Our morphological results are in perfect agreement with the presence of these morphological features, tempting the division of ETCs into these 3 categories. However, unsupervised cluster analysis revealed only two subpopulations of ETCs; differences between ETCs with extensively or sparsely branched secondary dendrites were not significant. Macrides and Schneider (1982) have also suggested that ETCs that lack secondary dendrites have a larger glomerular arbor than those with secondary dendrites. Their conclusion was based on the measured area of the two-dimensional projection of the apical dendrites. The results of our quantitative analysis are in disagreement with their conclusion, because detailed three-dimensional measurements of the total dendritic length, the number of segments and the largest extent (sholl max) of the dendrites in the glomerular layer have revealed significantly smaller values for cells in cluster 1 (without basal dendrites) than in cluster 2. Differences in basal dendrites and in the sizes of their glomerular dendritic arbors might impart different functional characteristics to the two ETC subpopulations.

#### **VII.1.2. The molecular heterogeneity of external tufted cells**

External tufted cells are not only heterogeneous based on their dendritic and axonal distributions, but they express distinct sets of ion channels. The ionotropic GABA<sub>A</sub> receptor  $\alpha 1$  and  $\alpha 3$  subunits are differentially expressed by ETCs (Panzanelli et al., 2005). Some cells express only the  $\alpha 1$ , some others only the  $\alpha 3$  and approximately 40% of the cells contain both of these  $\alpha$  subunits. Interestingly, ETCs with secondary dendrites predominantly express the  $\alpha 3$  subunit, resulting in a strongly immunoreactive dendritic plexus in the outer one third of the external plexiform layer (EPL). A previous report from my supervisor, Dr. Zoltan Nusser's laboratory also described that ETCs are heterogeneous with respect to their expression of the hyperpolarization activated and cyclic nucleotide-gated mixed cation channel 1 (HCN1; (Holderith et al., 2003)). Most of the HCN1 immunopositive ETCs do not seem to have basal dendrites, and are likely to belong to cluster 1.

### **VII.1.3. Basal dendrites – morphological predictors of bursting behavior in external tufted cells?**

In a recent study, Hayar et al. (2004a) have investigated the morphological and electrophysiological properties of ETCs. Several of our findings are in perfect agreement, including 1) approximately one third of the ETCs possess basal dendrites; 2) basal dendrites show variable ramification patterns; 3) the apical tuft of most ETCs arborizes in a single glomerulus, but a few percent of the ETCs project their apical dendrites into two glomeruli; 4) the extent of the intra-glomerular arborization of the apical dendrites varies considerably (5-fold) from small fan-like tufts to extensive globular tufts; 5) some cells project their axons towards the mitral cell and granule cell layer without extensive ramification; 6) whereas some other ETCs had extensive local axon collaterals. Interestingly, despite the observed morphological heterogeneity of ETCs, Hayar et al. (2004a) described rather uniform electrophysiological properties of the ETCs. Most notably, they reported only burst firing behaviors irrespective of whether spontaneous activity was monitored in cell-attached mode or firing was evoked by current injections in the whole-cell configuration. Because they reported that one third of their recorded cells had basal dendrites, but all cells showed bursting behavior, it may be appropriate to designate cells with basal dendrites as also possessing bursting behavior. This is in contrast with my results demonstrating that the majority of cells in cluster 2 (which all have basal dendrites) did not fire bursts of action potentials (APs). This conclusion is consistent with the results of my cell-attached recordings, demonstrating that the majority of the cells with basal dendrites lack spontaneous bursting, and thus the differences cannot be the consequence of dialysis of the cells during whole-cell recordings. A possible reason for this discrepancy could be due to a sub-selection of ETCs recorded by Hayar et al. (2004a). As discussed above, I have taken utmost care to avoid any bias in my sampling of juxtglomerular cells with diameter  $>10\ \mu\text{m}$ . Another possible reason could be the different strain and age of the animals (Hayar: P21-P29 Sprague Dawley vs. our study: P26-P78 Wistar). Some of the morphological features of cluster 2 cells are similar to some of the superficially located middle tufted cells (Macrides and Schneider, 1982), or as another study calls them ‘superficial’ tufted cells (Hamilton et al., 2005). However, one obvious difference between these cells and the ETCs in our study is that the somata of these cells are

located in the EPL, whereas all cells of our study were in a juxtglomerular position. Despite the different names, their functional roles could be very similar in olfactory processing. It is interesting to note that Hamilton et al. (2005) have described both bursting and non-bursting firing properties for ‘superficial’ tufted cells, whereas in my work, only a single cell in cluster 2 showed bursting behavior; the rest displayed regular or irregular-accommodating firing patterns.

#### **VII.1.4. What could be the major functional differences between the two types of external tufted cells?**

As already discussed by Macrides and Schneider (1982), the main difference between ETCs with and without basal dendrites is their potential innervation and lack of innervation by granule cells, respectively. External tufted cells without secondary dendrites (cluster 1 in our work) are likely to receive GABAergic inputs only from periglomerular and short-axon cells onto their apical tufts. These cells could still receive feed-forward and feed-back inhibition, and could also sense the activity of some neighboring glomeruli. However, ETCs with extensive secondary dendrites will also integrate feed-back GABAergic inputs from granule cells and sample the neuronal activity from a much larger area of the bulb. Our results also revealed that these cells have significantly larger glomerular dendritic trees. If the two types of ETCs have similar synaptic densities per unit dendritic length, this would predict a more robust sensory innervation of ETCs with secondary dendrites. Our qualitative observation that ETCs with basal dendrites possess a much larger and more extensively ramifying local axonal arbor predicts an additional functional difference between the two types of ETCs. In summary, ETCs in cluster 2 are predicted to receive much more sensory input, form connections with a higher number of cells in the glomerular layer (GL) and EPL and sample the network activity through interacting with granule cells from a much larger area of the bulb. It has also been suggested that a different ETC populations may be responsible for the commissural innervation of the contralateral main olfactory bulb through the anterior olfactory nucleus pars externa and for the latero-medial intrabulbar associational connection on the opposite side of the same bulb (Schoenfeld et al., 1985). These pathways allow communication among principal cells via granule cells, suggesting a key role for ETCs in processing olfactory sensory information. Whether

the two ETC subpopulations are responsible for this functional difference or whether cells within each subgroup participate in both commissural and associational projections remains to be determined. However, these authors also noted that most if not all ETCs in the superficial two-thirds of the GL have neither intrabulbar nor bulbofugal axonal projections. Interestingly, I found that most cells lacking basal dendrites (cluster 1) were recorded from such locations.

#### **VII.1.5. Subthreshold resonance properties show correlation with structural attributes.**

Another important feature of the ETCs with bursting firing pattern is that they show different subthreshold resonant behaviors than cells with basal dendrites. A larger proportion of the bursting cells have active resonance at the theta frequency range. In addition, a very significant proportion of these cells are spontaneously active at the theta frequency range even in *in vitro* slices, indicating that their activity could be associated with the theta rhythm (Adrian, 1950; Freeman, 1975; Laurent and Davidowitz, 1994). ETCs with basal dendrites have an intrinsic resonant frequency below 1 Hz, a frequency range which is below the frequency of local field potential oscillations observed *in vivo* (Adrian, 1950; Freeman, 1975; Laurent and Davidowitz, 1994). Thus, I predict that these ETCs may not participate in the theta frequency oscillation. Whether they are entrained to gamma frequency oscillations like mitral and middle/internal tufted cells (Desmaisons et al., 1999) or do not fire rhythmically at all, remains to be determined.

#### **VII.2. Novel intra- and extrabulbar GABAergic connections in the main olfactory bulb are provided by distinct subtypes of deep short-axon cells.**

In the second part of my dissertation, I provided evidence for the existence of 3 distinct deep short-axon cell subtypes in the main olfactory bulb, which are the glomerular layer (GL-), external plexiform layer (EPL-) and granule cell layer- (GCL-) dSACs. Subtype-specific differences were found in their axo-somato-dendritic morphologies, expression of the GABA<sub>A</sub>R  $\alpha 1$  subunit, intrinsic electrical properties and their postsynaptic target cells. Glomerular layer-dSACs establish a novel intrabulbar GABAergic connection from deep to superficial layers, whereas GCL-dSACs directly

signal the activity of the bulb to higher olfactory areas. Furthermore, we have also clearly shown that all dSAC subtypes are GABAergic and they selectively innervate GABAergic periglomerular cells and granule cells. Using paired whole-cell recordings I demonstrated that EPL- and GCL-dSACs innervate granule cells through the activation of  $\alpha 2$  and  $\gamma 2$  subunit-containing GABA<sub>A</sub>Rs.

### **VII.2.1. Heterogeneity and classification of dSACs**

Early studies using the Golgi impregnation technique have noted the morphological heterogeneity of olfactory bulb neurons, including deep short-axon cells (dSACs) (Blanes, 1898; Cajal, 1911; Price and Powell, 1970a; Schneider and Macrides, 1978). Four categories of dSACs were distinguished based on characteristic morphological features such as *i*) perpendicular (vertical Cajal cells), *ii*) parallel (horizontal cells) dendrites relative to the bulbar lamination, or *iii*) a non-oriented dendritic arbor (Blanes and Golgi cells); and the *1*) presence (Blanes cells) or *2*) absence (Golgi, vertical Cajal and horizontal cells) of dendritic spines. Other studies using immunolabeling techniques to visualize dSACs have described further categories, including deep stellate cells in the monkey (Alonso et al., 1998; Crespo et al., 2001), piriform and fusiform dSACs in the hedgehog (Brinon et al., 2001), and giant cells of the white matter in the rat (Brinon et al., 1992), but none have taken the axonal arborization of the cells into account.

We observed dSACs with somato-dendritic morphologies reminiscent of all the classical categories. However, we could recover almost the entire axonal arbors of the recorded neurons, leading to the emergence of a much more complex picture. Cells with a similar somato-dendritic morphology can possess very different axonal ramification patterns, and cells with a similar axonal arbor can have very different somato-dendritic morphologies. For example, we observed both horizontal-like and Golgi-like cells that predominantly innervated the glomerular layer, and conversely we identified cells with horizontally oriented dendrites that innervated either the GL or only the GCL. Because of this, we avoided the straightforward adaptation of the traditional classification and performed unsupervised cluster analysis of the cells based on both their axonal and dendritic arbors, which indicated the presence of 3 distinct dSAC subtypes. Additional dSAC subpopulations may exist, but our large sample size (~160

dSACs) indicates that they should comprise a very small fraction of all dSACs. Indeed, several neuropeptides (NPY, VIP, somatostatin), calcium binding proteins (CB, parvalbumin, calretinin, neurocalcin), some receptors (m2 acetylcholine receptor), and enzymes (ACh-esterase, NADPH-diaphorase, NOS) have been used previously as dSAC markers, but were found to label only small subpopulations of dSACs (Nickell and Shipley, 1988; Brinon et al., 1992; Alonso et al., 1998; Brinon et al., 1999; Crespo et al., 2000; Alonso et al., 2001; Brinon et al., 2001; Crespo et al., 2002; Gracia-Llanes et al., 2003; Kosaka and Kosaka, 2007). Due to the lack of complete visualization of axonal and dendritic arbors following immunohistochemical labeling, it is impossible at present to determine whether these neurochemically identified dSACs form subsets of the GL-, EPL- or GCL-dSAC subtypes or whether they represent separate, non-overlapping subpopulations. The latter is probably true for VIP immunopositive dSACs that selectively innervate other VIP positive dSACs (Gracia-Llanes et al., 2003). In our sample, we did not see any dSACs that selectively innervated other dSACs, but the lack of sampling of these VIP positive cells is likely to be due to their rarity (Gracia-Llanes et al., 2003). Willhite et al. (2006) have demonstrated that viral injection into the glomerular layer of the main olfactory bulb resulted in column-like labeling of granule cells (GCs) and mitral/tufted cells (M/TCs). The axonal arbor of EPL-dSACs could also be seen as another indication of the column-like organization of the main olfactory bulb. It remains to be seen how the GC columns and the column-like axonal arbor of EPL-dSACs relate to each other in space.

### **VII.2.2. Granule cell layer-dSACs mediate a novel extrabulbar GABAergic projection**

Long-range GABAergic projections are a well known feature of many brain regions where GABAergic cells form the sole output (e.g. cerebellar cortex, several nuclei of the basal ganglia) as well as areas where the primary projection is glutamatergic. For example, GABAergic projections from the neocortex (Gonchar et al., 1995) and hippocampus (Alonso and Kohler, 1982; Toth and Freund, 1992; Jinno et al., 2007) have been described and their functional roles have been examined. In the main olfactory bulb, glutamatergic M/TCs provide the main output. They receive direct input from the axons of the olfactory sensory neurons and following complex local processing

transfer their activity to higher olfactory areas. In the piriform cortex, M/TC axons mainly target pyramidal cell apical dendrites and to a much smaller extent local circuit interneurons (INs). My results indicate that GCL-dSACs synthesize the activity of the main olfactory bulb network by sampling excitation from a large number of M/TC probably associated with multiple glomeruli and therefore may participate in different representations (Xu et al., 2000). In turn, they then project this information to the same downstream olfactory areas as M/TCs. Revealing the postsynaptic target cells of GCL-dSAC axons in higher olfactory areas will be essential for understanding how they influence the activity of these brain regions. My hypothesis is that the selective innervation of local circuit GABAergic interneurons in the piriform cortex would be an ideal method of synchronizing the rhythmic activity of the main olfactory bulb with that of higher cortical areas (Laurent, 2002).

### **VII.2.3. Deep short-axon cells are interneuron-selective interneurons**

When the potential functional roles of dSACs are considered, one of the most important issues is determining whether they use glutamate or GABA as the main neurotransmitter. The GABAergic nature of VIP, NPY and CB immunopositive dSAC subpopulations has been demonstrated previously (Gracia-Llanes et al., 2003). However, the fact that some juxtglomerular short-axon cells are suggested to be glutamatergic (Aungst et al., 2003) prompted us to perform postembedding immunogold reactions for GABA. Our EM analysis demonstrated that the axon terminals of all dSACs subtypes are GABA immunopositive and form symmetrical synapses onto their GABAergic postsynaptic target cells. In the last series of experiments, I performed paired whole-cell recordings between dSACs and GCs and found that the postsynaptic responses in 6 out of 6 cell pairs tested were completely and reversibly blocked by the specific GABA<sub>A</sub>R antagonist SR95531. These experiments provided functional evidence for the GABAergic nature of EPL- and GCL-dSACs, and that at least some of their postsynaptic targets are GCs. Electron microscopic examination of the postsynaptic target profiles of 152 synapses of 9 dSACs revealed that M/TCs are not among their targets, but, instead, they exclusively innervate other GABAergic INs. Such IN-selective INs are not unique to the main olfactory bulb (Gracia-Llanes et al., 2003), as several subpopulations have also been described in the

hippocampus (Acsady et al., 1996; Gulyas et al., 1996; Gulyas et al., 2003) and neocortex (Meskenaite, 1997).

#### **VII.2.4. Novel intrabulbar connections between deep and superficial layers of the main olfactory bulb**

The existence of dSACs with widespread axonal ramification almost exclusively in the glomerular layer is one of the most surprising and pioneering findings of our work. To my knowledge, this is the first description of an intrabulbar connection from the inframitral layers to the sensory input layer. These GL-dSACs receive very prominent excitation from M/TCs and feed their activity back to the glomerular layer through the selective innervation of GABAergic periglomerular cells (PGCs). The classical interpretation of such a connection is that GL-dSACs disinhibit M/TCs. GABA<sub>A</sub>R-mediated synaptic currents (Puopolo and Belluzzi, 1998b; Smith and Jahr, 2002) as well as inhibitory synaptic contacts onto PGCs (Pinching and Powell, 1971b, c; Kosaka et al., 1998) have long been demonstrated. The source of GABA was assumed to originate from other PGCs and superficial SACs. Although our results cannot exclude the possibility of PGC-PGC and superficial SAC-PGC connections, they do reveal a new source of GABAergic input to PGCs. Inhibition of PGCs will not only reduce their inhibition of M/TCs, but will also reduce the modulation of synaptic transmission at olfactory receptor neuron terminals mediated by presynaptic GABA<sub>B</sub> and D<sub>2</sub> receptors (Aroniadou-Anderjaska et al., 2000; Wachowiak et al., 2005). Finally, GL-dSACs could also play a role in interglomerular synchronization through PGCs, but this remains to be experimentally demonstrated.

#### **VII.2.5. Properties of granule cell inhibition by deep short-axon cells.**

As in all nerve cells, GABAergic GCs also receive GABA<sub>A</sub>R-mediated inhibition (Nusser et al., 1999; Nusser et al., 2001b; Pressler and Strowbridge, 2006) and express several GABA<sub>A</sub>R subunits (Fritschy and Mohler, 1995; Nusser et al., 1999; Sassoe-Pognetto et al., 2000; Nusser et al., 2001b). Immunohistochemistry has demonstrated the presence of  $\alpha 2$ ,  $\alpha 5$ ,  $\beta 3$ ,  $\gamma 2$  and  $\delta$  subunits in GCs. Kinetic analysis and benzodiazepine pharmacology of unitary IPSCs recorded from GCs are consistent with  $\alpha 2\beta 3\gamma 2$  subunit-containing GABA<sub>A</sub>Rs being responsible for their synaptic inhibition.

My recordings demonstrate that the decay of IPSCs is 2.5-fold slower in GCs than in dSACs, consistent with the expression of different GABA<sub>A</sub> receptor subunits in these cell types ( $\alpha 1$ ,  $\beta 2$ ,  $\gamma 2$  in dSAC vs.  $\alpha 2$ ,  $\alpha 5$ ,  $\beta 3$ ,  $\gamma 2$ ,  $\delta$  in GCs; (Fritschy and Mohler, 1995; Nusser et al., 1999). Further physiological characterization of the unitary connections between dSACs and GCs revealed variable short-term plasticity, and demonstrated that the plasticity depends on the initial release probability.

#### **VII.2.6. Significance of deep short axon cells in olfactory information processing**

Synchronized oscillatory activity is thought to be important for information processing for many sensory modalities, including olfaction (Laurent et al., 2001). In the main olfactory bulb, mitral cell synchrony is essentially driven by inhibitory postsynaptic potentials imposed by granule cells, which are themselves synchronized by their excitatory inputs from mitral cells. The observed rapid synchrony emerges from this precise back-and-forth interplay between neuronal populations (Schoppa, 2006a, b). Lateral inhibition between principal cells of the olfactory bulb is also mediated by circuits that involve these reciprocal dendro-dendritic connections, the function of which may be to reveal specific, discrete patterns of glomerular activation (Urban, 2002). Inputs, such as deep short-axon cells, that influence granule cell activity will therefore have a critical effect on oscillatory synchronization.

## VIII. SUMMARY

To understand the cellular and synaptic mechanisms of olfactory information processing, the intrinsic properties and synaptic connectivity of the different types of nerve cells in the main olfactory bulb need to be deciphered. The main objective of my work was to identify whether heterogeneity in structural and functional properties as well as synaptic connectivity of certain nerve cell populations in the main olfactory bulb correlate with each other, resulting in well defined subpopulations of cells; or whether these measured features of the cells vary independently, resulting in a single but highly diverse population.

First, I determined the active and passive electrical properties of external tufted cells (ETCs) using *in vitro* whole-cell recordings and then I correlated them to their dendritic arborization patterns. Principal component followed by agglomerative cluster analysis revealed two distinct subpopulations of ETCs based on their electrophysiological properties. Eight out of twelve measured physiological parameters exhibited significant difference between the two subpopulations, including the membrane time constant, amplitude of spike after-hyperpolarization, variance in the inter-spike interval distribution and subthreshold resonance. Cluster analysis of the morphological properties of the cells also revealed two subpopulations, the most prominent dissimilarity between the groups being the presence or absence of secondary, basal dendrites. Finally, clustering the cells taking all measured parameters into account also indicated the presence of two subpopulations that mapped in an almost perfect one-to-one fashion to both the physiologically and the morphologically derived groups. My results demonstrate that a number of functional and structural properties of ETCs are highly predictive of one another. However, cells within each subpopulation exhibited pronounced variability, suggesting a large degree of specialization evolved to fulfill specific functional requirements in olfactory information processing.

A universal feature of neuronal microcircuits is the presence of GABAergic interneurons that control the activity of glutamatergic principal cells and each other. In the second part of my work I used a combined electrophysiological and morphological approach to investigate a rather mysterious cell population of the main olfactory bulb. Deep short-axon cells (dSACs) of the inframitral layers are GABAergic and have

extensive and characteristic axonal ramifications in various layers of the bulb, based on which unsupervised cluster analysis revealed three distinct subtypes, the glomerular (GL-), external plexiform (EPL-) and granule cell layer- (GCL-) dSACs. Each dSAC subtype exhibited different electrical properties, but received similar GABAergic and glutamatergic inputs. The local axon terminals of all dSAC subtypes selectively innervated GABAergic granule and periglomerular cells and evoked GABA<sub>A</sub> receptor-mediated inhibitory postsynaptic currents. One subpopulation of dSACs (GL-dSAC) creates a novel intrabulbar projection from deep to superficial layers. Another subpopulation (GCL-dSAC) was labeled by retrogradely-transported fluorescent microspheres injected into higher olfactory areas, constituting a novel projection-cell population of the main olfactory bulb. My results reveal multiple dSAC subtypes, each specialized to influence main olfactory bulb activity by selectively innervating GABAergic interneurons, and provide direct evidence for novel intra- and extrabulbar GABAergic projections.

## ÖSSZEFOGLALÁS

Ahhoz, hogy megértsük az illatok érzékelésének celluláris és szinaptikus mechanizmusait, meg kell ismernünk a szaglógumó különböző sejttípusainak belső tulajdonságait és szinaptikus kapcsolatrendszerét. Munkám fő célkitűzése az volt, hogy vizsgáljam a szaglógumó bizonyos sejtpopulációinak strukturális és funkcionális heterogenitását, illetve szinaptikus kapcsolatrendszerük közötti összefüggéseket. Tanulmányozni akartam, hogy a morfológiai, funkcionális és szinaptikus jellemzők alapján a szaglógumó egyes sejttípusai jól elkülöníthető alcsoportokra oszthatók-e. Vizsgálataimat a szaglógumó két sejtcsoportján: a külső ecsetsejteken és a mély rövid-axonú sejteken (mRAS) végeztem.

Munkám első részében, meghatároztam a külső ecsetsejtek aktív és passzív elektromos tulajdonságait *in vitro* egész-sejtes patch-clamp elvezetések segítségével, majd a mért elektromos tulajdonságokat összevettem dendritjeik elágazódási mintázatával. Az elektromos és morfológiai tulajdonságokat külön-külön elemezve főkomponens analízis és azt követő agglomeratív csoportosító analízis (*cluster analysis*) a külső ecsetsejteket elektrofiziológiai tulajdonságaik alapján két élesen elkülönülő csoportra osztotta. A tízenkét elemzett fiziológiai paraméterből nyolc adódott szignifikánsan különbözőnek a két csoport között (pl. membrán időállandó, akciós potenciált követő utóhiperpolarizáció amplitúdója, az akciós potenciálok közötti időintervallum eloszlásának varianciája, a tüzelési küszöb alatti rezonancia). A morfológiai tulajdonságok cluster analízise hasonló módon két csoportra osztotta a sejteket. A csoportok közötti legszembetűnőbb alaki különbség a másodlagos (bazális) dendritek megléte vagy hiánya volt. Végül, az elektrofiziológiai és a morfológiai paraméterek egyidejű figyelembevételével végeztem el a cluster analízist. Ez az elemzés szintén két csoportot képzett. Ráadásul, az így létrehozott csoportok, szinte tökéletesen megegyeztek mind az elektrofiziológiai, mind a morfológiai tulajdonságok alapján származtatott csoportokkal. Eredményeim azt mutatják, hogy a külső ecsetsejtek számos funkcionális és morfológiai tulajdonsága kölcsönösen prediktív jellegű. Azonban a sejtek az egyes alpopulációkon belül kifejezett változékonyságot mutattak, jelezve ezáltal azt a magas fokú specializációt, ami a szaglási információ-feldolgozás sajátos funkcionális követelményeinek kielégítésére fejlődött ki.

Idegi mikrohálózatok egyik általános tulajdonsága az olyan GABAerg interneuronok jelenléte, amelyek meghatározzák egymás és más glutamaterg fősejtek aktivitását. Munkám második részében a szaglógumó egyik igen rejtélyes sejtpopulációjának, a mRAS-eknek vizsgáltam az elektrofiziológiai, morfológiai és szinaptikus tulajdonságait. A mitrális sejtek rétege alatt elhelyezkedő mRAS-ek kiterjedt és jellegzetes axonális elágazódással rendelkeznek, amely alapján végzett cluster analízis a sejteket három, egymástól élesen különböző altípusra választotta szét. Ezek név szerint az axonjaikat elsősorban a glomeruláris rétegbe vetítő (GL-mRAS), a külső plexiform rétegbe vetítő (EPL-mRAS) és a szemcsesejt rétegbe vetítő (GCL-mRAS) mély rövid-axonú sejtek. Kimutattuk, hogy az axonelágazódási mintázatuk alapján elkülönülő egyes altípusok elektromos tulajdonságaikban is különböznek egymástól; ugyanakkor hasonló glutamaterg és GABAerg bemenetet kapnak. Úgy találtuk, hogy az egyes altípusokhoz tartozó sejtek lokális axonvégződéseik szelektíven GABAerg szemcse- és periglomeruláris sejteket innerváltak, és GABA<sub>A</sub> receptor-közvetítette gátló posztszinaptikus áramokat váltottak ki. A sejtek axonelágazódását vizsgálva azt találtuk, hogy a mRAS-ek egyik alpopulációja (GL-mRAS) egy eddig nem ismert, a szaglógumó mély és felszínes rétegeit összekötő projekciós axonrendszert alakít ki. A magasabb szagló-agyi területekre injektált, retrográd módon transzportálódó fluoreszcens mikrogömbök segítségével a mély rövid-axonú sejtek egy másik alpopulációját (GCL-mRAS) is sikerült szelektíven megjelölnünk, amelyekről így elsőként sikerült bizonyítanunk, hogy a korábban ismert mitrális és ecsetsejtek mellett részét képezik a szaglógumó projekciós rendszerének. Eredményeim egyrészt számos mRAS altípus létezését bizonyítják, melyek a GABAerg interneuronok szelektív jellegű beidegzésével befolyásolják a szaglógumó aktivitását, másrészt direkt módon mutattunk rá újfajta, szaglógumón belüli és kívüli GABAerg projekciós rendszerek létezésére.

## IX. BIBLIOGRAPHY

### IX.1. General bibliography

- Acsady L, Gorcs TJ, Freund TF (1996) Different populations of vasoactive intestinal polypeptide-immunoreactive interneurons are specialized to control pyramidal cells or interneurons in the hippocampus. *Neuroscience* 73:317-334.
- Adrian ED (1950) The electrical activity of the mammalian olfactory bulb. *Electroencephalography and Clinical Neurophysiology* 2:377-388.
- Allison AC (1953) The morphology of the olfactory system in the vertebrates. *Biological Reviews* 28:195-244.
- Alonso A, Kohler C (1982) Evidence for separate projections of hippocampal pyramidal and non-pyramidal neurons to different parts of the septum in the rat brain. *Neuroscience letters* 31:209-214.
- Alonso JR, Brinon JG, Crespo C, Bravo IG, Arevalo R, Aijon J (2001) Chemical organization of the macaque monkey olfactory bulb: II. Calretinin, calbindin D-28k, parvalbumin, and neurocalcin immunoreactivity. *J Comp Neurol* 432:389-407.
- Alonso JR, Porteros A, Crespo C, Arevalo R, Brinon JG, Weruaga E, Aijon J (1998) Chemical anatomy of the macaque monkey olfactory bulb: NADPH-diaphorase/nitric oxide synthase activity. *J Comp Neurol* 402:419-434.
- Aroniadou-Anderjaska V, Zhou FM, Priest CA, Ennis M, Shipley MT (2000) Tonic and synaptically evoked presynaptic inhibition of sensory input to the rat olfactory bulb via GABA(B) heteroreceptors. *J Neurophysiol* 84:1194-1203.
- Aungst JL, Heyward PM, Puche AC, Karnup SV, Hayar A, Szabo G, Shipley MT (2003) Centre-surround inhibition among olfactory bulb glomeruli. *Nature* 426:623-629.
- Bartolomei JC, Greer CA (1998) The Organization of Piriform Cortex and the Lateral Olfactory Tract Following the Loss of Mitral Cells in PCD Mice. *Experimental Neurology* 154:537.
- Belluscio L, Lodovichi C, Feinstein P, Mombaerts P, Katz LC (2002) Odorant receptors instruct functional circuitry in the mouse olfactory bulb. *Nature* 419:0028-0836.

- Blanes T (1898) Sobre algunos puntos dudosos de la estructura del bulbo olfatorio. *Rev Trimestral Micrografica* 3:99-127.
- Brinon JG, Alonso JR, Arevalo R, Garcia-Ojeda E, Lara J, Aijon J (1992) Calbindin D-28k-positive neurons in the rat olfactory bulb. An immunohistochemical study. *Cell Tissue Res* 269:289-297.
- Brinon JG, Weruaga E, Crespo C, Porteros A, Arevalo R, Aijon J, Alonso JR (2001) Calretinin-, neurocalcin-, and parvalbumin-immunoreactive elements in the olfactory bulb of the hedgehog (*Erinaceus europaeus*). *J Comp Neurol* 429:554-570.
- Brinon JG, Martinez-Guijarro FJ, Bravo IG, Arevalo R, Crespo C, Okazaki K, Hidaka H, Aijon J, Alonso JR (1999) Coexpression of neurocalcin with other calcium-binding proteins in the rat main olfactory bulb. *J Comp Neurol* 407:404-414.
- Buck L, Axel R (1991) A novel multigene family may encode odorant receptors: A molecular basis for odor recognition. *Cell* 65:175-187.
- Cajal SRy (1911) *Histologie du Systeme Nerveux de l'Homme et des Vertebres*. Paris: Maloine.
- Carlson GC, Shipley MT, Keller A (2000) Long-lasting depolarizations in mitral cells of the rat olfactory bulb. *J Neurosci* 20:2011-2021.
- Chen WR, Xiong W, Shepherd GM (2000) Analysis of relations between NMDA receptors and GABA release at olfactory bulb reciprocal synapses. *Neuron* 25:625-633.
- Crespo C, Blasco-Ibanez JM, Marques-Mari AI, Martinez-Guijarro FJ (2001) Parvalbumin-containing interneurons do not innervate granule cells in the olfactory bulb. *Neuroreport* 12:2553-2556.
- Crespo C, Blasco-Ibanez JM, Brinon JG, Alonso JR, Dominguez MI, Martinez-Guijarro FJ (2000) Subcellular localization of m2 muscarinic receptors in GABAergic interneurons of the olfactory bulb. *Eur J Neurosci* 12:3963-3974.
- Crespo C, Blasco-Ibanez JM, Marques-Mari AI, Alonso JR, Brinon JG, Martinez-Guijarro FJ (2002) Vasoactive intestinal polypeptide-containing elements in the olfactory bulb of the hedgehog (*Erinaceus europaeus*). *J Chem Neuroanat* 24:49-63.

- Desmaisons D, Vincent JD, Lledo PM (1999) Control of action potential timing by intrinsic subthreshold oscillations in olfactory bulb output neurons. *J Neurosci* 19:10727-10737.
- Freeman WJ (1975) Mass action in the nervous system. New York: Academic Press.
- Freund TF, Buzsaki G (1996) Interneurons of the hippocampus. *Hippocampus* 6:347-470.
- Fritschy J-M, Mohler H (1995) GABA<sub>A</sub>-receptor heterogeneity in the adult rat brain: differential regional and cellular distribution of seven major subunits. *J Comp Neurol* 359:154-194.
- Gonchar YA, Johnson PB, Weinberg RJ (1995) GABA-immunopositive neurons in rat neocortex with contralateral projections to S-I. *Brain research* 697:27-34.
- Gracia-Llanes FJ, Crespo C, Blasco-Ibanez JM, Marques-Mari AI, Martinez-Guijarro FJ (2003) VIP-containing deep short-axon cells of the olfactory bulb innervate interneurons different from granule cells. *Eur J Neurosci* 18:1751-1763.
- Gray EG (1959) Axo-somatic and axo-dendritic synapses of the cerebral cortex: an electron microscope study. *Journal of Anatomy* 93:420-433.
- Greer CA, Shepherd GM (1982) Mitral cell degeneration and sensory function in the neurological mutant mouse Purkinje cell degeneration (PCD). *Brain Res* 235:156.
- Gulyas AI, Hajos N, Freund TF (1996) Interneurons containing calretinin are specialized to control other interneurons in the rat hippocampus. *J Neurosci* 16:3397-3411.
- Gulyas AI, Hajos N, Katona I, Freund TF (2003) Interneurons are the local targets of hippocampal inhibitory cells which project to the medial septum. *Eur J Neurosci* 17:1861-1872.
- Hamilton KA, Heinbockel T, Ennis M, Szabo G, Erdelyi F, Hayar A (2005) Properties of external plexiform layer interneurons in mouse olfactory bulb slices. *Neuroscience* 133:819-829.
- Hayar A, Shipley MT, Ennis M (2005) Olfactory bulb external tufted cells are synchronized by multiple intraglomerular mechanisms. *J Neurosci* 25:8197-8208.

- Hayar A, Karnup S, Shipley MT, Ennis M (2004a) Olfactory bulb glomeruli: external tufted cells intrinsically burst at theta frequency and are entrained by patterned olfactory input. *J Neurosci* 24:1190-1199.
- Hayar A, Karnup S, Ennis M, Shipley MT (2004b) External tufted cells: a major excitatory element that coordinates glomerular activity. *J Neurosci* 24:6676-6685.
- Hirata Y (1964) Some Observations on the Fine Structure of the Synapses in the Olfactory Bulb of the Mouse, with Particular Reference to the Atypical Synaptic Configurations. *Arch Histol Jpn* 24:293-302.
- Hoffer BJ, Siggins GR, Bloom FE (1971) Studies on norepinephrine-containing afferents to Purkinje cells of rat cerebellum. II. Sensitivity of Purkinje cells to norepinephrine and related substances administered by microiontophoresis. *Brain Res* 25:523-534.
- Holderith NB, Shigemoto R, Nusser Z (2003) Cell type-dependent expression of HCN1 in the main olfactory bulb. *Eur J Neurosci* 18:344-354.
- Jahr CE, Nicoll RA (1980) Dendrodendritic inhibition: demonstration with intracellular recording. *Science* 207:1473-1475.
- Jinno S, Klausberger T, Marton LF, Dalezios Y, Roberts JD, Fuentealba P, Bushong EA, Henze D, Buzsaki G, Somogyi P (2007) Neuronal diversity in GABAergic long-range projections from the hippocampus. *The Journal of neuroscience* 27:8790-8804.
- Jolliffe IT, Morgan BJ (1992) Principal component analysis and exploratory factor analysis. *Stat Methods Med Res* 1:69-95.
- Kasowski HJ, Kim H, Greer CA (1999) Compartmental organization of the olfactory bulb glomerulus. *The Journal of Comparative Neurology* 407:261-274.
- Keverne EB (1995) Olfactory learning. *Current Opinion in Neurobiology* 5:482-488.
- Kosaka K, Toida K, Aika Y, Kosaka T (1998) How simple is the organization of the olfactory glomerulus?: the heterogeneity of so-called periglomerular cells. *Neurosci Res* 30:101-110.
- Kosaka K, Aika Y, Toida K, Kosaka T (2001) Structure of intraglomerular dendritic tufts of mitral cells and their contacts with olfactory nerve terminals and

- calbindin-immunoreactive type 2 periglomerular neurons. *J Comp Neurol* 440:219-235.
- Kosaka T, Kosaka K (2005) Intraglomerular dendritic link connected by gap junctions and chemical synapses in the mouse main olfactory bulb: Electron microscopic serial section analyses. *Neuroscience* 131:611-625.
- Kosaka T, Kosaka K (2007) Heterogeneity of nitric oxide synthase-containing neurons in the mouse main olfactory bulb. *Neurosci Res* 57:165-178.
- Laurent G (2002) Olfactory network dynamics and the coding of multidimensional signals. *Nat Rev Neurosci* 3:884-895.
- Laurent G, Davidowitz H (1994) Encoding of olfactory information with oscillating neural assemblies. *Science* 265:1872-1875.
- Laurent G, Stopfer M, Friedrich RW, Rabinovich MI, Volkovskii A, Abarbanel HD (2001) Odor encoding as an active, dynamical process: experiments, computation, and theory. *Annu Rev Neurosci* 24:263-297.
- Macrides F, Schneider SP (1982) Laminar organization of mitral and tufted cells in the main olfactory bulb of the adult hamster. *J Comp Neurol* 208:419-430.
- Macrides F, Schoenfeld TA, Marchand JE, Clancy AN (1985) Evidence for morphologically, neurochemically and functionally heterogeneous classes of mitral and tufted cells in the olfactory bulb. *Chem Senses* 10:175-202.
- Markram H, Toledo-Rodriguez M, Wang Y, Gupta A, Silberberg G, Wu C (2004) Interneurons of the neocortical inhibitory system. *Nat Rev Neurosci* 5:793-807.
- McBain CJ, Fisahn A (2001) Interneurons unbound. *Nat Rev Neurosci* 2:11-23.
- McLean JH, Shipley MT (1987) Serotonergic afferents to the rat olfactory bulb: I. Origins and laminar specificity of serotonergic inputs in the adult rat. *J Neurosci* 7:3016-3028.
- McQuiston AR, Katz LC (2001) Electrophysiology of interneurons in the glomerular layer of the rat olfactory bulb. *J Neurophysiol* 86:1899-1907.
- Meskenaite V (1997) Calretinin-immunoreactive local circuit neurons in area 17 of the cynomolgus monkey, *Macaca fascicularis*. *J Comp Neurol* 379:113-132.
- Mori K (1987) Membrane and synaptic properties of identified neurons in the olfactory bulb. *Progress in Neurobiology* 29:275.

- Mugnaini E, Oertel WH, Wouterlood FF (1984) Immunocytochemical localization of GABA neurons and dopamine neurons in the rat main and accessory olfactory bulbs. *Neurosci Lett* 47:221-226.
- Murphy GJ, Darcy DP, Isaacson JS (2005) Intraglomerular inhibition: signaling mechanisms of an olfactory microcircuit. *Nat Neurosci* 8:354-364.
- Nickell WT, Shipley MT (1988) Two anatomically specific classes of candidate cholinceptive neurons in the rat olfactory bulb. *J Neurosci* 8:4482-4491.
- Nusser Z, Sieghart W, Mody I (1999) Differential regulation of synaptic GABA<sub>A</sub> receptors by cAMP-dependent protein kinase in mouse cerebellar and olfactory bulb neurones. *J Physiol (Lond)* 521:421-435.
- Nusser Z, Naylor D, Mody I (2001a) Synapse-specific contribution of the variation of transmitter concentration to the decay of inhibitory postsynaptic currents. *Biophys J* 80:1251-1261.
- Nusser Z, Kay LM, Laurent G, Homanics GE, Mody I (2001b) Disruption of GABA<sub>A</sub> receptors on GABAergic interneurons leads to increased oscillatory power in the olfactory bulb network. *J Neurophysiol* 86:2823-2833.
- Orona E, Rainer EC, Scott JW (1984) Dendritic and axonal organization of mitral and tufted cells in the rat olfactory bulb. *The Journal of Comparative Neurology* 226:346-356.
- Panzanelli P, Perazzini AZ, Fritschy JM, Sassoe-Pognetto M (2005) Heterogeneity of gamma-aminobutyric acid type A receptors in mitral and tufted cells of the rat main olfactory bulb. *J Comp Neurol* 484:121-131.
- Paxinos G, Watson C. *The rat brain in stereotaxic coordinates*. Academic Press. London: 1998
- Pinching AJ, Powell TP (1971a) The neuron types of the glomerular layer of the olfactory bulb. *J Cell Sci* 9:305-345.
- Pinching AJ, Powell TP (1971b) The neuropil of the periglomerular region of the olfactory bulb. *J Cell Sci* 9:379-409.
- Pinching AJ, Powell TP (1971c) The neuropil of the glomeruli of the olfactory bulb. *J Cell Sci* 9:347-377.
- Pressler RT, Strowbridge BW (2006) Blanes cells mediate persistent feedforward inhibition onto granule cells in the olfactory bulb. *Neuron* 49:889-904.

- Price JL, Powell TP (1970a) The mitral and short axon cells of the olfactory bulb. *J Cell Sci* 7:631-651.
- Price JL, Powell TP (1970b) The synaptology of the granule cells of the olfactory bulb. *J Cell Sci* 7:125-155.
- Price JL, Powell TPS (1970c) The Morphology of the Granule Cells of the Olfactory Bulb. *J Cell Sci* 7:91-123.
- Puopolo M, Belluzzi O (1998a) Functional heterogeneity of periglomerular cells in the rat olfactory bulb. *Eur J Neurosci* 10:1073-1083.
- Puopolo M, Belluzzi O (1998b) Inhibitory synapses among interneurons in the glomerular layer of rat and frog olfactory bulbs. *J Neurophysiol* 80:344-349.
- Rall W, Shepherd GM, Reese TS, Brightman MW (1966) Dendrodendritic synaptic pathway for inhibition in the olfactory bulb. *Experimental Neurology* 14:44-56.
- Ressler KJ, Sullivan SL, Buck LB (1994) Information coding in the olfactory system: evidence for a stereotyped and highly organized epitope map in the olfactory bulb. *Cell* 79:1245-1255.
- Sassoe-Pognetto M, Panzanelli P, Sieghart W, Fritschy JM (2000) Colocalization of multiple GABA<sub>A</sub> receptor subtypes with gephyrin at postsynaptic sites. *J Comp Neurol* 420:481-498.
- Schneider SP, Macrides F (1978) Laminar distributions of interneurons in the main olfactory bulb of the adult hamster. *Brain Res Bull* 3:73-82.
- Schoenfeld TA, Marchand JE, Macrides F (1985) Topographic organization of tufted cell axonal projections in the hamster main olfactory bulb: an intrabulbar associational system. *J Comp Neurol* 235:503-518.
- Schoppa NE (2006a) AMPA/kainate receptors drive rapid output and precise synchrony in olfactory bulb granule cells. *J Neurosci* 26:12996-13006.
- Schoppa NE (2006b) Synchronization of olfactory bulb mitral cells by precisely timed inhibitory inputs. *Neuron* 49:271-283.
- Schoppa NE, Westbrook GL (2001) Glomerulus-Specific Synchronization of Mitral Cells in the Olfactory Bulb. *Neuron* 31:639-651.
- Shepherd GM (1972) The neuron doctrine: a revision of functional concepts. *Yale J Biol Med* 45:584-599.

- Shepherd GM, Chen WR, Greer CA. Olfactory bulb. In: Shepherd GM. The synaptic organization of the brain. Oxford University Press. New York. 2004:165-216
- Smith TC, Jahr CE (2002) Self-inhibition of olfactory bulb neurons. *Nat Neurosci* 5:760-766.
- Somogyi P, Hodgson AJ (1985) Antisera to  $\gamma$ -aminobutyric acid. III. Demonstration of GABA in Golgi-impregnated neurons and in conventional electron microscopic sections of cat striate cortex. *J Histochem Cytochem* 33:249-257.
- Somogyi P, Tamas G, Lujan R, Buhl EH (1998) Salient features of synaptic organisation in the cerebral cortex. *Brain Res Rev* 26:113-135.
- Takeuchi Y, Kimura H, Sano Y (1982) Immunohistochemical demonstration of serotonin-containing nerve fibers in the cerebellum. *Cell and Tissue Research* 226:1-12.
- Tibshirani R, Walther G, Hastie T (2001) Estimating the number of clusters in a data set via the gap statistic. *J R Statist Soc B* 63:411-423.
- Toth K, Freund TF (1992) Calbindin D28k-containing nonpyramidal cells in the rat hippocampus: their immunoreactivity for GABA and projection to the medial septum. *Neuroscience* 49:793-805.
- Urban NN (2002) Lateral inhibition in the olfactory bulb and in olfaction. *Physiol Behav* 77:607-612.
- Vassar R, Chao SK, Sitcheran R, Nunez JM, Vosshall LB, Axel R (1994) Topographic organization of sensory projections to the olfactory bulb. *Cell* 79:981-991.
- Wachowiak M, McGann JP, Heyward PM, Shao Z, Puche AC, Shipley MT (2005) Inhibition [corrected] of olfactory receptor neuron input to olfactory bulb glomeruli mediated by suppression of presynaptic calcium influx. *J Neurophysiol* 94:2700-2712.
- White EL (1972) Synaptic organization in the olfactory glomerulus of the mouse. *Brain Res* 37:69-80.
- Willhite DC, Nguyen KT, Masurkar AV, Greer CA, Shepherd GM, Chen WR (2006) Viral tracing identifies distributed columnar organization in the olfactory bulb. *Proceedings of the National Academy of Sciences USA* 103:12592-12597.
- Xu F, Greer CA, Shepherd GM (2000) Odor maps in the olfactory bulb. *J Comp Neurology* 422:489-495.

Zou Z, Horowitz LF, Montmayeur J-P, Snapper S, Buck LB (2001) Genetic tracing reveals a stereotyped sensory map in the olfactory cortex. *Nature* 414:173.

## **IX.2. Publications**

Publications that form the basis of the doctoral dissertation

**Antal M**, Eyre M, Finklea B, Nusser Z (2006) External tufted cells in the main olfactory bulb form two distinct subpopulations. *Eur J Neurosci* 24:1124-1136.

Eyre MD, **Antal M**, Nusser Z (2008) Distinct deep short-axon cell subtypes of the main olfactory bulb provide novel intrabulbar and extrabulbar GABAergic connections. *J Neurosci* 28:8217-8229.

Other publications

Köllő M, Holderith N, **Antal M**, Nusser Z (2008) Unique clustering of A-type potassium channels on different cell types of the main olfactory bulb. *Eur J Neurosci* 27:1686-1699.

## X. ACKNOWLEDGEMENTS

First and foremost, I would like to express the deepest appreciation and thanks to my advisor, Dr. Zoltán Nusser for giving me the opportunity to work in his research group, and for his support throughout my graduate years. He has the attitude and the substance of a genius, who continually and convincingly conveyed a spirit of adventure and excitement in regard to scientific research. His persistent help and guidance enabled me to complete my work successfully. The high standards of his laboratory and good example sculpted my scientific thinking and strengthened my desire to pursue a career in neuroscience.

I thank all my colleagues in the Laboratory of Cellular Neurophysiology, Dr. Noémi Holderith, Dr. Ágota Biró, Dr. Andrea Lőrincz, Dr. Mihály Köllő, Dr. Máté Sümegi, Dr. László Kocsis and Dóra Bánsághiné Rónaszéki for creating an enjoyable working environment and for providing me with inspiring discussions every day. Most importantly, I would like to express my special gratitude to Dr. Mark D. Eyre, my long-standing collaborator and friend, whose constant drive for excellence and contribution made our scientific discoveries possible.

I thank all the colleagues I have met over my years at the Institute of Experimental Medicine, many of who have assisted me in one way or another.

Here, I also thank Dr. Péter Szűcs, my supervisor during my undergraduate years, for his time and effort, and for introducing me to the field of neuroscience.

I thank my parents for their love and support. I am as ever, especially indebted to my father whose advice and moral support has helped me throughout my life.

Lastly, I am grateful to Móni for her encouragement, understanding and emotional support throughout these years.